Available online at www.sciencedirect.com
SCIENCE DIRECT®
PERGAMON
Progress in Energy and Combustion Science 29 (2003) 425–477
PROGRESS IN ENERGY AND COMBUSTION SCIENCE
www.elsevier.com/locate/pecs

# Coal conversion submodels for design applications at elevated pressures. Part I. devolatilization and char oxidation

Stephen Niksa[a,*], Gui-su Liu[a], Robert H. Hurt[b]

[a]*Niksa Energy Associates, 1745 Terrace Drive, Belmont, CA 94002, USA*
[b]*Division of Engineering, Brown University, Box D, 182 Hope Street, Providence, RI 02912, USA*

Received 25 October 2002; accepted 30 May 2003

**Abstract**

Numerous process concepts are under development worldwide that convert coal at elevated pressure. These developments rely heavily on CFD and other advanced calculation schemes that require submodels for several stages of coal chemistry, including devolatilization, volatiles combustion and reforming, char oxidation and char gasification. This paper surveys the databases of laboratory testing on devolatilization and char oxidation at elevated pressure, first, to identify the tendencies that are essential to rational design of coal utilization technology and, second, to validate two well-known reaction mechanisms for quantitative design calculations.

Devolatilization at elevated pressure generates less volatile matter, especially tar. Low-rank coals are no less sensitive to pressure variations than bituminous coals; in fact, coal quality is just as important at elevated pressure as it is at atmospheric pressure. Faster heating rates do not enhance volatiles yields at the highest operating pressures. The FLASHCHAIN® predictions for the devolatilization database depict the distinctive devolatilization behavior of individual samples, even among samples with the same nominal rank. The only sample-specific input requirements are the proximate and ultimate analyses of the coal. There were no systematic discrepancies in the predicted total and tar yields across the entire pressure range. Char oxidation rates increase for progressively higher $O_2$ partial pressures and gas temperatures, but are insensitive to total pressure at constant $O_2$ mole fraction. Char burning rates become faster with coals of progressively lower rank, although the reactivity is somewhat less sensitive to coal quality at elevated pressure than at atmospheric pressure. An expanded version of the carbon burnout kinetics model was able to represent all datasets except one within useful quantitative tolerances, provided that the initial intrinsic pre-exponential factor was adjusted for each coal sample.


*Keywords:* Coal; Pressure; Devolatilization; Pyrolysis; Char oxidation; Modeling; Simulation

**Contents**



*Abbreviations:* CBK, carbon burnout kinetics model; daf, dry-ash-free basis; EFCG, entrained flow coal gasification case in Section 2.6.1; EFR, entrained flow reactor; p.f., pulverized fuel; PFBC, pressurized fluidized bed combustor; p-RCFR, pressurized radiant coal flow reactor; PSD, particle size distribution; SFOR, single first-order reaction; SSE, sum-of-squares error estimate; WMR, electrically heated wire-mesh reactor.

* Corresponding author. Tel.: +1-650-654-3182; fax: +1-650-654-3179.
*E-mail address:* neasteve@pacbell.net (S. Niksa).

0360-1285/03/$ - see front matter © 2003 Elsevier Ltd. All rights reserved.
doi:10.1016/S0360-1285(03)00033-9

## 1. Introduction

Across the globe developers of coal-fired power generators face imperatives to raise conversion efficiencies to compete better with other fuels, especially where $CO_2$ emissions are being reduced. A multitude of process concepts are under development, as surveyed recently in PECS by Beer [1]. All have one thing in common: Primary conversion of the coal feed at elevated pressure. Entrained coal gasifiers operate at 2.5–3.0 MPa, with temperatures to

2000 °C and overall stoichiometric ratios (SR) of about 0.8. Pressurized fluidized bed combustors (PFBCs) operate at 1.5–2.0 MPa, at about 850 °C and a SR near 1.15. Fluidized bed gasifiers operate at similar pressures and temperatures with SR values as low as 0.7. Pressurized pulverized coal boilers are proposed much less frequently than the other units, but have been incorporated to raise steam by burning the residual char with a small portion of coal feed. In one proposed process [2], the boiler operates at 3.1 MPa with conventional waterwall temperatures. Different versions of these processes are being developed in many of the major industrialized nations, including Japan which imports coals from all the major coal producing regions worldwide. Consequently, they will be fed with coals representing the entire range of coal quality, from lignites to subbituminous to high volatile (hv) bituminous to low volatility coals.

Today, any major technology development effort is almost always supported by computational fluid dynamics (CFD) and/or other design calculation schemes. Such massive calculations are organized into submodels for each of the essential physicochemical stages. There are independent submodels for fluid dynamics, particle dynamics, heat transfer, coal conversion chemistry, and chemistry in the gas phase. We will only consider reaction mechanisms which are essential elements of a submodel for coal conversion chemistry at elevated pressures, particularly the following two steps.

(1) The partitioning of the coal feed into volatiles and char is crucial because volatiles are subsequently converted into ultimate products on much shorter time scales than char. The reaction mechanism responsible for the partitioning is called 'devolatilization'. It governs the stabilities of flames on the fuel injectors and also affects temperature profiles and all the major emissions. Devolatilization behavior is widely variable, even among different samples of the same type—or 'rank'—of coal. Devolatilization kinetics are needed in simulations, but the total volatiles yield is the crucial characteristic. The $O_2$ requirement for volatiles combustion and the associated heat release are also important. Volatiles species compositions are generally ignored in design calculations.

(2) The residual char from devolatilization must be completely converted into ultimate products, simply because fuel costs are the major component of process operating costs. Char oxidation must be described because, even in gasifiers, $O_2$ is injected to raise the process operating temperature into the target range. A suitable reaction mechanism must automatically adjust the limiting stage to correctly predict the burning rate, beginning with the intrinsic chemical kinetics at low temperatures, then to $O_2$ transport within the char at moderate temperatures, then to $O_2$ transport from the bulk gas flow to the external char surface at the highest temperatures. Also, the intrinsic kinetics must also depict the substantial differences among the reactivities of chars from diverse coal types, as well as the loss of reactivity by annealing at temperatures above 1000 °C. Additional factors reduce burning rates during the latest stages of burnout, such as the size reductions that lower particle temperatures, thereby re-instituting chemical kinetic control and, in some special cases, the hindered transport through ash layers [3]. When $O_2$ is not present, chars are gasified by the combined chemistry of $CO_2$, $H_2O$, CO, and $H_2$ in the process stream. Differences in char reactivity are thought to be even more important in gasification than in oxidation, because the reaction times are so slow that the gasification agents can penetrate deeper into the chars' internal pore structures. A more significant difference is that the concentration of the gasification agents is determined by chemistry in the gas phase that partially oxidizes and reforms the primary volatiles.

Part I of this paper covers both of these issues with one notable exception: only char gasification by $O_2$ is included. Char reactivities for other gasification agents ($CO_2$, $H_2O$, CO, and $H_2$) are surveyed separately in Part II. This arrangement enables direct references to the substantial databases on devolatilization and char oxidation at atmospheric pressure, to highlight the pressure effects, per se. These same topics were recently discussed in PECS by Wall et al. [4], but with the objectives of thoroughly reviewing the experimental work and surveying some of the major modeling approaches. Our papers are complementary in the sense that reaction mechanisms are emphasized here, and test results are primarily used to evaluate the mechanistic models.

Our ultimate aim is to validate a reaction mechanism for devolatilization that can predict the yields from any coal for heating rates from 10 to $10^5$ °C/s, temperatures from 800 to 2000 °C, and pressures to 3 MPa. This mechanism must also predict the char properties needed to simulate all stages of burnout; viz., the char yield, size, and density of reactive sites. A companion mechanism for char oxidation must predict the burning rates from the onset of ignition to extinction for the same ranges of temperature and pressure, and for $O_2$ levels up to 100%. The ultimate goal is to establish new benchmarks for the quantitative accuracy of predictions for devolatilization behavior and char oxidation reactivity at elevated pressures by evaluating the model predictions against all the available test results in the English literature that specified the required input for the simulations.

Our research strategy is regarded as classical in many branches of engineering science, but is unique in this area. First, all the datasets on devolatilization and char oxidation at elevated pressure in the literature in English were qualified for their suitability for model validations. Then selected datasets from various sources were combined to clearly illustrate the tendencies for all the important operating conditions, including coal quality. Then the predictions from the reaction mechanisms were evaluated with each dataset, and the discrepancies were compiled into statistics for the 'best' representation of the entire database. Although model parameters may have been tuned at various stages in the data evaluations, all model predictions in this

paper are based on the ultimate sets of parameter estimation algorithms for both reaction mechanisms.

At the outset, it is worth noting that several essential mechanisms for detailed process simulations involving devolatilization and char oxidation were omitted. Whereas the devolatilization mechanism, per se, is complete except for fragmentation under very high heat fluxes, essential chemistry for the subsequent conversion of volatiles into soot, partial oxidation products, and other reformed species is not considered. All forms of intraparticle gradients are also neglected. Similarly, all the necessary transport and chemical mechanisms to describe char oxidation at the level of individual particles are considered, but subsequent shifting of the primary oxidation products by gas phase chemistry is omitted. Moreover, essential aspects of single-particle burning in fluidized systems are also omitted, including fragmentation and comminution which are usually primary mechanisms for mass loss in bubbling fluidized beds.

This paper is organized in the same way that the research was conducted, except for the addition of a section on design applications after the model validation section. Devolatilization will be considered first, followed by char oxidation.

## 2. Rapid coal devolatilization at elevated pressures

During entrained-flow gasification, coal particles ground into the pulverized fuel (p.f.) size grade—70 wt% through a 200 mesh sieve—are entrained in oxygen or $O_2$-enriched gases into a very hot, intense mixing field. Swirling flows are used to mix the coal with the hot process gases as fast as possible. Temperatures near the coal injectors can exceed 2000 °C, and pressures are elevated to 2–3 MPa.

Devolatilization in such systems is responsible for generating the gaseous fuels that ignite and stabilize flames onto the coal injectors or, at least, within the mixing region. Since the coal particles are so finely pulverized and the process temperatures are so high, the coal devolatilizes while it is being heated at rates approaching $10^5$ °C/s. Under such conditions, devolatilization begins at 400 to 600 °C, and is complete in only several milliseconds, long before the char reaches the reactor temperature. Even so, the exposure to such high process temperatures is definitely important for the char's subsequent reactivity during char oxidation and char gasification. The volatiles are burned and otherwise transformed on time scales that are at least as fast as those for primary devolatilization.

Among the various chemical reaction mechanisms that come into play during the initial stages of entrained-flow gasification, there are two distinct stages to devolatilization: (1) *Primary devolatilization* generates gases by chemistry among species and functional groups in the condensed phase only; (2) *Secondary pyrolysis* comprises the subsequent transformations among primary products, after they pass through the interface between solid/liquid and gas. These stages are easily distinguished in conceptual terms, but not in practice. In suspension-fired systems, the behavior of individual particles gives way to clouds in which numerous fuel compounds—char, tar, soot, and noncondensible gases—compete for the available $O_2$ while secondary pyrolysis is occurring. The resolution can be much clearer in laboratory studies if special precautions are taken to preserve the primary products.

### 2.1. Prerequisites for data on pressurized devolatilization

To re-create in a laboratory the reaction environment in an entrained-flow gasifier, one needs to impose heating rates of $10^5$ °C/s and resolve the dynamics of the devolatilization process, preferably with complete distributions of all the volatile products plus several characteristics of char and tar. Simply put, this is not possible. It is not necessary either because today's most advanced devolatilization models are able to accurately extrapolate from the measured behavior under less severe operating conditions to more severe conditions within useful quantitative tolerances.

To evaluate devolatilization mechanisms for pressurized applications, data are needed for heating rates above 1 °C/s. Tests with heating rates of 1000 °C/s are preferable because they represent conditions closer to entrained flow conditions that can still be diagnosed within acceptable experimental uncertainties. The test temperatures should be hot enough to achieve ultimate primary devolatilization yields, which are the asymptotic values achieved after extended heating periods.

More formally, the following testing features are required of a dataset to be used to evaluate a devolatilization mechanism:

1. *Coal properties.* At a minimum, the proximate and ultimate analyses are required, as with FLASHCHAIN® [5] and the latest versions of CPD [6] and FG-DVC [7].
2. *Pressure.* Usually a uniform test pressure will be specified although a pressure history can also be analyzed.
3. *Thermal history.* Sufficient information must be available to assign the temperature of the sample as a function of time throughout an entire test.
4. *Impact of secondary chemistry.* Whenever volatiles are released into a flow that is hotter than the parent coal particle, volatiles will be transformed by secondary chemistry. The extent of this transformation should be monitored. Aside from the thermal effects, the gas atmosphere must be chemically inert.

The assignment of thermal histories is, by far, the most cumbersome requirement. One would normally be inclined to monitor devolatilization behavior in an entrained-flow reactor (EFR), simply because this system processes coal in the p.f. grade under similar conditions to most industrial units. But as seen in the sketch in Fig. 1, the operating

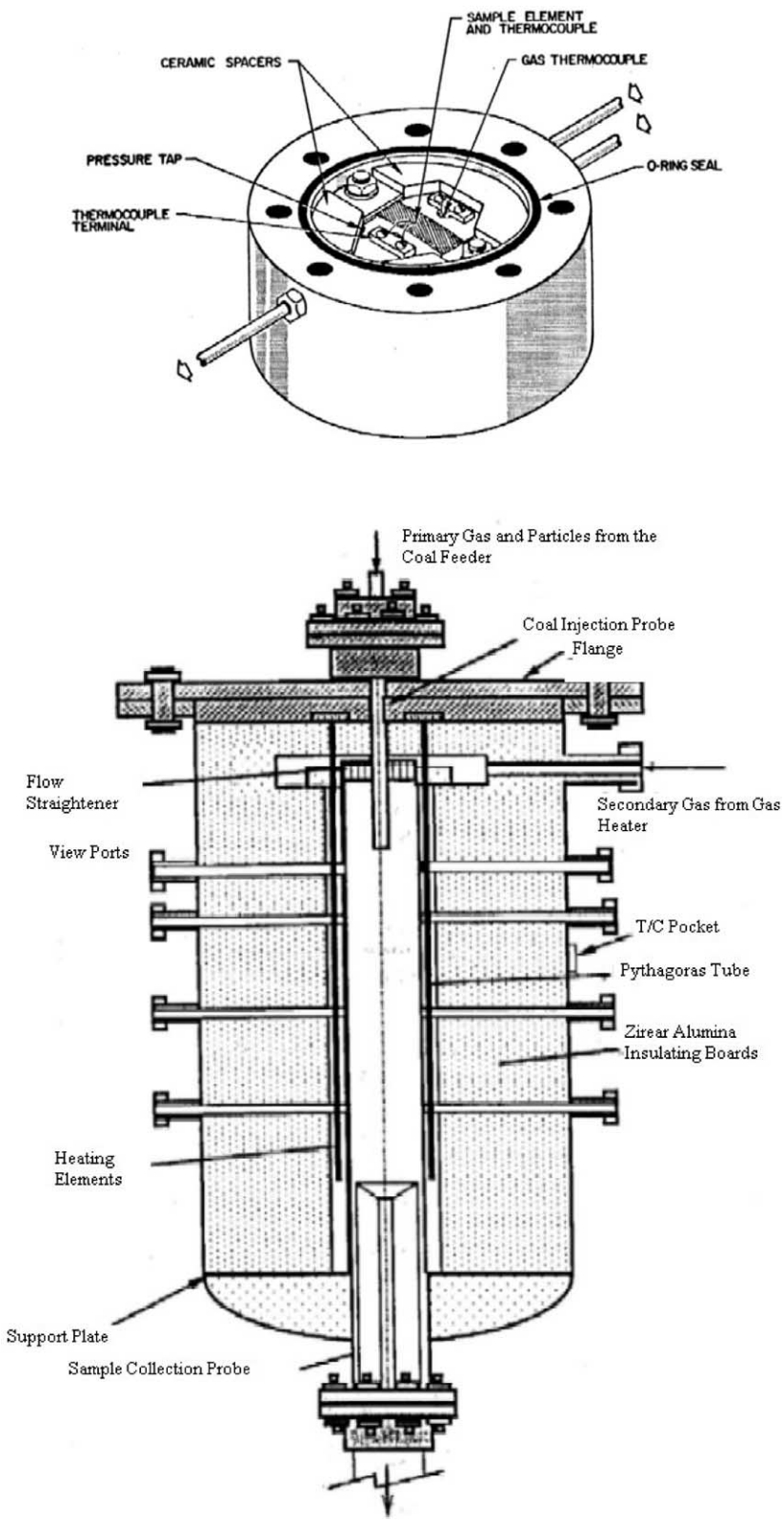


Fig. 1. Sketches of a WMR (top) and an EFR (bottom).

conditions in EFRs are not easy to diagnose or estimate, particularly near the injector where devolatilization occurs. In EFRs, thermal histories are determined by the initial coal temperature, a nominal particle size or particle size distribution (PSD), an entrainment gas temperature and flowrate, a preheated gas temperature and flowrate, the intensity of mixing and particle dispersion at the injector, the reactor temperature profile, the residence time distribution, and the quenching rate. In turn, this information must be incorporated into a heat transfer model that accounts for temperature- and composition-dependent coal thermophysical properties, convective mixing phenomena between the entrainment and preheated gas streams, particle dispersion, particle swelling and mass loss, and several heat transfer mechanisms to assign particle thermal histories. Obviously, the complexity of such calculations admits significant uncertainties into the thermal histories assigned for all EFRs.

After decades of development, there is a much simpler alternative called the 'Wire Mesh Reactor (WMR),' which is also sketched in Fig. 1. About 10 mg of pulverized coal is pressed into or supported on a stainless steel wire mesh which is then mounted between the electrodes in an electrical heating circuit. In modern WMRs, the electrical power is actively controlled to heat the mesh at a prescribed uniform heating rate to a prescribed ultimate temperature for a prescribed reaction period. Dynamics are resolved by actively quenching the support at the end of the reaction period. In other words, the desired thermal history is directly imposed on the sample support, and is therefore much less ambiguous than the calculated thermal histories for EFRs. However in older systems, heating rates were not uniform, ultimate reaction temperatures were highly variable, and there was no forced quenching.

WMRs hold another distinct advantage over EFRs for devolatilization testing. Simply by adding a cross flow over the mesh support, primary products can be rapidly swept away from the hot sample support before they undergo secondary pyrolysis and recovered. Conversely, secondary pyrolysis is always important in EFRs, because the primary products are necessarily released into gases that are hotter than their parent particles. Products recovered from EFRs always represent the combined influence of primary devolatilization and secondary pyrolysis, whereas WMRs can easily be used to characterize pristine primary devolatilization products. This distinction is important because only primary products can be directly related to postulated reaction mechanisms in the coal phase.

In addition to these prerequisites on the regulation of operating conditions, the datasets must include relevant aspects of a coal's devolatilization behavior. The foremost aspect is the ultimate weight loss, on a dry-ash-free (daf) basis, which is obtained with reaction times that are sufficient to achieve constant, asymptotic yields at the highest possible temperatures. Time-resolved yields are more valuable in principle, although, in practice the reaction dynamics are intertwined with all the ambiguities in the assignment of thermal histories. The next most valuable characteristic is a tar yield, because tar production is associated with reaction mechanisms that are especially sensitive to pressure variations. Char characteristics are important, especially elemental compositions, particle sizes (to assign swelling factors), and both bulk and true densities. The compositions of gases and tars are also useful, provided that the extents of secondary chemistry are either made negligible or quantitatively regulated.

### 2.2. The database on pressurized devolatilization

A database on pressurized devolatilization was compiled based on the prerequisites in Section 2.1. The final form appears in Table 1, which lists the performing organization, country, literature citations, the reactor type, number of coals, maximum heating rate, temperature, and pressure, and whether the major products, char composition, gases, and tar compositions were monitored. Twenty-nine datasets were located that satisfy the prerequisites described previously. The US and the UK are the most heavily represented, with 10 and 7 datasets, respectively. But there are also important contributions from other European countries, Scandinavia, Canada, Australia, and Japan. The modest representations from Germany and Japan, in particular, are due to our restriction to the literature in English.

Twenty datasets were obtained with WMRs, seven with conventional EFRs, and one with a novel flow system called the pressurized radiant coal flow reactor (p-RCFR) [37]. This system contains a radiant furnace section consisting of a quartz tube on the axis of a graphite cylinder which is inductively heated to temperatures to 1580 °C. Near-blackbody thermal emission from the graphite rapidly heats a suspension of coal particles as it traverses the furnace. Since the entrainment gas is transparent to the radiation, its only means of heating is by convection from the tube wall and particles. Dilute suspensions have little interfacial surface area for heat transfer, so the entrainment gas remains relatively cool and quenches secondary pyrolysis chemistry among primary products as they are expelled, especially at elevated pressures. This is the only entrained-flow system capable of recovering primary products. The final dataset from AVCO Everett is from a unique apparatus that first dispersed coal particles into a combustible $H_2/O_2$ mixture. The mixture was ignited by spark to provide the hot, pressurized environment that imposed rapid heating rates and devolatilization on the fuel. The population of reactor types is ideal, in so far as the precise regulation of the operating conditions, particularly in the work out of the WMR at Imperial College, provides an abundant database to validate predicted coal quality impacts. The detailed product distributions from the p-RCFR are a perfect compliment to the work with WMRs, even if the thermal histories in this system are more uncertain.

Table 1
Database on pressurized devolatilization

| Organization | Country | References | Reactor | Coals | $D_p$, μm | $Q$, k°C/s | $T$, °C | $P$, MPa | Major products | Char C/H/O/N/S | Gases | Tar C/H/O/N/S |
|---|---|---|---|---|---|---|---|---|---|---|---|---|
| Imperial College | UK | [8,9] | WMR | 1 | p.f. | 1.0 | 1000 | 3.0 | W,T | N | N | N |
| Imperial College | UK | [10–12] | WMR | 4 | p.f. | 1.0 | 1000 | 2.5 | W,T | N | N | N |
| Imperial College | UK | [13] | WMR | 5 | p.f. | 1.0 | 1000 | 3.0 | | | | |
| Imperial College | UK | [14] | WMR | 11 | p.f. | 2.5 | 850 | 15.0 | W,T | N | N | N |
| Imperial College | UK | [15–17] | WMR | 3 | p.f. | 1.0 | 850 | 7.0 | W,T | Y | N | Y |
| Imperial College | UK | [18–20] | WMR | 2 | p.f. | 1.0 | 600 | 15.0 | W,T | N | N | N |
| Silesian Tech. U. | POL | [21] | WMR | 1 | Na | 0.1 | 1100 | 1.5 | W | N | N | N |
| DMT | FRG | [22] | WMR | 1 | 128 | 0.2 | 1000 | 9.0 | | | | |
| DMT | FRG | [23] | WMR | 5 | 260 | 0.2 | 1000 | 10.0 | W,T | N | N | N |
| DMT | FRG | [24] | WMR | 2 | 650 | 9.0 | 800 | 20.0 | W,T | N | N | N |
| DMT | FRG | [25] | WMR | 1 | 263 | 9.0 | 800 | 20.0 | W,T | N | N | N |
| MIT | USA | [26,27] | WMR | 1 | 70 | 1.0 | 1000 | 1.0 | W,T | N | Full | N |
| MIT | USA | [28] | WMR | 6 | 82 | 1.0 | 1000 | 1.0 | W,T | N | Full | N |
| MIT | USA | [29] | WMR | 2 | p.f. | 1.0 | 1000 | 6.7 | W,T | Y | Full | N |
| Princeton U. | USA | [30] | WMR | 6 | 125 | 1.0 | 1000 | 3.4 | W,T | Y | Full | N |
| Princeton U. | USA | [31] | WMR | 6 | 125 | 1.0 | 1000 | 3.4 | W,T | Y | Full | N |
| Princeton U. | USA | [32] | WMR | 1 | 125 | 1.0 | 750 | 10.5 | | | | |
| U. Newcastle | AUS | [33] | WMR | 5 | p.f. | 1.0 | 1000 | 2.0 | W | N | N | N |
| Monash U. | AUS | [34,35] | WMR | 1 | 130 | 1.0 | 1000 | 1.0 | W,T | N | N | N |
| British Coal | UK | [36] | WMR | 17 | 1000 | 1.0 | 950 | 2.5 | W | N | N | N |
| SRI International | USA | [37] | P-RCFR | 6 | 90 | ca. 10 | 1100 | 1.0 | W,T | Y | Full | Y |
| Tohoku U. | JAP | [38] | EFR | 1 | 115 | ca. 10 | 850 | 3.0 | W,T | Y | Full | Y |
| Monash U. | AUS | [39–41] | EFR | 1 | 48 | ca. 100 | 1000 | 1.0 | W | N | N | N |
| VTT | FIN | [42] | EFR | 1 | 95 | ca. 100 | 850 | 0.8 | W | N | N | N |
| Risoe Nat'l Labs. | DMK | [43] | EFR | 1 | p.f. | ca. 100 | 1000 | 2.0 | W | N | N | N |
| U. Alberta | CAN | [44] | EFR | 4 | 140 | ca. 10 | 700 | 5.3 | W | N | $H_2O$ | N |
| Penn State U. | USA | [45–47] | EFR | 3 | 80 | ca. 10 | 915 | 3.6 | W | Y | Full | Y |
| Morgantown Energy Tech. Center | USA | [48–50] | EFR | 1 | p.f. | ca. 100 | 1370 | 6.2 | W | Y | Full | Y |
| Avco Everett Corp. | USA | [51] | Bomb | 13 | p.f. | ca. 100 | 2125 | 1.3 | W | Y | N | N |

The only qualification on the datasets in Table 1 pertains to the data from British Coal. The samples' ultimate analyses were not reported and could not be obtained from the host organization. For some of the coals, we estimated ultimate analyses based on previous work with coals from the same seams that had very similar proximate volatile matter contents; but data on most of these coal samples had to be omitted from the database. Several other datasets were omitted, either because the coal properties were incomplete or because important aspects of the operating procedures were not disclosed in the available publications.

*2.2.1. Operating characteristics*

The database comprises two groups, one each for tests in WMRs and EFRs. There are 260 independent tests with WMRs, and 72 independent tests with EFRs. Each test represents a specific thermal history, pressure, coal sample and particle size. Whenever replicate determinations were reported for the same test conditions, the devolatilization characteristics were averaged and reported under a single test record.

The domains of the most important test conditions across both groups are collected in Table 2. Heating rates were varied from 0.5 to approximately $10^5$ °C/s, and all rates in excess of 9000 °C/s were imposed in EFRs. However, the majority of tests were conducted at 1000 °C/s in WMRs. The ultimate reaction temperatures were varied from 550 to 1300 °C, and all temperatures hotter than 1100 °C were imposed in EFRs. The durations of the pyrolysis experiments tended to be at least several seconds in almost all cases. Consequently, due to the high temperatures and extended heating periods, the thermal histories in these tests were almost always severe enough to achieve ultimate primary devolatilization yields. In fact, we deliberately omitted data from the early stages of heating in the EFR tests for two reasons. First, the omission sharpens the focus on ultimate yields, which are the most important devolatilization characteristics in the vast majority of practical applications. Second, it also circumvents the ambiguities associated with assigning highly accurate thermal histories for all the EFR tests, which are known to be affected by numerous details of the injection hardware and flowfields at the top of the flow tube.

The test pressures covered a range that extends to values far higher than those envisioned for even the most advanced coal processing technologies, and the coverage of the pressure domain is uniformly fine through 10 MPa. All tests were conducted under $N_2$, except those in the combustion bomb which included substantial amounts of steam in the reaction gases. The particle sizes tended to be coarser than the p.f. grade, but usually by only about a factor of 2. Since the heating rates were also slower than in p. f. flames, all the sizes are regarded as sufficiently small to enable interpretations of the devolatilization characteristics that are independent of intraparticle heat and mass transport limitations.

Table 2
Domain of test conditions

| Variable | Range | Typical value |
|---|---|---|
| Heating rate, °C/s | 0.5-ca. $10^5$ | $10^3$ |
| Temperature, °C | 550–1300 | 1000 |
| Reaction time, s | 0.1–90 | 10 |
| *P*, MPa | 0.1–16.7 | 2 |
| Particle size, μm | 48–1000 | 125 |

*2.2.2. Coal quality*

The database represents virtually the entire coal rank spectrum, albeit nonuniformly. Sixty-six coals were tested in WMRs and thirty-three were tested in EFRs. The range of coal quality is shown in two ways in Fig. 2. The upper panel is a coalification diagram, which plots the atomic H/C ratio versus the atomic O/C ratio [52]. Data on a coalification diagram generates the coalification band, which is a banded exponential saturation curve emanating from the origin toward higher O/C values. Anthracites and other low volatility coals lie along the steep trajectory from the origin, whereas high volatile bituminous coals, subbituminous coals, and lignites lie on the saturation band because their H/C ratios are similar while their oxygen contents progressively increase across these ranks. Note that the WMR and EFR groups cover appreciably different ranks. The coals tested in WMRs are concentrated in the hv bituminous rank, and there are relatively very few subbituminous coals. Conversely, the coals tested in EFRs are concentrated in the hvC bituminous and subbituminous ranks, and contain fairly few hv bituminous coals. Only a handful of lignites, brown coals, and low volatility coals were tested in either test configuration.

The plot of the proximate volatile matter contents versus carbon content in the lower panel of Fig. 2 underscores the concentration of hv bituminous coals in the WMR database, and the better coverage of the subbituminous ranks in the EFR database. The conspicuous gap from 85 to 90% carbon and the generally poor coverage of low volatility coals needs to be rectified in future testing programs.

*2.2.3. Reported devolatilization behavior*

Whereas the domains of test conditions and coal quality cover virtually the entire domain of technological interest, the scope of the reported devolatilization characteristics is very limited. Weight loss was monitored in all but 14 of the 332 tests. But tar yields were reported in only 141 tests. Moreover, the collection systems that defined the nature and, therefore, the yields of tar varied significantly among the studies. Fortunately, most of the reported tar yields were collected with WMRs in which special precautions could be taken to minimize secondary pyrolysis. Only three WMR studies [28–30], comprising 10 tests, reported yields of the major noncondensible gases. Similarly, only two

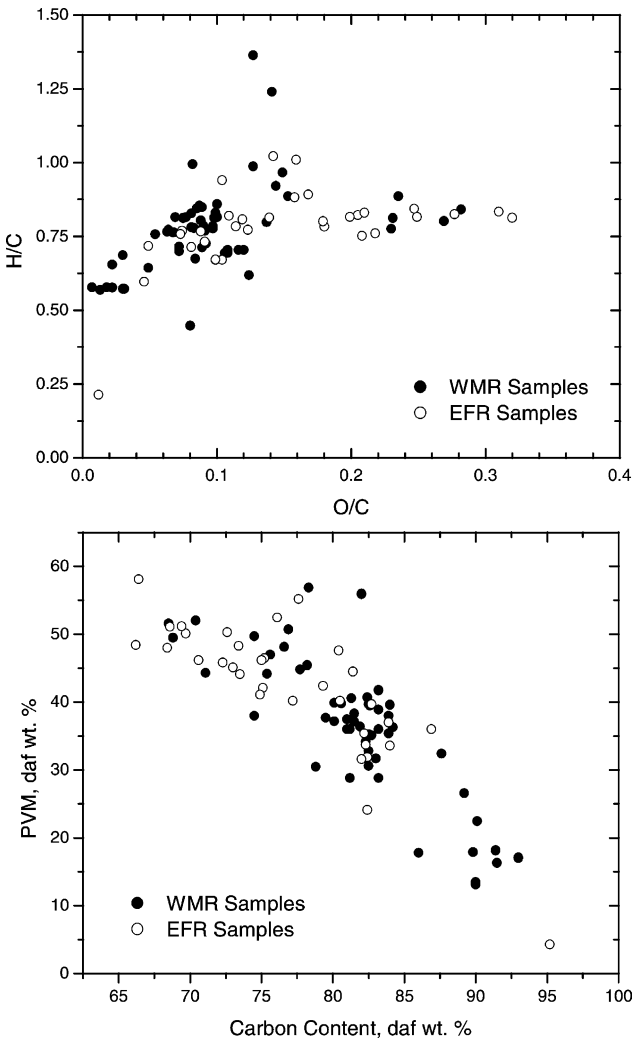


Fig. 2. (Top) Coalification diagram and (Bottom) proximate volatile matter contents of coals tested in WMRs (●) and EFRs (○).

EFR studies comprising 16 tests resolved the distributions of major noncondensible gases [37,38]. Char elemental compositions were reported in only one WMR study with 13 tests [15], and in two EFR studies with 17 tests [37,47]. Elemental compositions of tar collected without appreciable secondary volatiles pyrolysis were reported in only one EFR study with 13 tests [37].

Unfortunately, none of the datasets characterized changes in either particle size or bulk particle density.

### 2.3. Observed impacts of the test conditions

#### 2.3.1. Pressure effects

This section illustrates the most important qualitative trends in the devolatilization characteristics with selected datasets from the database, beginning with the direct impact of elevated pressures on weight loss and tar yields. The ultimate weight loss and tar yields for pressures to 7 MPa from coals representing the three main segments of the rank spectrum appear in Fig. 3. Note the distinctive influence of coal quality, and the much more pronounced pressure effect in the tar yields. Ultimate weight loss from this particular Victorian brown coal is essentially independent of pressure. The bulk of the available data on low-rank coals, however, does exhibit a pressure effect, as discussed below. The weight loss from bituminous and low volatility coals diminishes by 15–25%, with most of the reduction occurring below 1 MPa. The corresponding reduction in the tar yields is much greater at roughly 50%. Since the tar yields diminish by more than the reduction in weight loss, gas yields increase for progressively higher pressures, but not by enough to compensate for the reduction in tar yields.

Among hv bituminous coals, there appears to be little variation among the quantitative sensitivity of weight loss to pressure, as seen in Fig. 4. With carbon contents from 78.2 to 82.6 daf wt%, this suite of coals represents the most

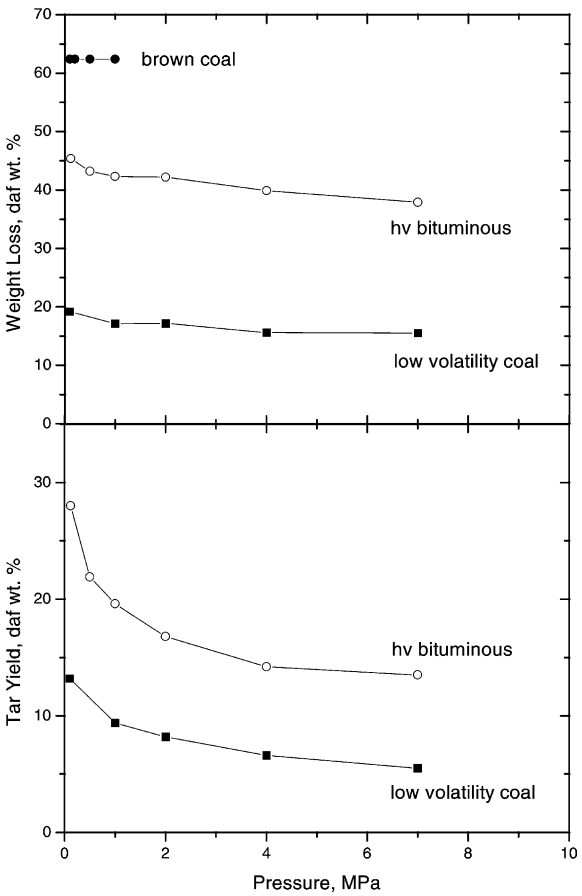


Fig. 3. (Top) Ultimate weight loss and (Bottom) tar yields from Victorian brown coal (●), hv bituminous (○), and a low volatility coal (■) for various pressures.

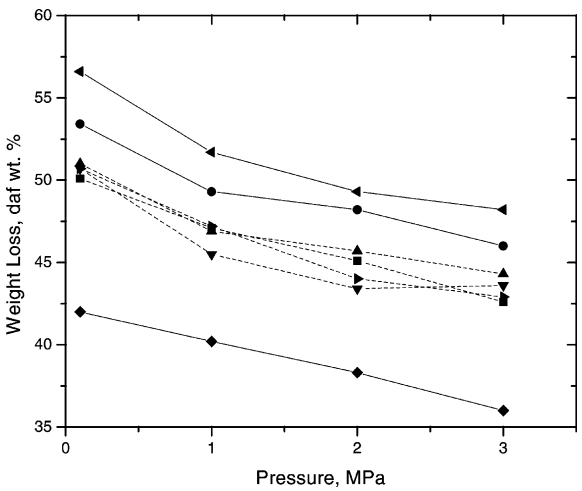


Fig. 4. Weight loss from several similar hv bituminous coals for various pressures after heating in a WMR to 1000 °C for 10 s after heatup at 1000 °C/s [8,9].

popular fuels for power production worldwide. Identical thermal histories were imposed in all tests, and the pressure was the only variable operating condition. The slopes of the curves of weight loss versus pressure are nearly the same, within experimental uncertainty, even while the ultimate yields at atmospheric pressure vary from 44 to 54 daf wt%. Unfortunately, tar yields were not reported for all these cases, but they would almost certainly vary by at least as much as the weight loss. We can reasonably expect ultimate weight loss among hv bituminous coals to diminish by approximately 2.5 daf wt% per MPa increase in pressure, even for a suite of samples whose total and tar yields could be expected to vary significantly.

The impact of pressure on tar characteristics was characterized well over a decade ago in WMR tests in the US [53–56], but has not received any attention since. The molecular weight distributions (MWDs) of tar shift to progressively smaller values for progressively higher pressures, suggesting that a vaporization mechanism is pertinent to any plausible rationale for the impact of pressure on yields.

Otherwise, the elemental compositions of tar are substantially enriched in hydrogen over the respective whole coal values, as seen in Fig. 5. The tars analyzed in

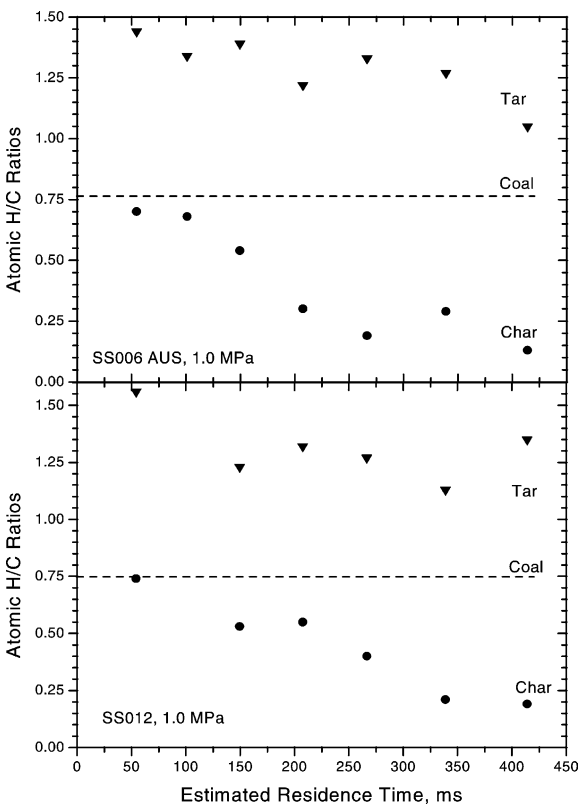


Fig. 5. Time-resolved atomic H/C ratios of tars (▼) and chars (●) recovered after negligible extents of secondary volatiles pyrolysis in an EFR operated at 1 MPa [37].

these tests were not subjected to significant levels of secondary volatiles pyrolysis [37]. The tars are substantially enriched in hydrogen over the whole-coal values, especially those generated during the initial stages of pyrolysis. Ultimately, the enrichment varies from 35 to 70%, based on the data in Fig. 5 as well as tar compositions from the same facility for several other coals. Only the low end of this range is consistent with previous data for comparable coal types for atmospheric pyrolysis. Consequently, it appears that tars generated under elevated pressures show greater enhancements in hydrogen than those generated at atmospheric pressure. Estimated oxygen contents of the tars varied from 8 to 20%, which are only half to two-thirds of the values reported for atmospheric pyrolysis with some of these same coals. This difference probably reflects the elimination of oxygen functional groups from intermediate fragments of coal molecules at elevated pressure before they were released as tar compounds.

The H/C ratios of chars fall continuously throughout devolatilization, as they do for chars prepared at atmospheric pressure. The ultimate values are very sensitive to the severity of the imposed thermal history, especially to reaction time, because char H/C ratios fall as $H_2$ is eliminated on time scales that are considerably longer than those for primary devolatilization. We have no reason to expect this process to be affected by pressure variations.

As mentioned previously, the yields of noncondensible gases are greater at higher pressures, but not by enough to compensate for the reduction in tar yields. Yields of CO, $CH_4$, and the other aliphatic hydrocarbons are enhanced the most, whereas $CO_2$ and $H_2O$ yields are hardly perturbed [28–30]. The very few data available on how pressure affects the oils yields (which are primarily benzene, toluene, and xylene) suggest that oils yields are reduced slightly at elevated pressures [37].

Whereas elevated operating pressures definitely affect ultimate primary devolatilization yields, they do not appear to affect the reaction dynamics. This feature is shown in Fig. 6 with transient weight loss from a hv bituminous coal at three pressures. The WMR in this study featured reproducible thermal histories and a nitrogen spray quench that could resolve reaction times into 100 ms increments [32]. It was used to resolve the transient weight loss under vacuum and at 0.19 and 3.60 MPa for the study in Fig. 6. The time on the abscissa is the time after the sample was heated at 1000 °C/s to 750 °C, which explains why nonzero weight loss was recorded at zero time in the figure. The curves in Fig. 6 are polynomial fits to the test data. In so far as their slopes indicate the nominal devolatilization rates, it is evident that elevating the pressure does not affect the rate-limiting aspects of the devolatilization mechanism. Moreover, it appears that the mechanisms governing the devolatilization rate are independent of the mechanisms responsible for the impact of pressure on ultimate yields, particularly the tar vaporization mechanism.

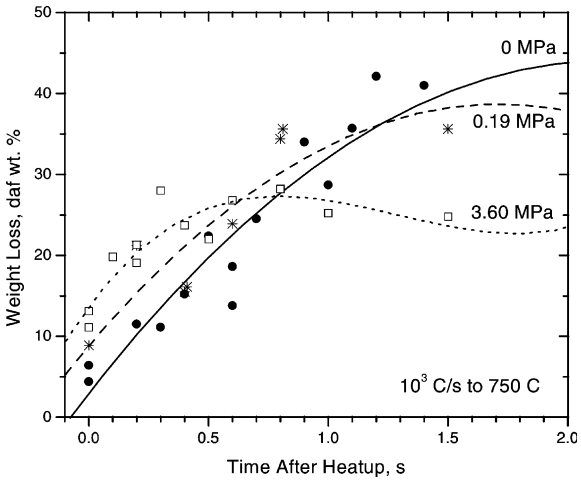


Fig. 6. Time-resolved weight loss versus time after the end of the heating period from the same hv bituminous coal for vacuum (●), 0.19 MPa (✷), and 3.6 MPa (□). In all cases samples were heated at 1000 °C/s to 750 °C [32].

There is a discernable shift of the weight loss transients to shorter times for progressively higher pressures, which was attributed to heat transfer aspects of this particular WMR. A sweep gas was preheated to 400 °C and passed over the sample support near the onset of electrical heating. The convective heat transfer rate from such a flow would depend on pressure in two ways. First, it would take the sample to slightly higher temperatures before the onset of electrical heating at higher pressures and, second, it would transfer heat into the sample at a faster rate during the forced heating cycle at progressively higher pressures. Both of these effects could account for the small shifts to shorter times in Fig. 6, which are probably inconsequential to the apparent indication of pressure-independent devolatilization rates.

### 2.3.2. Heating rate effects

It is firmly established that elevating the pressure reduces weight loss and, especially, tar yields. It is also firmly established that accelerating heating rates enhances ultimate yields, especially the tar yields. But through the 1980s, this conclusion had been exclusively based on data for various heating rates at atmospheric pressure. The ensuing test data for various heating rates at elevated pressures indicates that heating rate variations become much less important, as seen in Fig. 7. These yields are from the same hv bituminous coal for various heating rates at 0.12 and 7 MPa. Extended reaction times after the heating period were imposed in all cases, although the ultimate temperature was 700 °C at 0.12 MPa and 600 °C at 7 MPa. Notwithstanding the temperature variation, the data clearly show that faster heating does not enhance weight loss at elevated pressures.

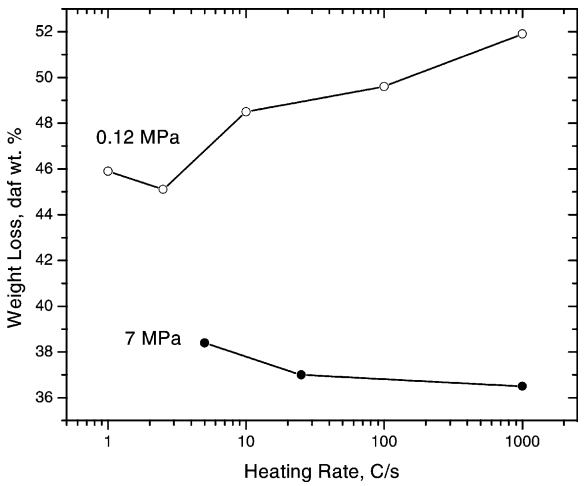


Fig. 7. Ultimate weight loss versus the heating rate to 700 °C at 0.12 MPa (○) and to 600 °C at 7 MPa (●) [18,19].

The additional data [14] collected in Table 3 firmly establish this tendency, and suggest that yield enhancements due to faster heating may weaken continuously for progressively higher pressures. The data for the Linby coal exhibit a substantial yield enhancement due to faster heating at 0.25 MPa in both weight loss and tar yields. But at 2 MPa only the weight loss is enhanced while tar yields are nearly independent of heating rate. And at 7 MPa, both weight loss and tar yields from this coal are insensitive to variations in heating rate. Among the five other coals in Table 3, both subbituminous coals (Pecket, Catamutum) exhibit appreciable weight loss enhancements at 7 MPa, but neither of the bituminous coals (Pit. No. 8, Longannet) shows an enhancement. The apparent enhancement with the low volatility coal (Tilmanstone) is difficult to resolve from experimental uncertainty. Notwithstanding these ambiguities, the tar yields from five of these six coals are slightly *lower* for 1000 °C/s than for 1 °C/s. Evidently, faster heating rates promote the production of intermediate compounds that are unable to vaporize at elevated pressures and therefore unable to be recovered as tar.

Table 3
Yields for various heating rates at elevated pressure

| Coal | *P*, MPa | Weight loss, daf wt% | | Tar yield, daf wt% | |
|---|---|---|---|---|---|
| | | 1 °C/s | 1000 °C/s | 1 °C/s | 1000 °C/s |
| Linby | 0.25 | 40 | 45.1 | 17.5 | 24.4 |
| | 2 | 36.8 | 41.9 | 15 | 13.7 |
| | 7 | 35.7 | 37.8 | 15 | 12.2 |
| Pit. No. 8 | 7 | 36.7 | 35.9 | 20.5 | 11.4 |
| Pecket | 7 | 46.8 | 50.9 | 9.5 | 9.3 |
| Catamutum | 7 | 47.3 | 53.6 | 11.6 | 13.8 |
| Longannet | 7 | 31.8 | 33.9 | 11.8 | 10.6 |
| Tilmanstone | 7 | 13 | 16 | 7.9 | 6.1 |

### 2.3.3. Coal quality impacts

We next characterize the impact of coal quality at elevated pressures. Both weight loss and tar yields are extremely sensitive to coal constitution, even among coals of the same nominal rank. This so-called 'sample-to-sample variability' is evident in all devolatilization characteristics, but is especially significant among tar yields. Since elevating the pressure suppresses tar production, one could reasonably expect that tar yields and, by association, weight loss would be less sensitive to coal quality at elevated pressures than at atmospheric pressure. But the data indicate otherwise.

A subset of the WMR database was assembled according to the following stipulations. All samples were exposed to heating rates of 1000 °C/s or faster, and brought to temperatures that were high enough to achieve ultimate yields. In each study, identical thermal histories were imposed on the same coals at 0.1 and 1 MPa. Eight studies conducted independently by several investigators worldwide satisfied these conditions with weight loss measurements, and seven studies qualified with tar yields. The tar yields and the associated weight loss appear in Figs. 8 and 9, respectively, and a subset of the weight loss data for hv bituminous coals only appears in Fig. 10.

In Fig. 8, there is a one-to-one correspondence among the tar yields at the two pressures. In other words, the sample-to-sample variability is unaffected by elevating the pressure. The percentage reduction in tar yields due to the pressure elevation (in the lower panel) diminishes from roughly 40% with lignites to 25% with low volatility coals, albeit within the considerable scatter in the data for the lowest rank coals. The $r^2$ correlation coefficient of the linear regression through the data is only 0.45. Until this ambiguity is eliminated, it is not possible to ascertain whether the tar yields from all coal types diminish by the same percentage as the pressure is elevated, or if lower rank tars are more sensitive to pressure increases.

The weight loss associated with the tar yields appears in Fig. 9. Here too, there is a one-to-one correspondence among the weight loss values at both pressures that indicates that the sample-to-sample variability is unaffected by pressure elevations. The only exception is the coal with 77.7% carbon. The percentage reduction in weight loss due to the pressure elevation is essentially independent of coal quality; the correlation coefficient of the regression is only 0.09. With a nominal value of only 8%, the percentage reduction in weight loss is also much less than the reduction in tar yields.

With hv bituminous coals, the weight loss is usually about twice the tar yield, so the typical reduction in tar yield of 30% would reduce the weight loss by 15%. But the actual reduction is only half the limiting value, implying that

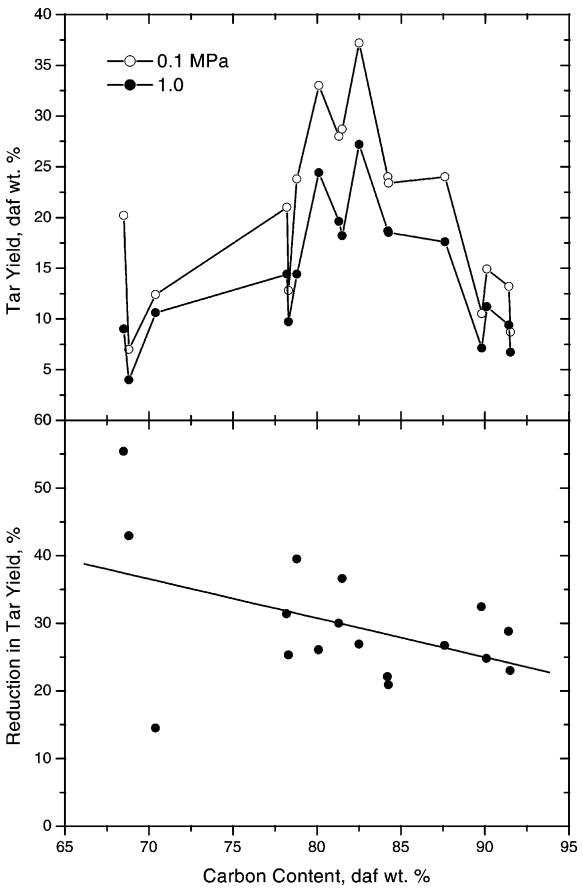


Fig. 8. (Upper) Ultimate tar yields at 0.1 (○) and 1 MPa (●) and (Lower) the percentage reduction reported in seven independent WMR studies that imposed identical rapid thermal histories at both pressures.

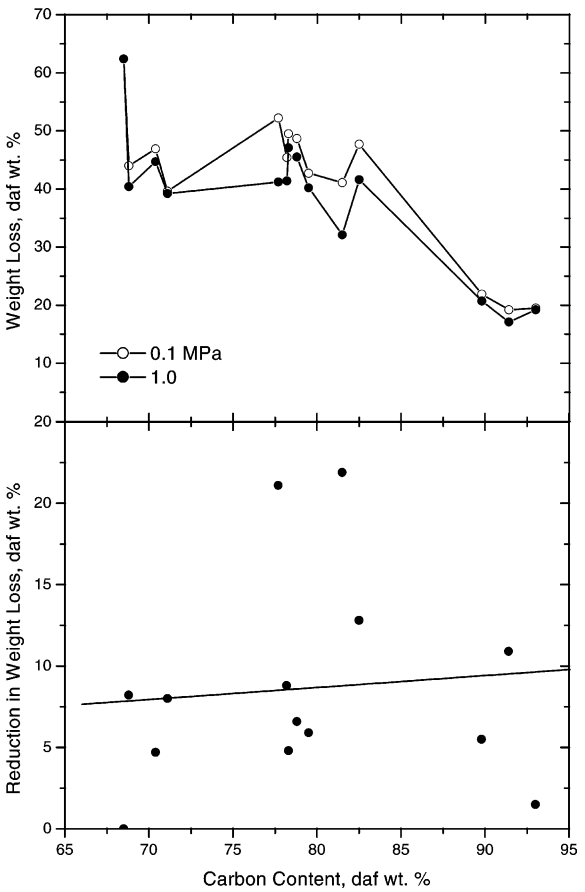


Fig. 9. (Upper) Ultimate weight loss at 0.1 (○) and 1 MPa (●) and (Lower) the percentage reduction reported in seven independent WMR studies that imposed identical rapid thermal histories at both pressures.

approximately half the mass of the tar that fails to vaporize is subsequently expelled as noncondensible gases. Since the regression of the tar reduction percentages in Fig. 8 suggests that tar yields from the lowest ranks are reduced even more by the same pressure elevation, much more than half of these tars must be cracked into gases. Typically, tars constitute only about a quarter of the weight loss from the lowest rank coals. If 40% of the tar fails to vaporize, then 80% of this retained tar mass must be expelled as gases to reduce the weight loss by the typical value of 8%. Considering the abundance of oxygen in low rank coals and the tars they release, and the propensity of oxygen-bearing radicals to promote organic decompositions in the temperature range of interest, it is not inconceivable that a higher percentage of the retained tar mass will be gasified with low rank coals than with bituminous coals. But more data with low rank coal samples is needed to definitively resolve this issue.

For the hv bituminous coals of greatest technological interest, elevating the pressure does not diminish the impact

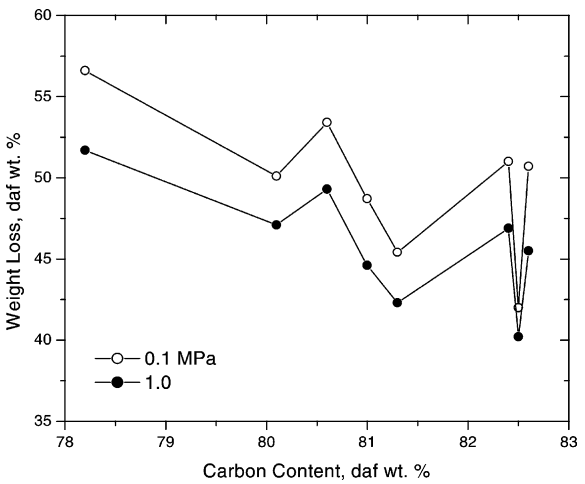


Fig. 10. Ultimate weight loss at 0.1 (○) and 1 MPa (●) reported for several similar hv bituminous coals in WMR studies that imposed identical rapid thermal histories at both pressures [15,8,9].

of coal quality in any discernable way, as seen in Fig. 10. The weight loss from this suite of very similar coals again displays the same sample-to-sample variability at both pressures, and the nominal reduction due to the pressure elevation is again approximately 8%.

### 2.4. Mechanistic interpretations

Any mechanistic interpretation for the impact of pressure on rapid coal devolatilization must quantitatively explain the following important aspects: (1) Diminished tar yields in conjunction with gas yields that are enhanced but not by enough to compensate; (2) Lighter and more hydrogen-enriched tar; (3) More CO and aliphatic hydrocarbons, especially $CH_4$, but unperturbed $CO_2$ and $H_2O$ yields; (4) Pressure-independent devolatilization rates; (5) A loss of sensitivity to heating rate variations; (6) Unperturbed coal quality impacts.

The first interpretation put forward [57], called classical devolatilization theory, only addressed the pressure effects on total weight loss and tar yields. Its essential ingredient is secondary redeposition of released volatiles into residues which remain in the char on a time scale set by the transport mechanism for volatiles escape. Consequently, factors that promote secondary redeposition chemistry, such as the higher vapor concentrations at elevated pressures (or the longer transport times in larger particles) were purported to lower yields. Transport mechanisms such as escape by either continuum or Knudsen diffusion, continuum diffusion of liquids through a melt, bulk flow through macropores, film-diffusion-limited evaporation from a melt, and bubble rupture and growth in a viscous melt have been analyzed. Several of these models can correlate total weight loss and tar yields over a wide pressure range, but none have ever interpreted tar MWDs or elemental compositions, heating rate effects, or coal quality impacts. Moreover, from a mechanistic standpoint, all such models are definitively contradicted by the observed absence of a size dependence. They cannot explain pressure-independent devolatilization rates either.

Niksa's 'flash distillation analogy' [58] was the first mechanism to circumvent the contradictions of classical devolatilization theory. Following its implementation in FLASHCHAIN®, it was also incorporated into the other two comprehensive devolatilization models, FG-DVC [7] and CPD [6].

The phenomenology sketched in Fig. 11 invokes an analogy between coal devolatilization and the steam distillation of petroleum. When steam is bubbled through a barrel of crude oil, the lightest fractions pass into the vapor and are transported away with bubbles breaking through the surface of the petroleum. But the material with high molecular weight remains in the liquid phase and condenses into coke if the temperature exceeds a certain threshold value. According to FLASHCHAIN®, coal devolatilization follows this same sequence of steps once depolymerization chemistry has disintegrated a coal's original three-dimensional macromolecular structure into a mixture of fragments that has a broad MWD. The role of the steam is played by the noncondensible gases produced whenever aliphatic components are partially converted into refractory char links. Tar is generated when the depolymerization fragments become small enough to vaporize into the escaping noncondensible gases. (Fragments that

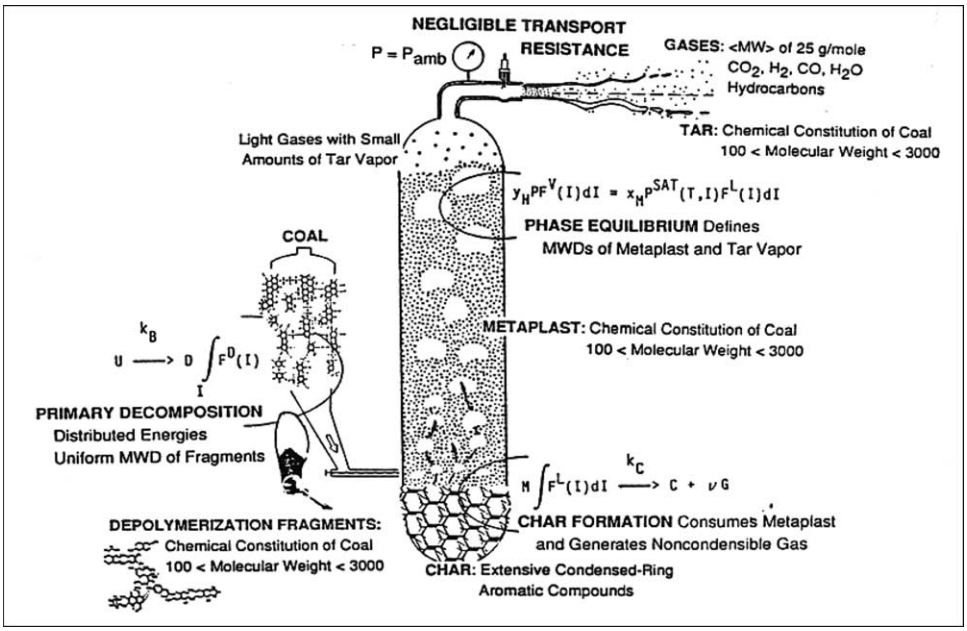


Fig. 11. Coal devolatilization as an equilibrium flash distillation.

vaporize at processing temperatures are still heavy enough to condense into viscous liquids at room temperature.) Char forms by crosslinking among heavier fragments in the condensed phase, whose further depolymerization is suppressed whenever labile connections are converted into refractory char links. Noncondensible gases are produced as a by-product of charring. All this chemistry occurs in the condensed phase, so no redeposition from the gas phase is involved.

Under all practical conditions, the collective mole fraction of all tar components is relatively small, and certainly much smaller than the mole fraction of noncondensible gases. So the mechanism for the transport of gases also governs the release of tar. The flash distillation analogy does not include any finite-rate transport mechanisms. Instead, the escape rate of gases is set equal to their rate of production from the chemical reaction mechanism, under the assumption that a bulk convective flow of gases can be established by a nominally infinitesimal pressure gradient across the particle; hence, internal and ambient pressures are equal and all transport resistances are deemed to be negligible.

According to this mechanism, the influences of thermal history, pressure, and particle size can be understood in terms of only four mechanisms: (1) Coal macromolecules depolymerize into fragments with a broad size distribution; (2) A phase equilibrium establishes the mole fraction of tar fragments in a gas stream that is convected out of the particle with no transport resistance; (3) The conversion of labile bridges in the fragments into char links suppresses depolymerization and simultaneously generates noncondensible gases; (4) Fragments also crosslink in the condensed phase to form nonvolatile components of char.

According to the flash distillation analogy, the phase equilibrium shifts to retain a larger portion of the lighter fragments in the condensed phase as the pressure is increased. These fragments would constitute the heavy end of the tar MWD at low pressures, but remain in the coal at elevated pressures. Consequently, tar prepared at higher pressures becomes lighter and the tar yield diminishes. The fragments retained in the char also contain precursors to noncondensible gases which are eventually released, so gas yields increase as the pressure is elevated, but not by enough to compensate for the retention of tar precursors. Finite-rate transport mechanisms are not needed to explain the pressure effect. In fact, the scaling for negligible transport resistances in FLASHCHAIN® is consistent with the lack of a particle size effect for devolatilization of pulverized coal [58], which presents problems for classical theory that were never reconciled.

Thermal history effects are rooted in the chemical heterogeneity of coals' key reaction centers. A distribution of activation energies for the depolymerization chemistry represents the very broad thermal response of this reaction system, and explains why asymptotic volatiles yields are observed to depend on the pyrolysis temperature. But competitive char formation chemistry is needed to explain the proportions of tar and gas from coals of different rank. Heating rate affects the rate, yields, and composition of volatiles. As the heating rate is increased, the onset of devolatilization moves to higher temperatures and the devolatilization rate increases in rough proportion to the heating rate. Rapid heating enhances yields at lower pressures by delaying the generation of primary fragments until higher temperatures are achieved, where more of the heavier fragments are expelled as tar. Consequently, tar becomes more abundant and heavier as heating rates are accelerated and gas yields decrease because the additional tar shuttles away precursors to noncondensibles. But at elevated pressures, the heavier tar fragments cannot vaporize so the heating rate enhancements diminish. Some of the fragment mass is retained in the char, while the rest is released as noncondensible gases.

The reason that nominal devolatilization rates are independent of pressure is because they are determined by chemical kinetics in the condensed phase, not by transport mechanisms. The rates of the chemical reactions that depolymerize the coal macromolecules and convert labile bridges into char links are functions of temperature and the concentrations of all reactive functional groups in coal. To a first approximation, both temperature and the concentrations are independent of pressure, so the overall devolatilization rate is insensitive to pressure variations. In actuality, the concentrations of tar precursors in the condensed phase are increased when the phase equilibrium shifts to retain heavier fragments in the condensed phase. But the increase is relatively small, because most of the components of the original coal macromolecule remain in the condensed phase under all operating pressures.

In FLASHCHAIN®, the vaporization of tar precursors is not represented as a finite-rate process. Rather, like-sized fragments in the condensed and vapor phases are in phase equilibrium. The equilibrium is modeled with a form of Raoult's Law for continuous mixtures, and it stipulates the mole fraction of tar in a binary mixture with a stream of noncondensible gases. As in a conventional application of Raoult's Law, the mole fraction of tar vapor is specified as the product of the mole fraction of condensed tar and the saturated vapor pressure of tar precursors, $P^{\mathrm{SAT}}(T, \mathrm{MW}_{t_j})$, according to

$$\sum_{j=1}^{J^*} p_j = \sum_{j=1}^{J^*} x_{m_j} P^{\mathrm{SAT}}(T, \mathrm{MW}_{t_j}) = \sum_{j=1}^{j^*} x_{m_j} P_{\mathrm{C}} \exp\left(-\frac{A(\mathrm{MW}_{t_j})^z}{T}\right) \tag{1}$$

where $p_j$ is the partial pressure of a tar $j$-mer; $J^*$ is the degree of polymerization of the largest tar molecule; $x_{m_j}$ is the mole fraction of a tar $j$-mer in the condensed phase; $T$ is the temperature, $\mathrm{MW}_{t_j}$ is the molecular weight of a tar $j$-mer; and $P_{\mathrm{C}}, A$, and $z$ are adjustable constants. Note that

the three adjustable constants are the primary means to improve the predicted weight loss and tar yields over a broad pressure range. In particular, both $P_C$ and $A$ were adjusted to improve the predictions for the database compiled for this project, as presented in Section 2.5.

Perhaps, the greatest challenge in devolatilization modeling has been to interpret the substantial sample-to-sample variability among the devolatilization behavior of even very similar coal samples with the same nominal rank (Figs. 8–10). Such coal quality impacts are clearly based on coals' chemical constitution and macromolecular configuration. In FLASHCHAIN®, crosslinked coal macromolecules are modeled as a mixture of chain fragments ranging in size from a monomer to the nominally infinite chain. The diverse assortment of structural components in real coals is rendered coarsely with four generic structural components: aromatic nuclei, labile bridges, char links, and peripheral groups. Aromatic nuclei are refractory units with the characteristics of the hypothetical aromatic cluster based on $^{13}C$ NMR analysis. Except for HCN production from their nitrogen, nuclei are immutable. Nuclei are interconnected by two types of linkages: labile bridges or char clinks. Labile bridges contain all the oxygen, sulfur, and aliphatic carbon, but no aromatic components. Being refractory, char links are completely aromatic with no heteroatoms. Peripheral groups are the remnants of broken bridges having the same composition.

Since they contain the most reactive heteroatoms, labile bridges are the key reaction centers. The pool of all aliphatic hydrocarbon elements and all oxygen and sulfur are allocated to the population of labile bridges, then apportioned to the aromatic nuclei according to the absolute number of intact linkages and the relative amounts of labile bridges and char links. As demonstrated elsewhere in detail [59], the elemental compositions of whole coals are very poor indicators of the compositions of their reaction centers. In particular, the atomic ratios of bridges, $(H/C)_B$ and $(O/C)_B$, are markedly superior regressions variables for devolatilization behavior because they exhibit the largest sample-to-sample variability and correctly depict the tendencies in the pyrolysis chemistry across the entire rank spectrum. Many of the structural parameters and reaction rate constants in FLASHCHAIN® are correlated with $(H/C)_B$ and/or $(O/C)_B$. Whereas these primary regressions are continuous functions of these atomic ratios, the correlated modeling parameters exhibit substantial scatter when plotted versus more conventional coal rank parameters, such as the daf carbon content, as shown in Ref. [59]. Hence, FLASHCHAIN® predictions are able to depict the sample-to-sample variability in Figs. 8–10 because the model parameters were never expressed as continuous functions of the primary coal properties. The calculation scheme to specify $(H/C)_B$ and $(O/C)_B$ from proximate and ultimate analyses and databases of other characterization data has been reported [59].

### 2.5. Data evaluations

FLASHCHAIN® was improved for applications at elevated pressures with the following strategy: evaluations with the WMR database were used to fine-tune the regressions for the structural parameters and rate constants described in the previous section to obtain the maximum accuracy for the complete ranges of pressure and coal quality in the database. First, every record in the WMR database was predicted to establish the baseline performance of the model. Then model parameters were adjusted to eliminate all systematic discrepancies. Once all parameters were specified at their final values, the complete WMR database was again predicted to establish the improved performance of the model. Finally, all records in the EFR database were predicted with no further parameter adjustments to establish the performance for simulated entrained-flow applications.

The criterion for evaluating the model predictions is the standard error of estimation (SSE), which is defined as follows

$$\mathrm{SSE} = \sqrt{\frac{\sum_{i=1}^{n_S} (p_i^P - p_i^O)^2}{n_S - n_F - 1}} \tag{2}$$

where $n_S$ is the number of records under evaluation; $p_i^P$ is the prediction for the $i$th record; $p_i^O$ is the measured value; and $n_F$ is the number of independent factors accounted for in the model. The number of independent modeling factors is easiest to specify when the model is a multivariate regression; however, it is ambiguous with mechanistic models like FLASHCHAIN®. Throughout the evaluations in this paper, $n_F$ was specified as 5 to account for the variations in pressure, heating rate, temperature, reaction time, and coal quality. Since $n_S$ is so much greater than unity, the specification on $n_F$ is unimportant.

Throughout the ensuing evaluation of FLASHCHAIN® with data, the most accurate predictions are said to be 'within experimental uncertainty' of the measured values. Considering the diversity of researchers, testing procedures, and test facilities represented in the database, the actual uncertainties in the measured weight loss and tar yields would vary widely among the datasets, and most testing groups neither reported uncertainty estimates nor provided sufficient technical detail for independent assignments. We conservatively assign nominal uncertainties of $\pm 4$ daf wt% to the measured weight loss and tar yields, knowing that the best datasets probably have uncertainties only half this large.

#### 2.5.1. Summary WMR data evaluations

The parity plots for the final parameter assignments appear in Fig. 12. There are no systematic discrepancies in the predicted weight loss and tar yields over the full range of the WMR database. The plots of error versus pressure in

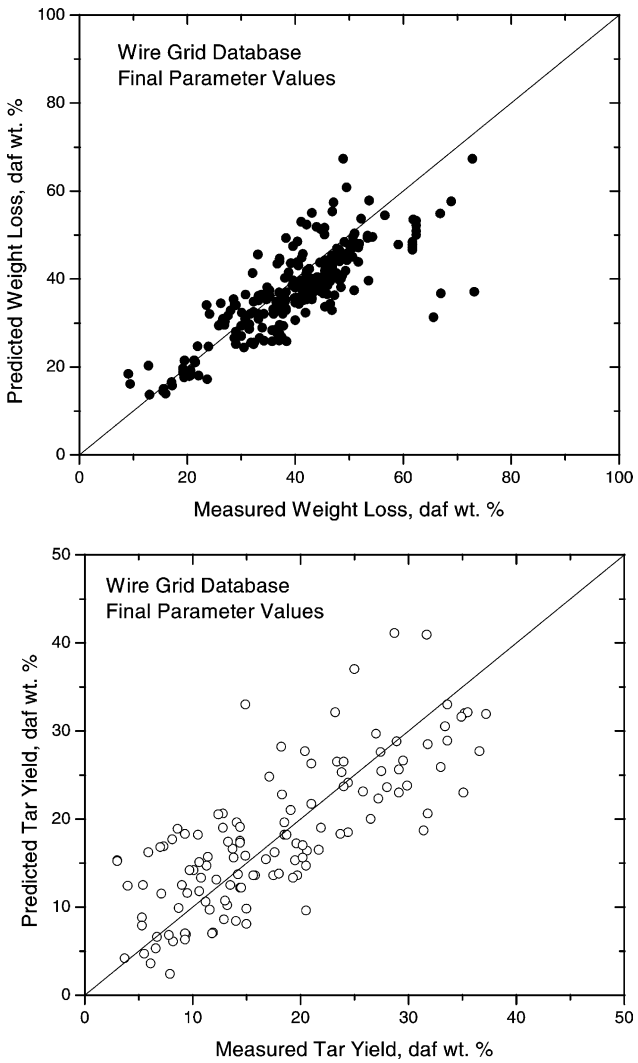


Fig. 12. Parity plots for (Upper) ultimate weight loss (●) and (Lower) tar yields (○) for predictions for the WMR database with the final parameter assignments.

Fig. 13 also show a complete insensitivity to pressure for the weight loss predictions, and only a small sensitivity for the tar yield predictions. For the final parameter values, the SSE for weight loss was 7.4 daf wt%, and the SSE for the tar yields was 5.8 daf wt%. The mean discrepancy in weight loss remains below 10% over the full range of pressure in the WMR database (which is much broader than the range of technological interest). The mean discrepancy in the predicted tar yields remains under 20% over the full range.

*2.5.2. Case studies with WMR evaluations*

This section presents several detailed comparisons with several datasets from the WMR database and predictions based on the final parameter assignments. Evaluations for EFR tests are presented in the next section.

A comparison covering nearly the entire range of bituminous coal properties appears in Fig. 14. Three coals were heated at 1000 °C/s to 700 °C under pressures from 0.1 to 7 MPa [15,17]. The predicted weight loss is within experimental uncertainty over the full pressure range for the Gedling and Tilmanstone samples, and within 5 wt% for the third coal for pressures to 1 MPa. The predicted tar yields are probably within experimental uncertainty for all three coals, provided that pressures are higher than 0.5 MPa. But the predicted tar yields are too low by at least 5 wt% for 0.1 MPa.

The evaluation in Fig. 15 considers the suite of very similar hv bituminous coals that were previously described in Fig. 4 [8,9]. Even though the predicted weight loss is systematically too low by 3–5 wt% for all coals,

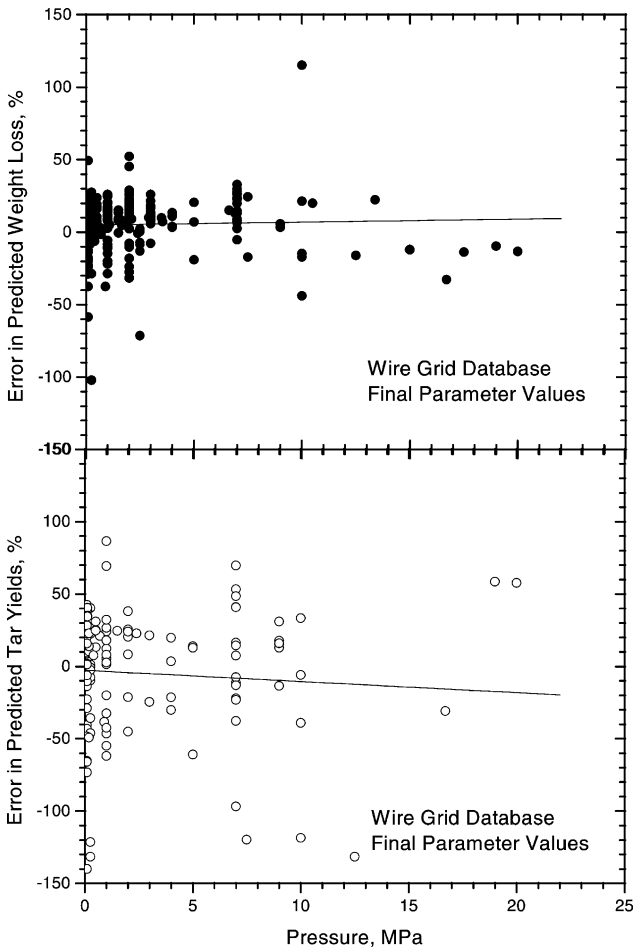


Fig. 13. Error in predicted ultimate weight loss and tar yields (from Eq. (2)) versus pressure for the final parameter values.

the predictions still express the distinctive behavior of individual samples. The Reitspruit coal is predicted and observed to have the lowest yield, and the Ill. No. 6 is predicted and observed to have the highest. Four of these coals are predicted to have essentially the same weight loss, whereas five of the coals are observed to be indistinguishable. The only discrepancy is for the high ash Daw Mill sample, which is predicted to have a slightly lower weight loss than is observed. Notwithstanding these minor flaws, FLASHCHAIN® does depict the distinctive devolatilization behavior of very similar samples of the same nominal rank.

There are no WMR datasets with tar compositions, and only three with noncondensible gas distributions. A representative evaluation of the distribution of noncondensible gases appears in Table 4. The data were recorded for several pressures with Pit. No. 8 coal after heating at 1000 °C/s to 750 °C for a 10 s isothermal reaction period [30]. As recommended in the descriptions of FLASHCHAIN's submechanisms for the production of noncondensibles [5,60], the distribution of noncondensible gases should be calibrated with one measurement (at any set of operating conditions) to predict the distributions at any operating conditions within useful quantitative tolerances. In the present evaluation, the gas yields at atmospheric pressure were used to specify the proportions of $CO_2$, $H_2O$, and $CH_4$ then the model was used without further adjustment to predict the behavior at elevated pressures.

The $CO_2$ yields are predicted within experimental uncertainty across the entire pressure range. Whereas the predicted CO yields increase slightly for progressively higher pressures, the measured values in this dataset decrease slightly (at odds with the rest of the reported data on this species). The predicted $CH_4$ yields increase for higher pressures, but not by as much as the measured values. The predicted changes are also too weak for all other aliphatic hydrocarbons. With this coal there is too little hydrogen available for the postulated mechanisms to predict the $CH_4$ yield even at atmospheric pressures. So all the predicted aliphatic hydrocarbon yields are too low.

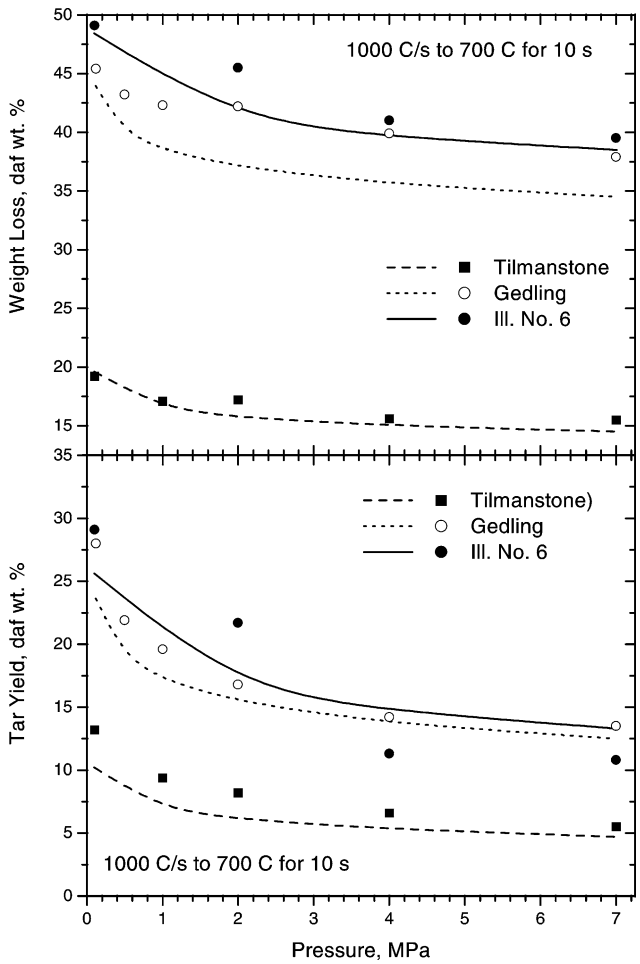


Fig. 14. Evaluation of predicted ultimate (Upper) weight loss and (Lower) tar yields for three bituminous coals [15,17].

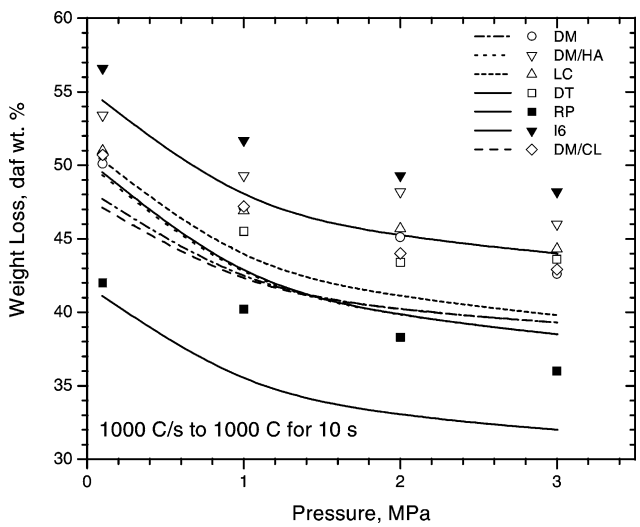


Fig. 15. Evaluation of predicted weight loss from several similar hv bituminous coals for various pressures after heating at 1000 °C/s in a WMR to 1000 °C for 10 s after heatup [8,9].

Table 4
Evaluation of noncondensible gas yields from an hv bituminous coal [30]

| Pressure, MPa | $CO_2$ | | CO | | $CH_4$ | | $C_2$s | | $C_3$s | |
|---|---|---|---|---|---|---|---|---|---|---|
| | Measured | Predicted | Mesured | Predicted | Measured | Predicted | Mesured | Predicted | Mesured | Predicted |
| 0.1 | 0.5 | 0.5 | 1.2 | 0.9 | 2.5 | 1.9 | 0.9 | 0.4 | 0.4 | 0.1 |
| 0.4 | 0.5 | 0.5 | 0.9 | 1.0 | 2.5 | 2.0 | 1.1 | 0.5 | 0.5 | 0.1 |
| 0.7 | 0.6 | 0.5 | 0.9 | 1.0 | 2.7 | 2.0 | 1.3 | 0.5 | 0.6 | 0.1 |
| 1.5 | 0.5 | 0.6 | 0.9 | 1.0 | 2.9 | 2.1 | 1.4 | 0.5 | 0.7 | 0.1 |
| 2.4 | 0.6 | 0.6 | 0.8 | 1.1 | 3.0 | 2.1 | 1.4 | 0.5 | 0.7 | 0.1 |

The next case considers the impact of pressure on the predicted nominal devolatilization rates. The predicted weight loss transients in Fig. 16 are for the same operating conditions used to obtain the data in Fig. 6. The data were omitted from this comparison because the thermometry and coal support systems in the tests are now thought to have introduced a significant lag into the measured weight loss transient, like the ones characterized by Freihaut and Proscia [61]. Consequently, the kinetics in FLASHCHAIN® have been based on data that exhibit much faster rates. Indeed, the model predicts much more weight loss at the end of the heating period than was measured in the tests, as expected. For this reason, the time scale in Fig. 16 is the total time after the start of heating, not the time after the end of the heating period which appears in Fig. 6. Despite the complications in the dynamics, it is still meaningful that the predicted ultimate weight loss is within experimental uncertainty of the measured values at all three pressures.

The important aspect in these predictions is the impact of pressure on the nominal devolatilization rates. It is small in so far as the onset of devolatilization is hardly affected, and the predicted nominal rates of weight loss fall from 107 to 71 daf wt% per second as the pressure is increased from vacuum to 3.6 MPa. The percentage reduction in the rate is identical to the percentage reduction in the predicted ultimate yields. Whereas the mechanisms responsible for the predicted devolatilization dynamics in FLASHCHAIN® are strictly independent of pressure, the predicted rates of weight loss must exhibit a very weak sensitivity to pressure due to the partial retention of tar precursors in the char. This finding is qualitatively in accord with the few available measurements on devolatilization rates for various pressures, but more tests are needed to quantitatively characterize the model's performance with this aspect.

The joint impact of variations in pressure and heating rate are characterized in Fig. 17. This series of calculations is based on the coal properties in Fig. 7, but the temperature and isothermal reaction periods at both pressures were standardized to 700 °C and 10 s, respectively, to sharpen the focus in the presentation on the heating rate variations.

The predictions for 0.12 MPa are directly comparable to the experimental data. They are within experimental uncertainly for all heating rates faster than 100 °C/s, but too low for slower heating rates. The predicted tar yields are similarly flawed. Whereas the weight loss for 7 MPa in Fig. 7

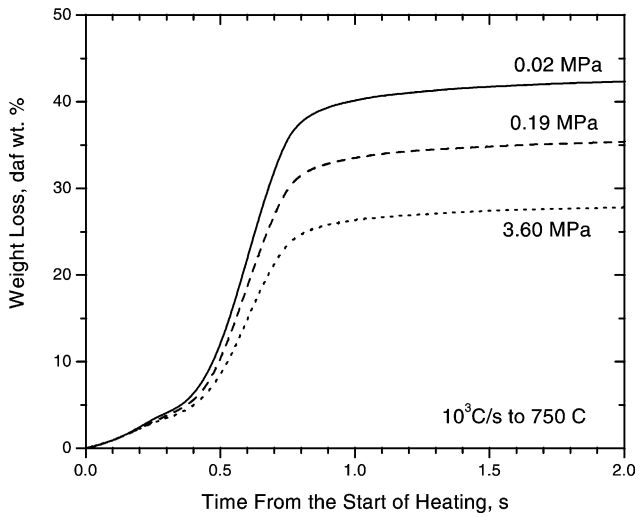


Fig. 16. Predicted weight loss transients after the start of heating for the tests reported in Fig. 6 for vacuum (solid curve), 0.19 MPa (dashed), and 3.6 MPa (dotted). In all cases samples were heated at 1000 °C/s to 750 °C.

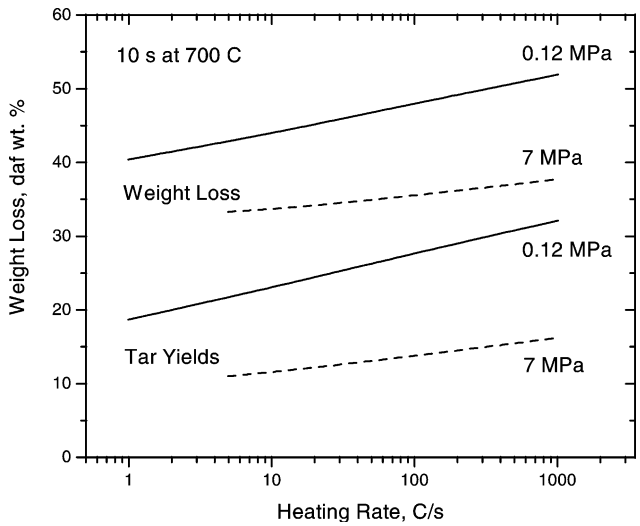


Fig. 17. Predicted ultimate weight loss and tar yields for various heating rates to 700 °C at 0.12 MPa (solid curve) and 7 MPa (dashed curve) for the coal used in the tests in Fig. 7.

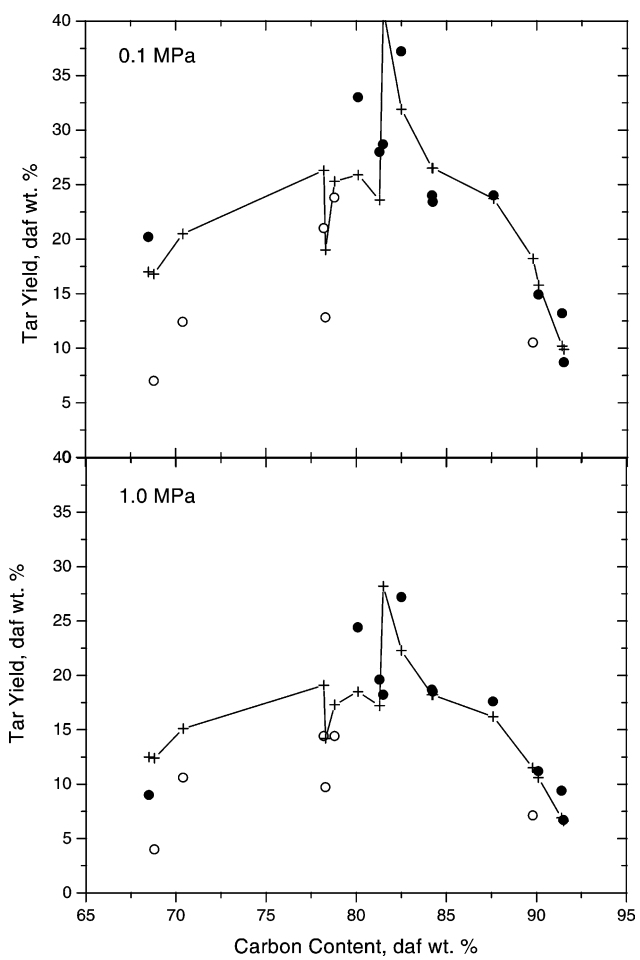


Fig. 18. Evaluation of predicted ultimate tar yields (+ connected by line segments) at (Upper) 0.1 MPa and (Lower) 1 MPa for the datasets in Fig. 8. Data reported by Ko et al. [26] appear as open circles.

diminishes slightly for higher heating rates, nearly all the data for the selection of coals in Table 3 increase with faster heating. Similarly, the predicted weight loss in Fig. 17 increases for faster heating rates, albeit with a much lower sensitivity than for atmospheric pressure, in qualitative accord with the bulk of the available data. However, nearly all the measured tar yields from various coals for 7 MPa in Table 3 diminish at the faster heating rate, at odds with the predicted enhancement at the highest pressure in Fig. 17. The prediction of a smaller enhancement in weight loss for faster heating at elevated pressures is supported by the available data, but the basis for this prediction should be considered suspect in light of the overestimation of tar yields for faster heating rates.

The evaluations of the predicted coal quality impacts appear in Figs. 18–20. Tar yields and weight loss for 0.1 and 1 MPa are considered in Figs. 18 and 19, respectively, and the predicted weight loss from very similar hv bituminous coals is evaluated in Fig. 20. In Fig. 18, the predictions appeared as the plus signs connected by the line segments, and the measured values from Fig. 8 appear as datapoints. Different data symbols have been used to distinguish the data reported by Ko et al. [26] from the others, because this data appears to be systematically lower than other values reported for very similar coals by other investigators.

Sample-to-sample variability is emphasized in the format in Fig. 18, which makes it easy to compare the predicted and observed values point-by-point. The best way to view it is sequentially from left to right, noting if the observed perturbations to the yields are depicted by the theory for every incremental change in carbon content. In the upper panel of Fig. 18, FLASHCHAIN® accurately depicts the sample-to-sample variability among the tar yields reported by all other investigators except Ko et al. for every coal except the one with 81.5% carbon. Moreover, the predictions are within experimental uncertainty in all but two cases. However, the predicted tar yields at atmospheric pressure for Ko et al.'s data are 5–10 wt% higher than

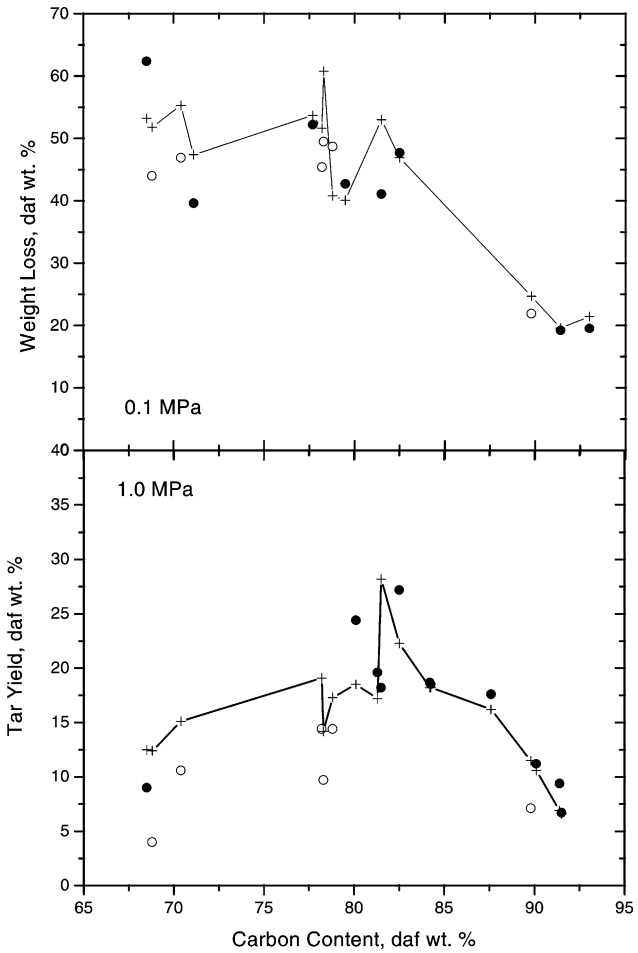


Fig. 19. Evaluation of predicted ultimate weight loss (+ connected by line segments) at (Upper) 0.1 MPa and (Lower) 1 MPa for the datasets in Fig. 9. Data reported by Ko et al. [26] appear as open circles.

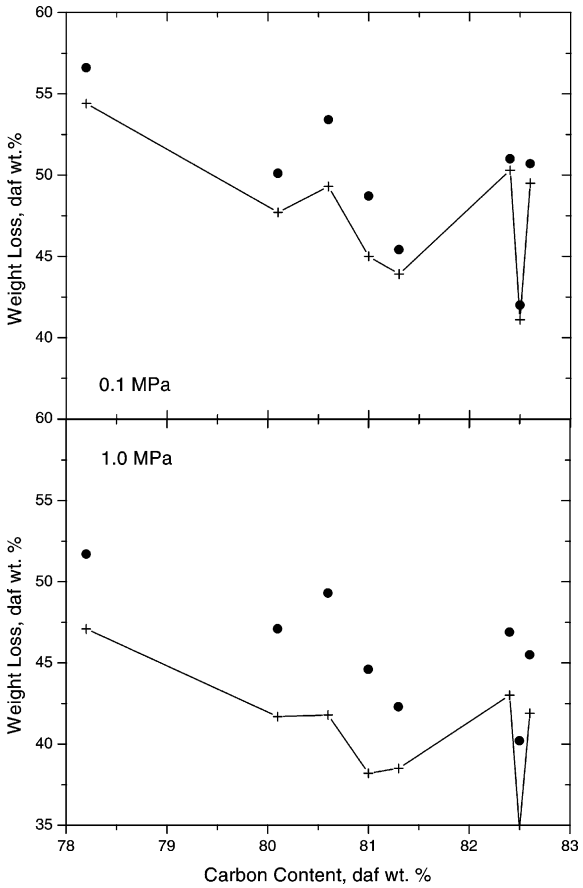


Fig. 20. Evaluation of predicted ultimate weight loss (+ connected by line segments) at (Upper) 0.1 MPa and (Lower) 1 MPa for the datasets for similar hv bituminous coals in Fig. 10.

the measured values for all coals except for the one with 78.8 daf wt% carbon, which is predicted within experimental uncertainty. Notwithstanding the quantitative discrepancies, FLASHCHAIN® accurately depicts the sample-to-sample variability among these coals in every case. The situation is the same for 1 MPa. FLASHCHAIN® accurately depicts the sample-to-sample variability for all coals in this evaluation except the one with 81.5% carbon, but the values for Ko et al.'s coals are higher than the measured values by 5–10 wt%. The coal quality impacts are as evident in the predictions for 1 MPa as for 0.1 MPa, as they should be.

The evaluation of weight loss in Fig. 19 exhibits similar features. In the case for atmospheric pressure, the sample-to-sample variability is evident in the predictions for all coals except the one with 81.5% carbon. Among the ranks of hv bituminous and higher, the predictions are within experimental uncertainty for most cases, although the predictions again overestimate the values reported by Ko et al. except for the coal with 78.8% carbon. The predictions for the low-rank coals are within 5–10% of the observed values, including the two overpredictions for Ko et al.'s data in this range. All of these same features are evident in the evaluation for 1 MPa, except that the quantitative agreement is generally better across the entire rank spectrum. Once again, the predicted coal quality impacts are as evident at 1 MPa as they are at 0.1 MPa, as they should be.

The evaluation of weight loss in Fig. 20 is free of the qualifications regarding inter-laboratory variability that obscure the previous evaluations. All these data were recorded in Prof. Kandiyoti's laboratory at Imperial College. Moreover, they represent a suite of very similar hv bituminous coals to further tighten the stringency in the evaluation of the predicted coal quality impacts. For both pressures, the predicted sample-to-sample variability is correct for every case except for the coal with 81.3% carbon at 1 MPa (which deviates from the relative position of this coal in the 0.1 MPa dataset). The predictions for 0.1 MPa are slightly low but still within experimental uncertainty in all but one case. The underprediction is larger for all coals at 1 MPa, but the accuracy of the predictions remains within useful quantitative tolerances. Since the coal quality impacts are evident in the predictions, the model parameters could be tuned-in to this dataset to improve the quantitative performance at 1 MPa. In fact, the systematic under-predictions in Fig. 20 are probably a manifestation of the inter-laboratory inconsistencies in our WMR database, such as those exhibited by the dataset of Ko et al. They are certainly not evidence of any basic limitation to the mechanisms in FLASHCHAIN®, because the sample-to-sample variability is accurately depicted, even for similar coals of the same nominal rank.

### 2.5.3. EFR evaluations

This section presents the evaluations of FLASHCHAIN® predictions with all the suitable EFR datasets listed in Table 1, including the combustion bomb tests at AVCO Everett. All the predictions are based on the complete set of model parameters that were fine-tuned to represent the WMR database. No further parameter adjustments were made to improve the agreement with the EFR database.

The datasets from the p-RCFR include the most comprehensive product distributions, by far, and will be presented before the emphasis shifts to ultimate weight loss only in the evaluations of the older EFR work. Nominal particle residence times were set by the inlet gas flow rate and the distance between the inlet plane and an argon quench nozzle, which was fixed. Thermal histories in a series of runs with different gas flowrates had similar heating rates, but the suspension achieved different temperatures at the outlet in each case. Higher temperatures were achieved as residence times were extended, but outlet temperatures were always well below the furnace temperature. Thermal histories for these tests were assigned with CFD simulations. The FLASHCHAIN® predictions were based on a much simpler energy balance for individual particles that was tuned to match the CFD simulations.

Table 5
Evaluation of product distributions from the p-RCFR at 1 and 0.1 MPa

| | SS001AUS | | SS002AUS | | SS003AUS | | SS004CHN | | SS005JPN | |
|---|---|---|---|---|---|---|---|---|---|---|
| | Predicted | Measured | Predicted | Measured | Predicted | Measured | Predicted | Measured | Predicted | Measured |
| 1.0 MPa | | | | | | | | | | |
| Wt loss | 31.8 | 29.8 | 44.5 | 50.9 | 31.1 | 29.4 | 33.5 | 46.9 | 58.2 | 49.1 |
| Tar + oils | 18.6 | 16.1 | 24.9 | 26.6 | 17.6 | 12.4 | 18.1 | 24.8 | 27.2 | 24.5 |
| $CO_2$ | 2.1 | 1.1 | 2.4 | 1.8 | 2.9 | 3.2 | 3.3 | 2.4 | 4.0 | 5.3 |
| $H_2O$ | 4.6 | 3.2 | 5.1 | 5.8 | 5.8 | 8.8 | 6.1 | 6.5 | 6.8 | 10.9 |
| CO | 1.3 | 1.0 | 1.8 | 3.5 | 1.7 | 5.4 | 1.7 | 4.3 | 3.0 | 12.2 |
| 0.1 MPa | | | | | | | | | | |
| Wt loss | 39.8 | 43.7 | 52.8 | 54.8 | 39.0 | 48.8 | 41.6 | 45.5 | 69.1 | 65.0 |
| Tar yield | 27.7 | 29.2 | 35.6 | 36.1 | 26.4 | 20.6 | 27.1 | 23.7 | 39.8 | 35.3 |
| $CO_2$ | 1.9 | 1.1 | 2.1 | 2.4 | 2.8 | 4.3 | 3.1 | 2.8 | 3.7 | 2.1 |
| $H_2O$ | 4.2 | 5.1 | 4.5 | 5.4 | 5.4 | 10.1 | 5.8 | 7.0 | 6.3 | 10.9 |
| CO | 1.2 | 1.4 | 1.5 | 3.8 | 1.6 | 9.3 | 1.6 | 6.8 | 3.1 | 8.3 |

Eight coals have been tested in this system at 1 MPa, including five that were also tested at 0.1 MPa. Each test record includes weight loss, plus the yields of tars, oils, and noncondensibles gases ($CO_2$, CO, $H_2O$, $H_2$, $CH_4$, $C_2$'s, $C_3$'s, and HCN), plus the elemental compositions of char and tar. The comparisons of ultimate weight loss and the yields of tar, $CO_2$, $H_2O$, and CO at 1.0 and 0.1 MPa appear in Tables 5 and 6. Table 5 shows the cases for which data are available for 1.0 and 0.1 MPa, and Table 6 shows the cases that were monitored at only 1.0 MPa. FLASHCHAIN® does not yet resolve the oils and tar yields because both products are derived from aromatic nuclei in the whole coal. So the measured tar yields in Tables 5 and 6 are actually the sums of the measured tar and oils yields, respectively.

The predicted weight loss at 1.0 MPa is within experimental uncertainty for SS001AUS, SS003AUS, SS006AUS, and SS013, but slightly underpredicted for SS002AUS. The discrepancies are more substantial in the underprediction, by 12 wt%, for SS004CHN and the overpredictions, by 9 wt% for SS005JPN and by 13 wt% for SS012. These discrepancies are extremely difficult to explain because the predicted weight loss for SS002AUS, SS004CHN, and SS005JPN at 0.1 MPa are within experimental uncertainty. Moreover, SS004CHN is the only bituminous coal in the database on pressurized devolatilization which exhibits the same weight loss (and tar yields) at 1.0 and 0.1 MPa. The discrepancy for SS012 is similarly difficult to explain, although no data are available for this coal at 0.1 MPa. The predicted weight loss at 0.1 MPa is within experimental uncertainty for SS001AUS, SS002AUS, SS004CHN, and SS005JPN, but low by 10 wt% for SS003AUS.

The predicted tar yields for 1.0 MPa are within experimental uncertainty for SS001AUS, SS002AUS, SS005JPN, SS006AUS, and SS012, but slightly overpredicted for SS003AUS and slightly underpredicted for SS004CHN and SS013. The predicted tar yields at 0.1 MPa are within experimental uncertainty for all coals for which tar yields are available for 0.1 MPa, except for the slight overprediction for SS003AUS. Perhaps, most important, the FLASHCHAIN® predictions do identify the significantly higher weight loss and tar yields from SS002AUS and SS005JPN, compared to the other six coals. Within this suite of coal samples, the carbon and oxygen contents of SS002AUS and SS005JPN are not distinctive. Nevertheless, FLASHCHAIN® recognizes the acute impact of these coals' relatively high hydrogen content—both coals have over 6% coal-H—and correctly predicts that the tar yields from SS002AUS and SS005JPN are up to 70% higher than those from the other coals. It is worth emphasizing that none

Table 6
Evaluation of product distributions from the p-RCFR at 1 MPa

| | SS006AUS | | SS012 | | SS013 | |
|---|---|---|---|---|---|---|
| | Predicted | Measured | Predicted | Measured | Predicted | Measured |
| Wt loss | 41.8 | 39.1 | 53.4 | 39.6 | 35.5 | 39.5 |
| Tar + oils | 20.6 | 16.9 | 17.8 | 16.0 | 18.4 | 23.3 |
| $CO_2$ | 3.4 | 2.1 | 7.9 | 3.6 | 2.7 | 0.6 |
| $H_2O$ | 6.3 | 8.4 | 8.4 | 12.2 | 5.5 | 5.0 |
| CO | 2.3 | 3.1 | 6.4 | 1.4 | 1.6 | 2.4 |

of the parameters in FLASHCHAIN® were adjusted to achieve this degree of accuracy.

In the previous evaluation of noncondensible gas distributions (Table 4), the gas distributions at 0.1 MPa were used to calibrate the model parameters used to make the predictions for elevated pressures. No such calibration procedure was implemented for the comparisons in Tables 5 and 6. Among the oxygenated gases, the predicted $H_2O$ yields at 1.0 MPa are predicted to be the most abundant product for all coals. Water was observed to be the most abundant oxygenated gas at 1.0 MPa with all coals except for SS005JPN. The predicted $H_2O$ yields are within 2 wt% of the measured values at 1.0 MPa for all coals except SS003AUS, SS005JPN, and SS012, and at 0.1 MPa for all coals except SS003AUS and SS005JPN. The predicted yields of $CO_2$ agree well with the measurements except with SS012 and SS013, although SS013 is predicted and observed to have the lowest $CO_2$ yield of all.

The CO yields at 1.0 MPa are predicted within useful quantitative tolerances with SS001AUS, SS006AUS, and SS013, but appreciably lower than the observed values with all other coals except SS012, for which the predictions are too high. These discrepancies are rooted in uncertainties in the thermal histories assigned for the tests, because most CO is released during the final stages of primary devolatilization. Consequently, uncertainties in the final temperatures and reaction periods will substantially affect the predicted CO yields. Moreover, since CO is the last oxygenated species released during devolatilization, the errors in the predictions for all the other oxygenated compounds accumulate in the predicted CO yields, through an oxygen balance.

The yields of the oxygenated gases should increase as the pressure is increased, based on the other product distributions in the literature and the production mechanisms in FLASHCHAIN®. But among the five coals for which data at 0.1 and 1.0 MPa are available, this tendency is evident only with SS005JPN. It is very difficult to explain how $CO_2$ and CO yields could diminish with increasing pressure for the four other coals.

The p-RCFR datasets also include tar and char elemental compositions, which were discussed previously (Fig. 5). The predicted tar compositions are generally consistent with the measured values, except that the predicted degree of hydrogen enrichment is greater at 0.1 MPa than at 1 MPa, at odds with the data. Also, the predicted char compositions generally show higher carbon contents than the measured values, although the measured values only close the material balance if more oxygen is included than that which satisfied the oxygen balances.

The next EFR evaluation is based on data from a more conventional EFR system in which a suspension was entrained through a quartz tube heated to approximately 800 °C [38,62]. Data on three low-rank coals were reported for total reaction times exceeding 3 s. The thermal history in the simulations was provided by the investigators. Weight loss was assigned by three independent methods, and the two sets of measurements deemed most accurate were averaged for the evaluation. The tar yields are subject to considerably greater uncertainty because appreciable extents of secondary volatiles pyrolysis were evident as significant amounts of soot and deposited carbonaceous solids. As seen in Table 7, the predicted weight loss values are within experimental uncertainty for all three coals. The predicted tar yields are too low for the low-rank coals, but within experimental uncertainty for the hv bituminous.

Table 7
Evaluation of EFR product distributions at 1 MPa [38,62]

| | Weight loss, daf wt% | | Tar yield, daf wt% | |
|---|---|---|---|---|
| | Predicted | Measured | Predicted | Measured[a] |
| SS012IND, 68.4%C | 51.6 | 52.6 | 9.7 | 16.9 |
| SS011IND, 70.6% | 48.8 | 51.6 | 10.2 | 16.5 |
| SS005JPN, 76.1% | 52.1 | 54.6 | 16.4 | 18.8 |

[a] Evaluated as the sum of the measured yields of tar, deposited coke, and hydrocarbon liquids.

The most extensive selection of coal samples in the EFR database was used in the combustion bomb tests at AVCO Everett [51]. Unfortunately, the thermal histories in the tests were significantly more complex than those in a pressurized drop tube. In the cases under consideration here, a stoichiometric $H_2/O_2/N_2$ mixture was ignited to provide the hot, inert gases for pyrolysis at 1.3 MPa. In the assignment of thermal histories for the simulations, the adiabatic flame temperature of 1325 °C was first lowered to 1200 °C to account for radiative and convective heat losses. However, the steady-state temperature of the 48 μm particles used in the tests suspended in a stagnant gas at 1200 °C would be only 1100 °C. Finally, the investigators estimated the nominal particle heating rate to be roughly $10^5$ °C/s. Hence, these tests were simulated with uniform heating at $10^5$ °C/s to 1100 °C; since the ultimate yields were achieved before the end of the heating period, no isothermal reaction period was specified.

The predictions are compared to the measured values in Fig. 21. Among the 13 coals in the tests, the predictions are within experimental uncertainty in all but three cases. Indeed, for all coals with carbon contents greater than 75%, the agreement is nearly exact, and FLASHCHAIN® again depicts the distinctive sample-to-sample variability among coals of the same nominal rank with uncanny accuracy. All three of the discrepancies are for low-rank coals, suggesting that the model may not be representing these coals with the same accuracy as for the higher ranks. Whereas it appears in Fig. 21 that two low-rank coals with roughly 70% carbon were accurately predicted, both of these coals were actually

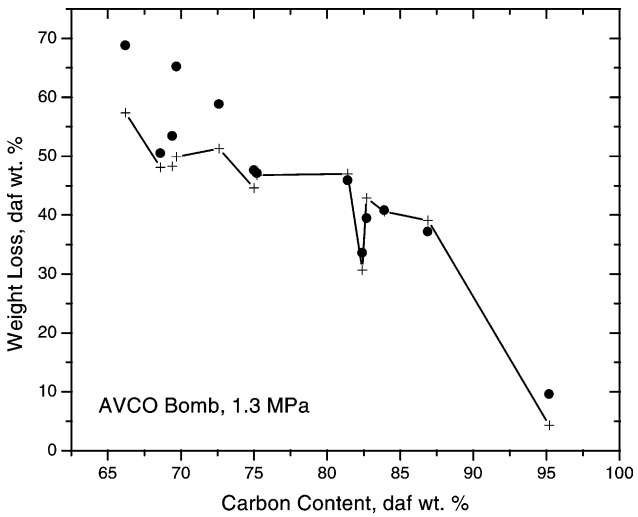


Fig. 21. Evaluation of predicted ultimate weight loss (+ connected by line segments) with the measured values at 1.3 MPa (●) from the AVCO combustion bomb [51].

hv bituminous with nearly 10% sulfur. An alternative explanation for the discrepancies is that the char recovery procedures in the tests may have been degraded by the strong propensity for fragmentation of low-rank chars. Alternatively, the corrections for the extent of weight loss due to steam gasification in the tests may not have accurately accounted for the much higher gasification reactivities of low-rank chars.

The next evaluation emphasizes higher pressures and cooler temperatures than a typical EFR study with p.f. suspensions. The tests were conducted in a heated steel coil with four very similar Canadian subbituminous coals [44]. As seen in Table 8, temperatures were varied from 550 to 700 °C, while pressures ranged from 1.75 to 5.25 MPa. Contact times were approximately 2 s. Among the 14 sets of operating conditions, the largest discrepancy is 4.1 daf wt% (for coal No. 4 at 600 °C and 1.75 MPa) and there are two cases with discrepancies between 3 and 4 wt%. Otherwise, the predictions are within 2.5 wt% of the measured values, and correctly represent the tendencies for increasing temperatures and pressures in all cases. Note that increasing the pressure from 1.75 to 5.25 MPa at the moderate temperatures in this study are predicted and observed to barely perturb the ultimate weight loss.

In addition to the cases considered above, there are a number of studies that reported weight loss only for a single coal at a few sets of operating conditions. These evaluations are summarized as follows.

Bissett [48–50]: All tests were conducted with a p.f. suspension of Rosebud subbituminous coal in a drop-tube furnace specially designed to impose fast heating rates. The predicted ultimate weight loss values generally depict the impact of progressively higher pressures and temperatures, but are higher by 10–20 daf wt% across the board. This discrepancy is impossible to reconcile with the underprediction for the Rosebud subbituminous sample in the AVCO test series, because these coals have nearly identical ultimate analyses. Moreover, several other coals with similar carbon contents were used in the WMR database, and these cases were either predicted within experimental uncertainty or overpredicted by less than 10% (Fig. 19). The most likely explanation for the discrepancies is a procedural breakdown in the tests that led to systematic overestimations of the char yields.

Yeasmin et al. [40]: The measured ultimate weight loss values from a p.f. suspension of Victorian brown coal at 1 MPa and 600, 800, and 1000 °C were 32.1, 54.8, and

Table 8
Evaluation of EFR weight loss at moderate temperatures and high pressures [44]

| Coal | Temperature, °C | Pressure, MPa | Weight loss, daf wt% | |
|---|---|---|---|---|
| | | | Predicted | Measured |
| No. 4 | 550 | 5.25 | 19.0 | 17.3 |
| No. 4 | 600 | 1.75 | 25.6 | 21.5 |
| No. 4 | 600 | 3.50 | 24.8 | 21.5 |
| No. 4 | 600 | 5.25 | 24.4 | 21.9 |
| No. 4 | 650 | 5.25 | 27.9 | 24.8 |
| No. 4 | 700 | 5.25 | 30.5 | 28.6 |
| No. 4 | 550 | 1.75 | 20.0 | 20.7 |
| No. 4 | 550 | 3.50 | 19.3 | 21.0 |
| No. 4 | 550 | 5.25 | 19.0 | 21.0 |
| No. 2 | 550 | 1.75 | 21.8 | 22.4 |
| No. 2 | 550 | 3.50 | 21.1 | 22.2 |
| No. 2 | 550 | 5.25 | 20.8 | 22.6 |
| No. 10 | 550 | 5.25 | 20.1 | 21.9 |
| No. 11 | 550 | 1.75 | 19.1 | 21.4 |
| No. 11 | 550 | 3.50 | 18.4 | 21.7 |
| No. 11 | 550 | 5.25 | 18.0 | 20.7 |

63.9 daf wt%, respectively, versus respective predicted values of 45.7, 57.8, and 62.2.

Hamalainen and Aho [42]: The measured ultimate weight loss from a p.f. suspension of Polish hv bituminous coal at 0.5 MPa and 850 °C was 36 daf wt% versus a predicted value of 38.2%.

Lee et al. [45–47]. The measured weight loss values from a p.f. suspension of Ill. No. 6 hv bituminous coal at 916 °C and 0.1, 0.78, 2.2, and 3.71 MPa were 56.0, 44.4, 43.4, and 34.8 daf wt%, respectively, versus respective predicted values of 51.2, 44.9, 42.1, and 40.4%.

Gjernes et al. [43]: The measured ultimate weight loss values from a p.f. suspension of Columbian hv bituminous coal (El Cerrejon) at 1 MPa and 800, 900, and 950 °C were badly scattered at 42.2, 57.4, and 40.0 daf wt%, respectively, versus respective predicted values of 47.0, 47.7, and 47.7. The measured value at 2 MPa and 900 °C was 37.6 daf wt% versus a predicted value of 45.6%.

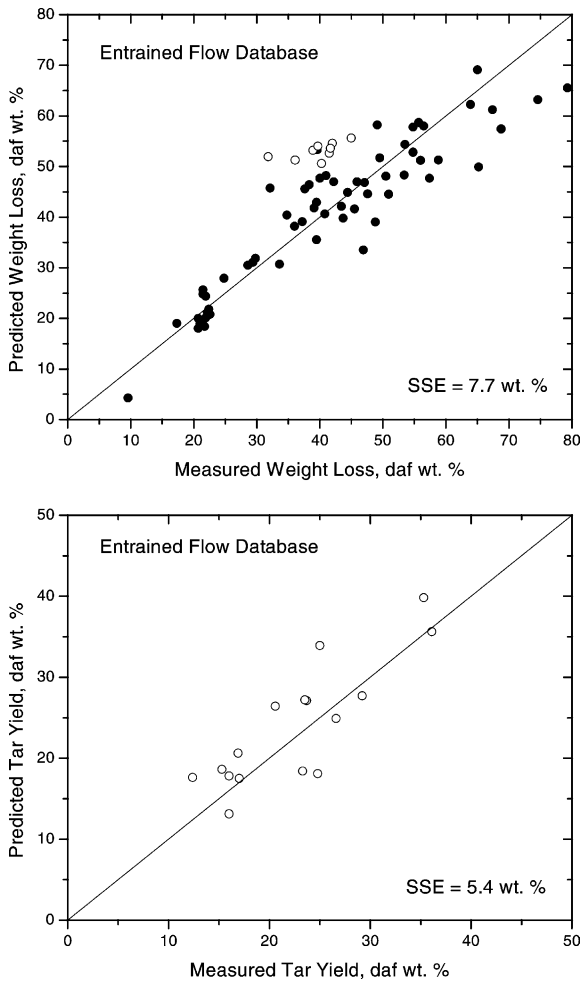


Fig. 22. Parity plots for (Upper) ultimate weight loss (● with ○ denoting the data from Bissett [48–50]) and (Lower) tar yields (○) for the EFR database based on the final parameter values.

A grand summary for the EFR database appears in Fig. 22. The parity plots for weight loss and tar yields exhibit uniform dispersion around the parity line, especially when the suspect data from Bissett's dataset are excluded. The SSE values of 7.7 and 5.4 wt% for weight loss and tar, respectively, are essentially the same as those for the WMR database (7.4 wt% for weight loss and 5.8 wt% for tar yields). Hence, no appreciable uncertainties were introduced into the FLASHCHAIN® predictions by the assignments of thermal histories required for the EFR evaluations.

### 2.6. Devolatilization applications

FLASHCHAIN® predicts the ultimate weight loss and tar yield from any coal at any operating conditions within useful quantitative tolerances, given only the coal's proximate and ultimate analyses. These predictions have been validated over the full domain of technologically relevant operating conditions with the WMR and EFR databases. Most important, the FLASHCHAIN® predictions capture the distinctive devolatilization characteristics of individual samples, and represent the sample-to-sample variability with uncanny accuracy, even among samples with the same nominal rank. FLASHCHAIN® also predicts that nominal devolatilization rates are independent of pressure, in accord with the few available measurements that characterize this aspect.

Whereas the predictions show smaller enhancements due to faster heating rates for progressively higher pressures, the predicted tar yields for very high pressures do not become independent of heating rate, as do the available data. The predictions also do not depict the greater degree of hydrogen enrichment in tars prepared at elevated pressures; in contrast, the predicted tar H/C values diminish slightly for higher operating pressures.

Due to the scarcity of measured product distributions for pressurized pyrolysis and the inconsistencies among the few available datasets, it was not possible to stringently evaluate the predicted distributions of noncondensible gases. FLASHCHAIN® predicts slight enhancements of all oxygenated gases and hydrocarbons for progressively higher pressures. Quantitatively, the enhancements appear to be lower than those observed for aliphatic hydrocarbons, particularly $CH_4$.

Neither the problem in the predictions for heating rate variations at elevated pressures nor that with hydrogen enrichment of tar are serious impediments to practical applications with FLASHCHAIN®. On the one hand, the predicted weight loss and tar yields have already been validated for relevant operating conditions and, on the other, tar is only a short-lived intermediate in any high-temperature, entrained flow process so its characteristics are not particularly important.

Two practical considerations pave the way for practical applications. First, it is not necessary to build FLASHCHAIN® or any other comprehensive devolatilization

mechanism into CFD or other complex engineering calculations, because we can analyze model predictions as we would analyze lab data to assign all the aspects of devolatilization behavior used in the complex calculations. Second, the enormous savings in time in using model predictions compared to lab testing opens up a multitude of opportunities for additional case studies, including broad domains of coal quality and process operating conditions. These advantages are illustrated further in the following sections.

*2.6.1. Global devolatilization expressions*

Complex calculations like CFD implement rudimentary rate expressions for devolatilization like the single first-order reaction (SFOR), two competing reactions, or the distributed activation energy model. Most of these expressions incorporate the ultimate weight loss as an input parameter, so their only function is to describe the change in particle mass as a function of time while the particle is heated after injection into the process. Unfortunately, the rate expressions are too simple to directly connect to the coal properties, so the user is left to determine how the ultimate yield parameter, rate constants, and stoichiometric coefficients should be adjusted for different coal samples. He or she can either compile a database or consult an expert or use a comprehensive mechanism, as follows.

It is always possible to identify the parameters in simple, global rate laws for devolatilization that will closely mimic the predictions from more sophisticated models like FLASHCHAIN®. Here, we illustrate the procedure with the SFOR but any simple rate expression can be analyzed in the same way. The SFOR for devolatilization is

$$\frac{\mathrm{d}V(t)}{\mathrm{d}t} = A\exp\left(-\frac{E_a}{RT}\right)(V^\infty - V(t)) \tag{3}$$

where $V(t)$ is the instantaneous volatiles yield; $V^\infty$ is the hypothetical ultimate volatiles yield; $A$ is a pseudo-frequency factor, and $E_a$ is an apparent activation energy. In this rate law, $A, E_a$, and $V^\infty$ are adjustable parameters that vary with heating rate, pressure, and coal type. At the outset, it is important to realize that their magnitudes have no mechanistic significance whatsoever, because this simple reaction rate expression cannot possibly represent the numerous mechanisms that, in actuality, govern the kinetics of coal devolatilization. The premise that coal contains a fixed amount of precursors to volatiles, $V^\infty$, is implicit in the SFOR yet, in actuality, ultimate devolatilization yields vary with heating rate, pressure, and coal type in ways that no global expression can depict. Similarly, $A$ and $E_a$ are simply numbers that can faithfully mimic devolatilization kinetics, provided that they are applied within their restricted range of applicability.

The parameters $A, E_a$, and $V^\infty$ are usually assigned from laboratory test data. Instead, we use FLASHCHAIN® to synthesize simulation 'data' that can subsequently be analyzed for rate parameters just like one would analyze test measurements. We first evaluate $\mathrm{d}V/\mathrm{d}t$, $V(t)$, and $V^\infty$ for the operating conditions of interest from the FLASHCHAIN® predictions, then assign $A$ and $E_a$ by rearrangement of the SFOR, as follows

$$\langle k\rangle = A\exp\left(-\frac{E_a}{RT}\right) = \frac{(V^\infty - V(t))}{\dfrac{\mathrm{d}V(t)}{\mathrm{d}t}} \tag{4}$$

where $\langle k\rangle$ is the nominal devolatilization rate. In Eq. (4), the weight loss rate, $\mathrm{d}V/\mathrm{d}t$, is evaluated as the sum of the total rates of tar and gas release from FLASHCHAIN®; $V^\infty$ is the sum of the predicted yields of gas and tar at times long enough to achieve an asymptotic value for the heating rate, pressure and coal sample under consideration; and $V(t)$ is the instantaneous sum of the predicted yields of gas and tar. The thermal history in the simulation specifies the sample temperature at every instant in time, so conventional Arrhenius diagrams can be prepared by plotting the logarithm of $\langle k\rangle$ versus reciprocal temperature.

This same analysis can be applied with any reaction rate law to any of the species predicted with FLASHCHAIN®, including tar, gas, $CO_2$, $H_2O$, CO, hydrocarbons, HCN, total volatile nitrogen species, and char–nitrogen.

The performance of the method is shown in Fig. 23 for the following three cases: (1) The p.f. combustion case is based on the mean thermal history of particles from a CFD simulation of a 1.7 $MW_t$ pilot-scale flame at atmospheric pressure; (2) the entrained-flow coal gasification (EFCG) case is based on the thermal history of 55 μm particles injected into gases at 1600 °C within a 1200 °C chamber at 2.5 MPa; and (3) the PFBC case has 2 mm particles heated at 25 °C/s to 850 °C at 1.5 MPa. All cases are based on a typical hv bituminous coal. Fig. 23 shows both the apparent rate based on the FLASHCHAIN® simulations, according to

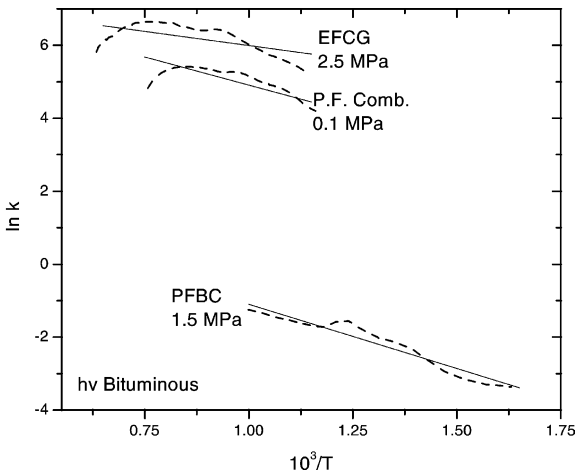


Fig. 23. Arrhenius plot based on rearrangements of the FLASHCHAIN® predictions according to Eq. (4) (dashed curves) and the linear fits based on the SFO (solid lines) for three test conditions described in the text.

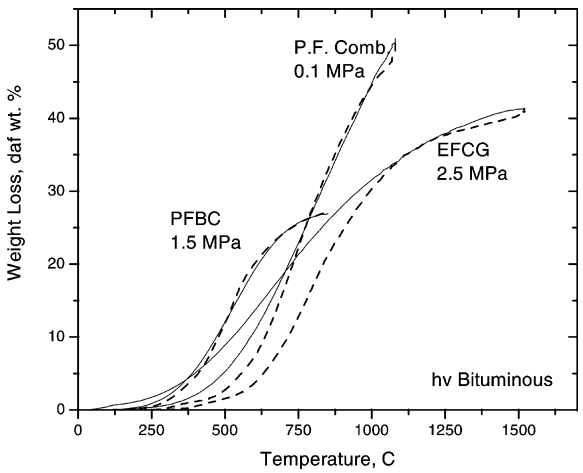


Fig. 24. An evaluation of the transient weight loss during the heating periods based on the SFO assignments in Fig. 23 (solid curves) versus the original FLASHCHAIN® predictions for three test conditions described in the text.

Eq. (4), and the linear fits based on the SFOR for each of the three cases. The apparent SFO frequency factors shift toward higher values for progressively faster heating rates, while the apparent activation energies are hardly affected.

The transient weight loss curves during the heating period based on the SFOR-assignments for the three cases are compared to the original FLASHCHAIN® predictions in Fig. 24. The agreement is nearly exact throughout the PFBC case, and very close at all but the initial stage for the p.f. combustion case. Although the discrepancies are much more substantial for the first half of the EFCG case, this SFOR-based weight loss history eventually relaxes to the FLASHCHAIN® prediction. Hence, the comprehensive devolatilization mechanism directly determines all devolatilization parameters used in complex engineering calculations.

### 2.6.2. Volatiles compositions

Until the serious gaps in the database on detailed product compositions are closed, FLASHCHAIN® provides the most accurate means to estimate volatiles compositions for a broad range of operating conditions. The predicted product distributions from the same hv bituminous coal for the three test cases defined in the previous section are collected in Table 9. Each case has both the products of primary devolatilization as well as the distribution of secondary pyrolysis products. Due to the high processing temperatures in all three test cases, the secondary pyrolysis products would better represent the fuels that are actually converted under these conditions.

In a conventional hv bituminous coal flame, about half the daf-coal mass is released as volatiles, nearly 70% of which is tar. Similar amounts of $H_2$, aliphatic hydrocarbons, and carbon oxides are released from the coal. But secondary volatiles pyrolysis converts nearly all the tar into soot, while eliminating nearly all the aliphatic hydrocarbons and substantially enhancing the yields of $H_2$, CO, and HCN. In an entrained gasifier, the primary products are similar, except that the total and tar yields are 10% lower, and the secondary products are also similar, except for the lower soot yield. But in the PFBC, the same coal releases only one-third the amounts of tar and $H_2$ during primary devolatilization. Similarly, the secondary products contain much less soot and $H_2$, but significantly more $C_2H_2$. There is also more $H_2O$ but less CO and HCN.

Table 9
Predicted distributions of primary and secondary products, in daf wt%, from an hv bituminous coal for three test cases described in the text

| | PF comb, 0.1 MPa | | EFCG, 2.5 MPa | | PFBC, 1.5 MPa | |
|---|---|---|---|---|---|---|
| | Primary | Secondary | Primary | Secondary | Primary | Secondary |
| Tar | 34.9 | 0 | 23.7 | 0.0 | 11.0 | 0.0 |
| Soot | 0 | 31.5 | 0.0 | 21.3 | 0.0 | 9.8 |
| $H_2$ | 1.57 | 4.08 | 2.14 | 4.00 | 0.58 | 1.70 |
| $CH_4$ | 1.5 | 0.21 | 1.60 | 0.23 | 1.70 | 0.24 |
| $C_2H_2$ | 0 | 0 | 0.00 | 0.00 | 0.00 | 1.25 |
| $C_2H_4$ | 0.67 | 0 | 0.70 | 0.00 | 0.74 | 0.00 |
| $C_2H_6$ | 0.24 | 0 | 0.26 | 0.00 | 0.27 | 0.00 |
| $C_3H_6$ | 0.56 | 0 | 0.59 | 0.00 | 0.62 | 0.00 |
| CO | 2.5 | 5.2 | 2.9 | 5.6 | 2.7 | 4.3 |
| $CO_2$ | 2.5 | 2.5 | 2.7 | 2.7 | 2.9 | 2.9 |
| $H_2O$ | 5.2 | 5.2 | 5.7 | 5.7 | 6.1 | 6.1 |
| HCN | 1.02 | 1.87 | 0.76 | 1.33 | 0.27 | 0.53 |
| $H_2S$ | 0.33 | 0.42 | 0.36 | 0.42 | 0.37 | 0.41 |
| Char | 49.1 | | 58.7 | | 72.8 | |

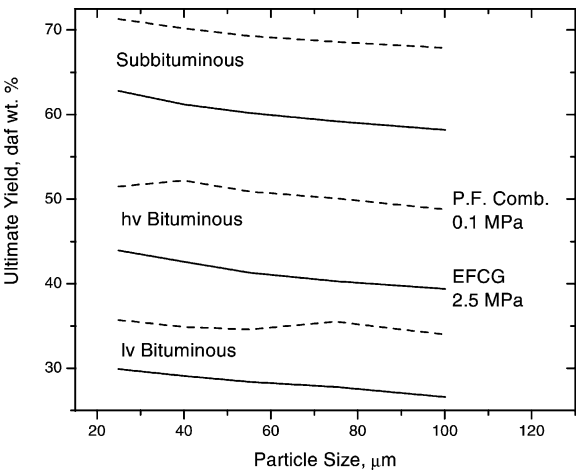


Fig. 25. Predicted ultimate yield versus particle size for three coal types for the p.f. combustion case (dashed curves) and for the EFCG case (solid curves).

*2.6.3. Size effects*

Applications always have broad size distributions for the coal feed, not the monodisperse suspensions used in lab testing. Heating rates become progressively faster for smaller size particles, which can perturb the ultimate yields. The best way to incorporate this effect into complex calculations is to represent the ultimate yield parameter in the SFO as a function of size, based on predictions from FLASHCHAIN® for several discrete sizes. Predictions for the p.f. combustion and EFCG cases for subbituminous, hv bituminous, and lv bituminous coals appear in Fig. 25. The effect is fairly weak, never perturbing the yield by more than 15% across the entire size range. In a similar way, comprehensive devolatilization mechanisms can also be used to develop size-dependent versions of the frequency factors and activation energies in the SFOR, although this would normally not be necessary in most applications.

## 3. Char oxidation at elevated pressures

Oxygen is injected into all types of advanced coal utilization technologies to raise operating temperatures into the specified range. Most of the available $O_2$ is consumed in volatiles combustion and oxidative pyrolysis. But significant amounts can also be used in char oxidation. The reason is connected to the broad PSD of the fuel and the broad range of time scales for devolatilization that is associated with PSDs in entrained flow systems. As long as volatiles are being released, $O_2$ cannot contact the char surface due to the high stoichiometric requirement of volatiles [63]. But once a char is fully devolatilized, it will burn whenever $O_2$ is available because oxygen is the most effective agent for gasification, by far. Note that the mixing intensity of fully devolatilized char into $O_2$-rich gases determines the burnout levels in near-burner zones. The smaller particles are especially likely to burn because they have the shortest devolatilization time scales and therefore the longest times available for dispersion and mixing. The relative burning rates of volatiles and char are also important because, together with mixing intensities, they determine the gas compositions leaving the near-burner zones. Only chars from low-rank coals burn fast enough to effectively compete for $O_2$ with their volatiles [64]. Even so, the degrees of burnout of chars from hv bituminous coals in near-burner zones are probably not negligible.

In this section, the first three subsections describe the available test data on pressurized coal and char oxidation that were used in model evaluations, and illustrate the qualitative tendencies for variable operating conditions. The last three sections describe the validation of a comprehensive mechanism for char oxidation over a wide pressure range.

*3.1. Prerequisites for data on pressurized char oxidation*

To re-create in a laboratory the reaction environment in an entrained coal gasifier, one needs to impose heating rates to $10^5$ °C/s and resolve the dynamics of the char oxidation process at high temperatures and low $O_2$ levels. Due to the relatively long burning times for p.f. chars, the dynamics can be resolved because sampling techniques are available for time scales as short as 10 ms for realistic operating temperatures. Extents of burnout are assigned from measurements of the residual mass of combustibles on a daf-basis, usually by regarding the ash level as a refractory tracer. In pressurized coal combustion testing, time resolution is not the primary hindrance. But there are several other impediments to consider.

The greatest hindrance to laboratory characterization of pressurized coal combustion is in specifying the char particle temperature throughout all the stages of burnout. The initial temperature history is important because we now know that thermal annealing significantly reduces the char oxidation reactivity, and annealing in entrained flow systems is primarily a function of the highest exposure temperature [65]. Accurate temperatures are also important throughout subsequent stages. At intermediate burnout levels, char temperatures are the best means to validate modeling mechanisms for film-diffusion-limited burning. During the later stages, char temperature measurements are the only means to recognize near-extinction, whereby the particle temperature falls by hundreds of degrees as the burning mechanisms shift toward chemical kinetic control [66,67].

The char particle temperature reflects a balance among the burning rate and the associated heat flux and numerous other heat and mass transfer mechanisms. These mechanisms also depend on the particle size as well as various thermophysical properties, such as emittances and heat transfer coefficients, which can change during burnout. This

mechanistic interplay is so complex that temperature estimates based on calculations are subject to large uncertainties, primarily because they are so sensitive to postulated burning mechanisms. Consequently, the weakest data for model evaluations are burnout times at well-defined operating conditions. Adding time-resolved extents of burnout only marginally improves the situation, because burning rates can only be assigned if temperatures are known within tight tolerances.

Char particle temperature measurements together with time-resolved burnout data are sufficient to assign burning rates within useful quantitative tolerances. Due to the essential roles of diffusion, particle size determinations are also very useful in characterizing the mechanisms for burning. Simultaneous determinations of conversion levels, temperature, size, and bulk particle density are primarily responsible for the significant advances in mechanistic modeling for char oxidation achieved during the past decade. The optical diagnostics pioneered in the US for simultaneous determinations of temperature, size, and velocity of individual particles burning at atmospheric pressure have recently been expanded for pressurized applications in US, Germany, and Finland. Detailed technical reports on the American and Finnish work are available but, unfortunately, most of the German work is inaccessible to English readers.

The primary tool used here to analyze the char oxidation database at elevated pressure is CBK/E (extended), a recent version of the Carbon Burnout Kinetics Model (CBK) extended to wide ranges of temperature and pressure by incorporation of the three-step oxidation mechanism of Hurt and Calo [68].

From the standpoint of evaluating CBK/E for applications in entrained-flow gasification, the chars need to be prepared at rapid heating rates. The exposure temperature may be more important than heating rate, per se (although most systems that impose fast heating rates operate at high temperatures). They should also be prepared at elevated pressures, although the impact of pressure on subsequent char oxidation reactivity is just now beginning to be characterized. To characterize the extent of char oxidation, the burnout assigned from the mass fraction of combustibles remaining (on a daf basis) is the most useful conversion index. Supplemental characterization of a char's physical structure is also helpful, particularly if bulk and true densities are monitored over a wide range of burnout. Surface area measurements are less useful because the relevance of total micropore surface area to oxidation rates, especially at high temperatures, has often been questioned [69]. In particular, CBK/E uses mass-specific intrinsic kinetics that do not require specification of total surface area.

More formally, the following testing features are required if a dataset can be used to evaluate CBK/E for pressurized applications.

*Coal properties.* Modeling char oxidation requires, at a minimum, specification of the size, density, and chemical reactivity of the initial char. For studies employing char prepared in a separate pyrolysis step, initial char size and density are needed, and the reduction in reactivity by annealing during the preparation stage must be estimated. For studies involving in situ char formation or where no char properties are reported, the size and density can be estimated from the parent coal density, volatiles yield, and swelling factor. Since swelling factor and coal density are often correlated with the ultimate analysis of the parent coal, and volatiles yields can be predicted from the proximate and ultimate analyses, these coal properties will also be required.

*Pressure.* Usually a uniform test pressure will be specified.

*Oxygen partial pressure.* Uniform $O_2$ levels in the free-stream throughout a combustion history can only be imposed with very dilute coal suspensions, although diminishing profiles of $O_2$ can also be handled in the modeling.

*Thermal history.* Sufficient information must be available to assign the temperature of the sample throughout an entire test. Since the temperature of a burning char particle is intimately coupled to several mechanisms for heat and mass transfer, temperature and size are correlated. Consequently, simultaneous determinations of temperature and size are much more informative than estimates based on modeling.

The previous version of CBK, called CBK8, incorporated correlations for the initial value of char oxidation reactivity in terms of the carbon content of the parent coal, on a daf-basis [70]. This procedure depicts the gross tendencies but cannot depict the sample-to-sample variability in char oxidation rates for a wide range of coals within useful quantitative tolerances. Good test data for a diverse selection of coal chars will be needed to depict the distinctive sample-to-sample variations in the burning rates. Correlations for the initial bulk density of char and swelling correlations that specify the initial char particle size must also be updated for pressurized applications.

Datasets that do not include char temperature measurements can only be used to corroborate model predictions. They do not provide sufficient information to assign burning rates. The combination of burnout data and temperature determinations is sufficient, albeit within the uncertainties associated with simultaneous changes to particle size and density during burning. Time-resolved burnout data with simultaneous determinations of temperature and size are the most stringent means available to evaluate model predictions. In fact, given only simultaneous determinations of particle temperature and size, without any burnout data, one can assign approximate burning rates if the $CO/CO_2$ product ratio is known or can be estimated. But the addition of burnout data circumvents some of the ambiguities in the burning mechanisms. The product of the heterogeneous char oxidation chemistry is ambiguous, shifting from $CO_2$ to CO for progressively higher temperatures. This factor is

Table 10
Database on pressurized coal combustion

| Organization | Country | Reference | Reactor | Coals | $D_p$, μm | $Q_{MAX}$, k°C/s | $T_{MAX}$, °C | $P_{MAX}$, MPa | $X^{O_2}_{max}$ | Monitor[a] |
|---|---|---|---|---|---|---|---|---|---|---|
| VTT | FIN | [71] | EFR | 5 | 85–160 | ca. 100 | 1000 | 1.0 | 0.3 | BO, $T_p$, $D_p$ |
| University of Newcastle | AUS | [72] | EFR | 1 | 63–90 | ca. 100 | 1300 | 1.5 | 0.21 | BO |
| University of Stuttgart | FRG | [73] | EFR | 2 | 160–250 | ca. 100 | 1500 | 0.3 | 0.12 | $T_p$, $D_p$ |
| DMT | FRG | [74] | EFR | 1 | 80, 112, 180 | ca. 100 | 1200 | 2.0 | 0.56 | BO |
| DMT | FRG | [75] | EFR | 3 | 80, 112, 405 | ca. 100 | 800 | 1.5 | 0.21 | BO |
| Brigham Young University | USA | [76] | EFR | 2 | 40, 70 | ca. 100 | 1225 | 1.5 | 0.21 | BO, Q, $T_p$ |
| Riso | DMK | [43] | EFR | 1 | p.f. | ca. 100 | 1000 | 1.53 | 0.054 | BO |
| Eindoven Univ. Tech. | NTH | [77,78] | Shock tube | 2 | 5 | ca. 100 | 1525 | 0.8 | 1.0 | $D_p$, $T_p$, $Q$ |
| Kansas State University | USA | [79] | Shock tube | 2 | 13, 25 | ca. 100 | 1925 | 1.0 | 0.55 | $T_p$, $Q$ |

[a] BO: burnout; $T_p$ : particle temperature; $D_p$ : particle diameter; $Q$ : reaction rate.

important because the heat flux due to char oxidation is very sensitive to the product assignment. Another ambiguity is due to the subsequent homogeneous oxidation of CO. When it occurs in the boundary layers surrounding individual char particles, additional energy will be fed back to the char, which must be accounted for in the overall energy balance for the particle.

### 3.2. Database for pressurized coal and char combustion

A database on pressurized coal combustion that satisfied the above prerequisites was compiled from the literature in English. Fixed bed reactors and thermo-gravimetric analyzers (TGAs) impose very slow heating rates to low temperatures, so their data are not directly relevant to entrained flow or fluidized processing. Therefore, these types of datasets were excluded from the model evaluations.

The database is compiled in Table 10, which lists the performing organization, country, literature citations, the reactor type, the number of tested coals, the particle size range, the heating rate, the maximum temperature, the maximum pressure, the maximum $O_2$ mole fraction, and the char oxidation parameters that were monitored. Nine datasets were located that satisfy most of the prerequisites described previously. Five of them were obtained at universities, with all the rest coming from private or not-for-profit research institutions. This activity is truly international in scope and no single country has contributed a disproportionate share of this research.

#### 3.2.1. Operating characteristics

The database comprises two groups, one each for tests in EFRs and shock tubes. Seven datasets were obtained with EFRs, and two with shock tubes. There are 168 independent tests from EFRs and 53 independent tests from shock tubes. Each test represents a specific total pressure, $O_2$ mole fraction, gas temperature, coal sample and particle size. The domains of the test conditions across both groups are collected in Table 11. Total pressures were varied from 0.1 to 2.0 MPa, with a typical pressure of 1.0 MPa for tests in both groups. This pressure range covers the range for most coal processing technologies, and the coverage of the pressure domain is uniformly fine. Oxygen mole percentages were varied from 0.5 to 100%, with a typical range of 10–21% for tests in EFRs. Gas temperature ranged from 700 to 1527 °C, covering the typical range in entrained flow and fluidized bed gasifiers. Particle sizes ranged from 4 to 500 μm, but fell into separate ranges for shock tubes and EFRs. All the shock tube tests used sizes of 4–5 μm, whereas the EFR tests used sizes from 70 to 500 μm, with a typical value of 125 μm.

#### 3.2.2. Coal quality

The database represents 11 different coals plus two chars, including ranks from lignite through lv bituminous coal. Most of the datasets have the required proximate and ultimate analyses. Only those coals used by DMT were not completely described. For the Westerholt coal used at DMT, we used the proximate and ultimate analysis for the same coal reported elsewhere [80]. The data on the Liebenburen anthracite used in Muhlen and Schulte [75] had to be omitted, because the coal properties were not reported.

Table 11
Domain of test conditions

| Variable | Range | Typical value |
|---|---|---|
| Pressure, MPa | 0.1–2.0 | 1.0 |
| $O_2$ mole fraction, % | 0.5–100 | 21 |
| Gas temperature, °C | 700–1527 | 1100 |
| Particle size, μm | 4–500 | 4 (shock tube) and 125 (EFR) |

The database represents virtually the entire coal rank spectrum, albeit nonuniformly. Nine coals were tested in EFRs and four were tested in shock tubes. The range of coal quality is shown in two ways in Fig. 26. The upper panel is a coalification diagram, which plots the atomic H/C ratio versus the atomic O/C ratio. The coals tested in EFRs and shock tubes are concentrated in the hv bituminous rank; otherwise, there were only a few subbituminous coals and a few anthracites.

The plot of the proximate volatile matter contents versus carbon content in the lower panel of Fig. 26 underscores the concentration of hv bituminous coals in both EFRs and shock tubes, and the generally poor coverage of low volatility coals and subbituminous coals. The poor coverage of low volatility coals and subbituminous coals needs to be rectified in future testing programs.

### 3.2.3. Reported combustion characteristics

The EFR test results were reported in a variety of forms, including measurements of particle temperatures, residence times, particle size and extents of burnout. One of the EFR datasets [71] reported complete measurements of particle temperature, residence time, burnout and particle size, which enable stringent model validations. Another [76] reported all these measurements except for particle size. Another dataset [73] reported the measured particle temperature and particle size at a specified residence time. The other four EFR datasets only reported the burnout levels as a function of residence time. Surface reaction rates (g/cm$^2$ s) and particle temperatures of coal or char were the reported measurements in all shock tube tests. The rates were calculated through particle size variations. Lester et al. [79] measured the initial burning rate of coal at an extremely short residence time after the ignition of coal particles. Banin et al. [77,78] calculated the surface reaction rate through direct measurements of the variation in particle size. In their reports, both particle temperature and reaction rate were assigned for each specific run, which were used in our evaluations.

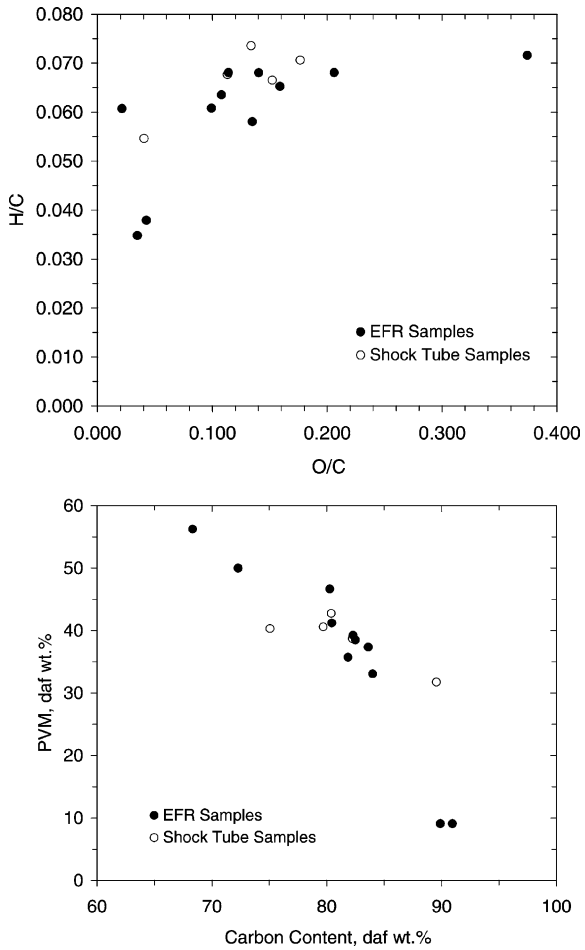


Fig. 26. (Top) Coalification diagram and (Bottom) proximate volatile matter contents of coals tested in EFRs (●) and shock tubes (○).

### 3.3. Observed impacts of the test conditions

This section illustrates the most important qualitative trends in the combustion characteristics with selected datasets, beginning with the impact of total pressure on char burnout and the char burning rate.

### 3.3.1. Pressure effect

The simplest situation is shown in Fig. 27. Since the coal particle size was large, from 315 to 500 μm, char oxidation under the test conditions is expected to be limited by $O_2$ diffusion across the boundary layer surrounding the particle. At a constant $O_2$ mole fraction, the diffusion rate is independent of total pressure, so burnout should also become independent of pressure in the limit of film-diffusion control. Indeed, the reported extents of burnout

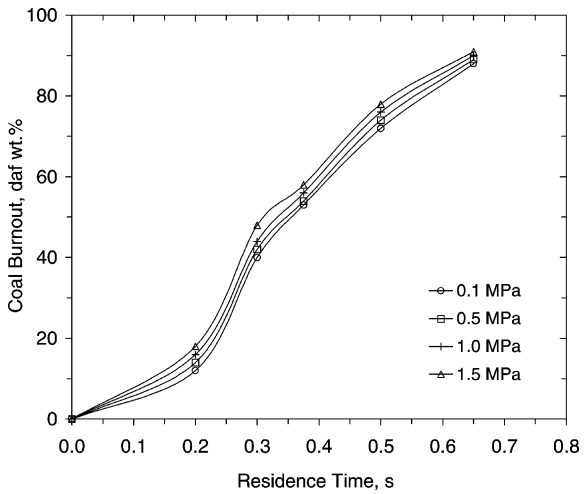


Fig. 27. Burnout history of a hv bituminous coal in an EFR at 21%$O_2$ and 800 °C [75].

increase slightly while the total pressure was increased from 0.1 to 1.5 MPa, consistent with this simple interpretation.

The burnout of a variety of coals representing three main segments of the rank spectrum appears in the upper panel of Fig. 28. Burnout measurements for each coal were taken at the same residence time in an EFR [71], although nominal residence times vary among the various coals. The burnout of one of the lignites is independent of total pressure, consistent with a strictly diffusion-limited burning rate. Since lignite chars have the highest intrinsic char oxidation reactivities, film diffusion might be expected to closely approach the theoretical Zone III limit. Apparently the situation is more complicated, because the burnout of the other lignite char in Fig. 28 exhibits a fairly strong pressure dependence. Similarly, the burnout of one of the hv bituminous chars is independent of pressure through 0.5 MPa, then becomes higher for progressively higher pressures. But the burnout of the other hv bituminous char is

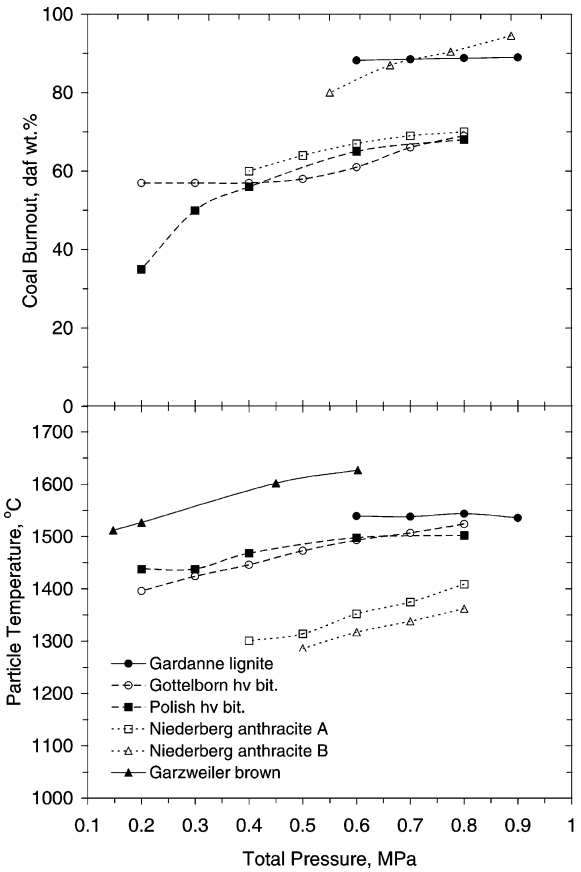


Fig. 28. (Upper) Burnout and (Lower) particle temperatures of a variety of coals in EFRs. From Joutsenoja et al. [71]: (●) Lignite at ($T_g$ = 877 °C, $O_2$ = 10% and at 130 ms); (○) hv bit. coal at (897 °C, 10%, 80 ms); (■) hv bit. coal at (887 °C, 10%, 100 ms); (□) anthracite A at (997 °C, 10%, 370 ms); (△) anthracite B at (997 °C, 10%, 300 ms); and from Reichelt et al. [73]: (▲) brown coal (1000 °C, 12%, 250 ms).

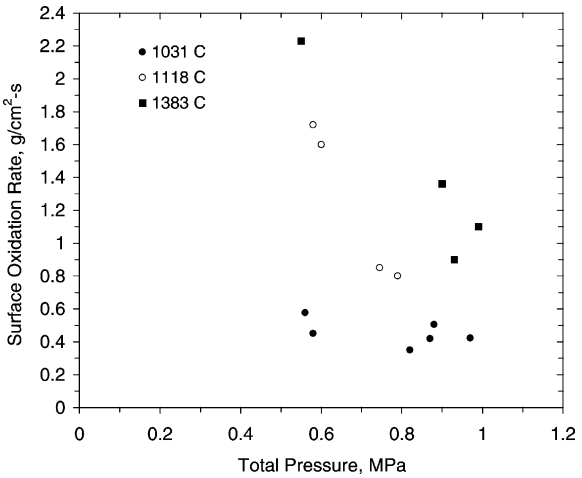


Fig. 29. Impact of total pressure on surface oxidation rate of Ill. #6 coal samples in a shock tube at various gas temperatures [79].

especially sensitive to pressures below 0.5 MPa, then becomes insensitive to further increases in the pressure. Compared to the lignite char, the bituminous and anthracite chars are converted at slower, albeit similar, burning rates for pressures above 0.25 MPa. The particles always burn hotter for progressively higher pressures, except for the lignite whose burning rate was film-diffusion-limited.

The pressure dependence appears to invert for very small particles, as seen in the oxidation rate assigned from shock tube data in Fig. 29 [79]. The particles in these tests were as small as 4 μm, for which burning rates under these test conditions would probably be limited by a combination of pore diffusion and chemical reaction. If so, then a major portion of the internal surface area would participate in the oxidation. The reported oxidation rates decreased for higher total pressures, especially at the higher gas temperatures. The authors attribute this tendency to variations in the plasticity of the nascent chars during their devolatilization, but all the test pressures are above the threshold for limiting, high-pressure asymptotic devolatilization behavior. Taken at face value, these data appear to indicate that small particles of char prepared at progressively higher pressures have lower surface areas, but this inference needs to be confirmed with further characterizations.

### 3.3.2. Oxygen level

The impact of variations in the $O_2$ level on char combustion is clearly apparent in the database, especially in several studies in which the oxygen concentration was varied at uniform total pressure and reactor temperature. For example, Fig. 30 shows the burnout profiles for Westerholt coal in an EFR at a total pressure of 1.5 MPa and a reactor temperature of 1200 °C. Although the number of data points for each gas condition is limited, the char burned much faster for progressively higher $O_2$ levels. In 7.5% $O_2$, burnout was almost complete in less than 300 ms, whereas

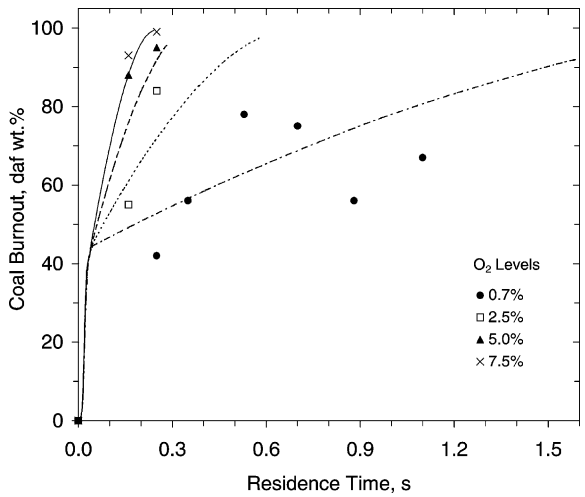


Fig. 30. Coal burnout profiles of Westerholt coal in an EFR at 1.5 MPa and 1200 °C with various $O_2$ levels [74].

a residence time well over a second was insufficient with 0.7% $O_2$. Large particles, such as those used in these tests, are expected to burn at or near rates limited by film diffusion. Since the bulk diffusion rate is proportional to the $O_2$ concentration at a constant total pressure, the overall diffusion-limited burning rate is proportional to $O_2$ concentration for a constant $CO/CO_2$ ratio.

### 3.3.3. Gas temperature

Three datasets, two from EFRs and one from a shock tube, directly characterize the impact of gas temperature variations on coal combustion characteristics. Char burnout profiles for Utah coal char at a total pressure of 0.5 MPa and an $O_2$ level of 10% appear in Fig. 31. Although the number of points in each burnout profile is limited, the extent of

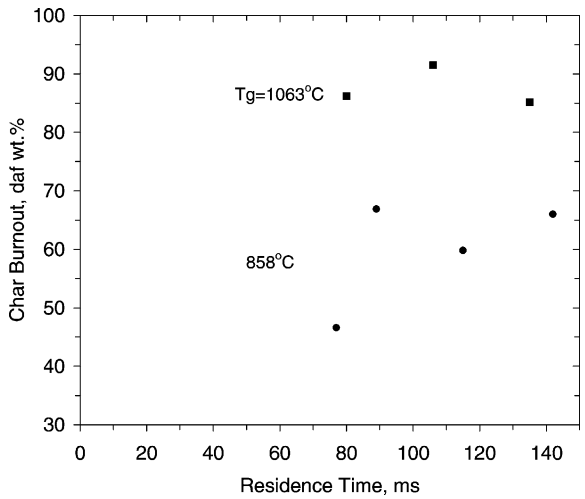


Fig. 31. Impact of gas temperature on char burnout in an EFR at 0.5 MPa and 10% $O_2$ and two gas temperatures [76].

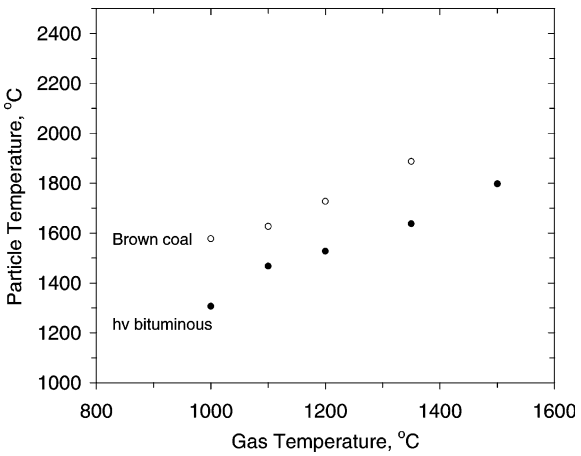


Fig. 32. Impact of gas temperature on the particle temperatures at 200 ms of brown coal (○) and hv bituminous coal (●) in an EFR at 0.3 MPa with 10% $O_2$ [73].

burnout increases for higher gas temperatures, as expected. At 858 °C, approximately 65% char burnout was achieved after 140 ms, whereas 90% burnout was achieved at 1063 °C after only 100 ms. According to the energy balance for a burning particle, a hotter gas temperature produces a hotter particle temperature, hence a faster burning rate. Fig. 32 shows this tendency with the particle temperatures monitored during combustion of hv bituminous and brown coals in an EFR. The particle temperatures increased from 1300 to 1800 °C for the bituminous coal when the gas temperature was increased from 1000 to 1500 °C. The same trend was observed for brown coal, albeit for the hotter particle temperatures associated with the more reactive low rank char.

### 3.3.4. Coal quality and particle size impacts

Unfortunately, the database does not directly characterize the impact of particle size variations, due to uncontrolled variations among the other test conditions while size was also varied. According to classical char combustion theory, the burning rate (per unit external surface area) becomes independent of size when it is limited by the intrinsic char oxidation kinetics, and inversely proportional to size when it is film-diffusion-limited.

The impact of coal quality is among the strongest influences on char oxidation at atmospheric pressure, and char burning rates diminish for coals of progressively higher rank. Among all datasets on char oxidation at elevated pressures, four tested two coals, one tested three coals and one used five coals. But the test conditions were widely variable so it is difficult to isolate the coal quality impacts for a broad segment of the rank spectrum. As seen in the previous illustrations, low rank chars tend to be the most reactive, exhibiting high particle temperatures and fast burning rates.

### 3.4. Mechanistic interpretations

A variety of reaction orders are in current use in atmospheric coal combustion modeling including global orders of 1 or 1/2, intrinsic reaction orders of 1, 0.5, or 0, and variable order expressions such as Langmuir kinetics. Note that most atmospheric char combustion occurs between Zones II and III, where the equivalence law between global order and intrinsic order is given by: $n_{global} = (n_{intrinsic} + 1)/2$. The reaction order is often difficult to extract from flame data, and in some cases authors report successful fits to the same atmospheric data set using quite different values of the reaction order. It is arguable that accurate knowledge of the order is not critical for char combustion modeling over the relatively narrow range of partial pressures in atmospheric p.f. firing. In this case the lack of agreement about reaction order may not represent a problem for atmospheric combustion modeling. Extending predictive models to higher pressures, however, requires more accurate knowledge of the reaction order, since it directly expresses the dependence of the intrinsic chemical rate on the primary variable, oxygen pressure.

Examination of the more fundamental literature on carbon/oxygen surface kinetics reveals a complex picture, in which reaction order is typically high (0.6–1) at low temperatures ($<727$ °C), while at high temperatures ($>927$ °C) the most commonly invoked intrinsic reaction order is zero [68]. The high temperature reaction order is subject to considerable uncertainly, as it can only be determined by model extraction from flame data in Zone II or above, where it represents only one of several unknown parameters. Nevertheless, the existing database strongly suggests an apparent transition from high to low order as temperature increases. This behavior cannot be captured by models assuming constant order or by simple Langmuir kinetics, which predict the opposite behavior (low order at low temperature; high order at high temperature).

A simple, three-step, quasi-global kinetic mechanism has been proposed to capture this trend in a simple submodel for use in flame codes [68]. These kinetics were incorporated into the reaction framework for the CBK model, and then implemented it in a new version called ‘CBK/E’. The added suffix denotes ‘Extended,’ in reference to the extended domain of operating conditions, both pressure and temperature, that the new kinetics can represent.

In this section, we briefly review the mechanisms included in CBK/E, then focus on all the rate parameters that must be assigned in the model evaluations.

#### 3.4.1. Overview of CBK/E

CBK is a kinetics package that describes char oxidation under conditions relevant to p.f. firing. It has been developed by Hurt and co-workers both at Sandia National Laboratories, Livermore and currently, at Brown University. Detailed publications on the earlier versions of CBK are available [81–83], and the technical basis for the rate expression in CBK/E has been described by Hurt and Calo [68]. The mechanism describes the rate of burning, the char particle temperature, and the changes in the particle diameter as combustion proceeds, given a gas temperature, radiative exchange temperature, and oxygen partial pressure. It is specially designed for carbon burnout applications, because it treats the late stages of char combustion in detail.

Within the theory, char reactivity is a dynamic function of heat treatment severity, based on a distributed activation energy model of thermal annealing. The thermal annealing mechanism acts to destroy active oxidation sites during heat-up and devolatilization, and throughout combustion. The annealing kinetics are so fast that the maximum temperature often determines the extent of reduction of the intrinsic reactivity. The theory uses mass-specific intrinsic kinetics, and earlier versions emphasized the statistical variability of intrinsic char oxidation reactivity. There is a standard model of the reaction/diffusion process within porous char particles, and the ‘one-film’ description of the boundary layer processes which accounts for bulk (Stefan) flow and continuum diffusion but ignores all chemistry in the gas phase. The code also includes a model of the effect of ash inhibition in the late stages of combustion. Together, these mechanisms act to significantly reduce char conversion rates during the later stages of combustion, in accord with observations of very long reaction times for conversion of the last few percentage points of the char mass.

The transport rate of $O_2$ to the char surface is determined by bulk diffusion through an external boundary layer, in series with pore diffusion through an ash layer that forms over the char surface during the later stages, in series with pore diffusion through the pore system of the carbonaceous char core. These transport mechanisms must balance the consumption of $O_2$ in the chemical mechanism for oxidation, which was previously represented with an $n$th order global rate expression. Now a three-step quasi-global surface reaction mechanism has been incorporated. The interplay among the transport and chemical reaction mechanisms automatically determines whether burning rates are governed by the chemical kinetics (Zone I), internal pore diffusion (Zone II), or external film diffusion (Zone III). Under typical p.f. firing conditions, this intrinsic formulation quickly shifts from Zone I during the ignition stage to Zone III during quasi-steady combustion at the hottest particle temperatures. As the particle burns, the core of remaining combustible material shrinks, so the burning regime can shift back into Zone I, in which $O_2$ completely penetrates the internal pore structure and both external film and intraparticle diffusion resistances are negligible.

The intrinsic formulation also allows more accurate extrapolation of the primary high temperature data on which CBK is based to lower temperatures. Although CBK is not specifically designed for predictions far outside the pc-combustion regime, it has been found to yield useful predictions at temperatures as low as 500 °C and is reasonably consistent with TGA data. As an option,

the theory contains fuel-general correlations for each of the reactivity parameters, so that predictions can be made knowing only the proximate and ultimate analyses of the parent coal.

CBK/E includes all the same transport-related and annealing mechanisms, including single-film char combustion, intraparticle reaction/diffusion, thermal annealing, and ash inhibition. The new three-step intrinsic kinetics resolves the problems in the reaction order for conventional char oxidation kinetics. They are based on the following reactions:

1. $C + O_2 \rightarrow 2C(O)$ (5)
2. $C(O) + O_2 \rightarrow CO_2 + C(O)$
3. $C(O) \rightarrow CO$

The corresponding rate laws for each step are:

$$R_1 = k_1 P_{O_2}(1 - \theta) \quad (6)$$

$$R_2 = k_2 P_{O_2} \theta$$

$$R_3 = k_3 \theta$$

where $\theta$ represents the fraction of sites occupied by the adsorbed oxygen complex, $P_{O_2}$ is the $O_2$ partial pressure on the carbon surface, and, $k_1, k_2$ and $k_3$ denote the rate constants for Step 1, Step 2 and Step 3 in Eq. (5), respectively.

These laws can be combined to yield the steady-state expression for the overall oxidation rate and primary CO/$CO_2$ ratio, which are

$$r_{gas} = \frac{k_1 k_2 P_{O_2}^2 + k_1 k_3 P_{O_2}}{k_1 P_{O_2} + k_3/2} \quad (7)$$

$$\frac{CO}{CO_2} = \frac{k_3}{k_2 P_{O_2}} \quad (8)$$

An effectiveness factor is required when oxygen transport through the pores becomes a rate controlling mechanism at high particle temperatures. Due to the complexity of the rate law, an analytical solution for the effectiveness factor is not available, so a generalized modulus approach was incorporated into CBK/E [84].

In addition to the new intrinsic kinetics, CBK/E also incorporates the following new correlation for coal swelling ratio [85], in which the operating pressure is involved:

$$Sw = \begin{cases} Sw_1^{0.7143+2.857P_T}, & 0.1 \le P_T \le 0.8 \\ Sw_1^{3.5-0.625P_T}, & 0.8 \le P_T \le 4.0 \end{cases} \quad (9a)$$

where $P_T$ is the total pressure in MPa and $Sw_1$ represents the swelling ratio at atmospheric pressure, which is evaluated from

$$Sw_1 = \begin{cases} 8.67 - 0.0833 C_{daf}, & 89 \le C_{daf} \le 92, \\ -0.0458 + 0.01459 C_{daf}, & 72 \le C_{daf} < 89, \\ 1.0, & C_{daf} < 72 \end{cases} \quad (9b)$$

where $C_{daf}$ denotes the daf carbon content of the parent coal.

*3.4.2. Rate parameters in CBK/E*

The rate constants, $k_1, k_2$, and $k_3$ in Eq. (6), are each of Arrhenius form, so each rate contains a pre-exponential factor $A$ and an activation energy $E$. We first explain the assignment of pre-exponential factors, then of the activation energies.

In CBK/E, the initial (pre-annealing) pre-exponential factor for $k_3$ (Step 3), called $A_{30}$, is used to normalize the pre-exponential factors in $k_1$ and $k_2$. This variable is the primary indicator of reactivity and the most important fuel-specific variable in the mechanism, because Step 3 is typically the rate controlling step at high temperatures. The other rate constants are tied to $A_{30}$ so that changing its value alone will alter all the rate constants proportionally. In this way $A_{30}$ represents a 'reactivity' and does not determine the controlling step (and thus the effective order and effective activation energy). The controlling mechanism is determined rather by the subsequent parameters $A_{20}/A_{30}$ (a ratio of the pre-exponential factors in $k_2$ and $k_3$) and $A_{30}/A_{10}$ (a ratio of the pre-exponential factors in $k_3$ and $k_1$). Based on the same philosophy, annealing in CBK/E acts on all rate constants simultaneously. There is insufficient information in the current database to support separate effects of annealing or rank on $k_1, k_2$, and $k_3$.

The pre-exponential factor for $k_2$ can be obtained through the ratio of the pre-exponential factors in $k_2$ and $k_3$ in the semi-global mechanism, denoted by $A_{20}/A_{30}$. Step 2 is the oxygen/complex reaction which is responsible for high effective reaction orders at lower temperatures and higher oxygen partial pressures. It is certainly needed to model oxidation behavior below 727 °C and may play a smaller role at higher temperatures—it remains to be seen if data above 727 °C can only be represented by nonzero reaction orders. Rate parameters should be assigned to cause a transition from zero order to higher orders as temperature falls below about 627 °C. The default assignment for $A_{20}/A_{30}$ is $5.0 \times 10^4$ which, in combination with the other default rate parameters, correctly located the transition. To accentuate nonzero order behavior above 727 °C, $A_{20}/A_{30}$ can be increased by adjusting $E_2$.

Similarly, the pre-exponential factor for $k_1$ can be obtained through the ratio, $A_{30}/A_{10}$. Step 1 is the adsorption reaction whose influence yields high effective reaction orders, typically at high temperatures and low $O_2$ partial pressures. At this time it is not clear if or when it is needed to model practical combustion—the literature provides conflicting opinions. If the transition to adsorption control occurs at very high temperature, it will coincide with the regime of boundary layer diffusion limitations where the rate law loses its significance for practical prediction. We started with $A_{30}/A_{10} = 1.0 \times 10^{-6}$, which when used with the other defaults has no effect on predictions. With this parameter set, adsorption (Step 1) will not limit the reaction until very high temperatures. If the data present evidence of a transition toward higher orders (and low activation energies) as temperature increases in the high temperature

regime, this parameter can be increased as needed (which decreases $k_2$ and makes it more likely to limit the rate).

$E_3$ is the activation energy for Step 3 in the semi-global mechanism. Because of the exponential form of the Arrhenius law it has a large effect on predictions. The default value of 133.8 kJ/mol was assigned to give reasonable predictions in both the high temperature regime and for TGA air oxidation at 500 °C. $E_2$ is the activation energy for Step 2, and also affects predictions at lower temperatures. Its primary function would be in fitting lower temperature data in the tail of the flame. $E_2$ should be kept below $E_3$ to preserve the proper qualitative behavior—the transition toward lower order as temperature increases in the low temperature regime. The default value for $E_2$ is 117 kJ/mol, which is within the range of values assigned to two different chars in a recent high-pressure kinetic study [86]. $E_1$ is the activation energy for adsorption (Step 1). It is recommended to use the default value of 25 kJ/mol unless there is evidence of adsorption control at high temperature, and the adjustment of $A_{30}/A_{10}$ is not fully sufficient to model that regime. With these default values, the model yields the limiting cases listed in Table 12. The model provides an adequate fit to the observed global reaction order data, and the behavior can even be compared with the observations in some specific cases described in Ref. [68].

In addition to the rate constants in CBK/E, a power-law exponent that relates density changes to the extent of burnout must be specified. This parameter, denoted by $\alpha$, is set to zero for shrinking core behavior (at constant density) and unity for burnout at constant size with variable density. Alpha was specified as 0.2 for all cases in this paper, which is the best fit value for CBK8 simulations at atmospheric pressure.

In the validation sections to follow, only $A_{30}$ was adjusted to fit the observed data, while the default values were used for all other parameters. This approach is thought to be the most effective method to evaluate and compare the datasets from different sources. Once validated, this approach demonstrates that CBK/E is able to predict coal oxidation behavior for any coal with only one adjustable parameter, even while its more complex kinetics circumvent the major deficiencies of *n*th order intrinsic kinetics.

Table 12
Summary of controlling mechanisms and rate expressions for each temperature range [68]

| Particle temperature range | Simplified burning rate | Controlling mechanisms |
|---|---|---|
| Low temperature: ($k_3$ small) | $r_{gas} = k_2 P_{O_2}$ | $O_2$-complex reaction control |
| Very high temperature: ($k_3$ large) | $r_{gas} = 2k_1 P_{O_2}$ | Adsorption control |
| Low-moderate temperature ($k_1 P_{O_2} \gg k_3$) | $r_{gas} = k_2 P_{O_2} + k_3$ | Mixed desorption/$O_2$/complex control |
| Moderate temperature ($k_1 P_{O_2} \gg k_3 \gg k_2 P_{O_2}$) | $r_{gas} = k_3$ | Desorption control |
| High-moderate temperature ($k_1 P_{O_2}$, $k_3 \gg k_2 P_{O_2}$) | $r_{gas} = \dfrac{k_1 k_3 P_{O_2}}{k_1 P_{O_2} + k_3/2}$ | Langmuir–Hinshelwood-type, mixed adsorption/desorption control |

### 3.5. Data evaluations

We first briefly describe the simulation procedures, then present the evaluations with each of the EFR and shock tube datasets in the database.

#### 3.5.1. Simulation procedures

CBK/E was first incorporated into PC Coal Lab®, which is a comprehensive computer package used for simulating complete combustion of individual particles of any coal type at any operating conditions. PC Coal Lab® incorporates FLASHCHAIN® for devolatilization [58], a simple mechanism for volatiles combustion that accounts for energy feedback from the volatiles flame [63], and CBK/E for char oxidation.

All rate parameters in CBK/E were set to their default values, except $A_{30}$. The value for $A_{30}$ was adjusted to match the CBK/E prediction to the reported combustion behavior for each test case in a dataset, starting with values between $1.0 \times 10^7$ and $1.0 \times 10^9$. Iterations were continued until the error between the predicted and reported behavior was less than 5%. Then the assigned values for all cases were averaged to assign the best-fit value of $A_{30}$ for that particular fuel. The best-fit values for all fuels in the database were then used to develop a rank-dependent correlation to estimate $A_{30}$ (Section 3.6.1) for generalized applications.

An early version of CBK/E was found to underpredict low-rank coal burnout, even when reactivities were set high enough to produce diffusion-limited rates. We believe the underprediction of the diffusion-limited rate was due to omission of the following factors.

*Nonsphericity.* There have been a number of studies of nonsphericity [87,88], which is most important for biomass, but may also play a role for low-rank coals that do not soften. A recent example is the study of Gera et al. [89] in which they use the mathematical model for ellipsoidal forms. A typical enhancement of burning rates is 20% for biomass with $L/D = 3$, which is significantly greater than the estimates for nonspherical coal particles.

*Fragmentation.* CBK/E does not account for fragmentation, but it has been observed in flow reactors that impose very rapid heating rates. Mitchell and Akanetuk [90] reported evidence for fragmentation during both devolatilization and char combustion, with more occurring during devolatilization. Such early fragmentation could significantly enhance the mass loss rates of combustibles in the early-to-mid-conversion range. Unfortunately, no reliable, quantitative models are available.

*Surface voids.* Oxygen may penetrate into large surface voids and onto the walls of these voids, which will enhance the burning rate in the film diffusion-limited regime [91]. The enhancement of burning rates is significant when the surface pores are deeper than their radius.

*Gasification reactions.* Simultaneous gasification of char by $CO_2$ and $H_2O$ occur during p.f. combustion [92], and can enhance burning rates by 0.7% in 6% water vapor. Typically, gasification would contribute about 2% to the extent of burnout with 17% water vapor.

*Convection.* Deviations in the *Sh* and *Nu* numbers due to the slip velocity from the stagnant gas limit of 2.0 follow the Ranz-Marshall correlation. For 100 μm particles with typical densities and gas properties, burning rates would be enhanced by 3% by this factor.

It is not feasible to incorporate all these mechanisms in CBK/E to predict the enhanced diffusion-limited burning rates for low rank coals, because each mechanism would introduce uncharacterized adjustable parameters. Instead, an overall transport enhancement factor was introduced to match the predicted and observed burnout histories for the cases with diffusion-limited burning rates. The best-fit value was 1.84. All the CBK/E calculations for all fuels in this paper are based on this value of the factor.

The criterion for evaluating the model predictions is the SSE as defined in Eq. (2) in Section 2.5. The number of independent modeling factors is easiest to specify when the model is a multivariate regression; however, it is ambiguous with mechanistic models like CBK/E. Throughout all the evaluations in this report, $n_F$ was specified as 5 to account for the variations in pressure, $O_2$ level, gas temperature, reaction time, and coal quality. Since $n_S$ is so much greater than unity, the specification on $n_F$ is unimportant.

### 3.5.2. EFR evaluations

This section presents the evaluations of CBK/E predictions with all the EFR data. The predictions are based on the coal's proximate and ultimate analyses, the initial particle temperature, gas temperature, total pressure, $O_2$ level, reaction time and particle size. A parity plot for the burnout predictions for the EFR database appears in Fig. 33. The predictions are based on the best-fit assignment for $A_{30}$ for each coal, but not for each individual test condition. The scatter is substantial over the whole range of burnout, and the model tends to overpredict burnout levels under 60% and underpredict levels over 80%. Nevertheless, the SSE for the burnout prediction is 11.4 daf wt%, so the predictions remain within useful quantitative tolerances. Case studies on each of the EFR evaluations are presented below.

*3.5.2.1. BYU dataset.* Char oxidation experiments at Brigham Young University (BYU) [76] used a Utah bituminous coal char that was prepared at atmospheric pressure in a drop-tube furnace. The char was then fed into a high-pressure, controlled-temperature profile, drop-tube reactor at pressures of 0.1, 0.5, 1.0 and 1.5 MPa. Reactor temperatures were varied from 733 to 1227 °C and the oxygen level was varied between 5 and 21% for a wide range of residence times. Extents of char burnout and particle temperatures were reported for each case.

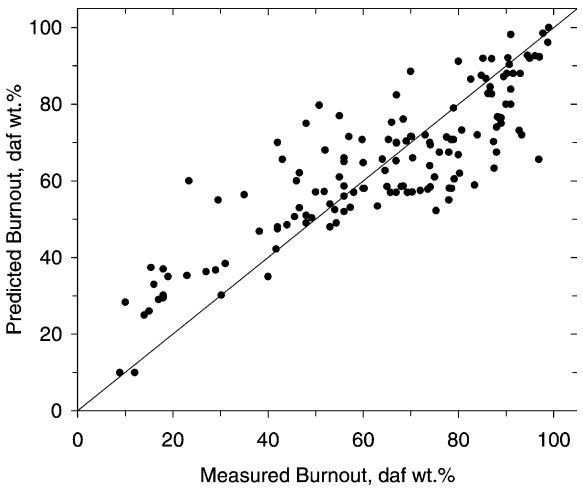


Fig. 33. Parity plot of burnout predictions for the EFR database based on the best-fit parameter assignment for $A_{30}$ for each coal.

For these tests, the PC Coal Lab® simulations used an initial char yield of 57 daf wt%, as reported [76], and predicted only the char oxidation stage. The assigned $A_{30}$ value was $1.0 \times 10^8$.

The parity plot for the burnout prediction for Utah char appears in Fig. 34. Although the scatter appears excessive, there is actually a systematic deviation in the predictions for progressively higher pressures. The predictions at 0.1 and 0.5 MPa are within experimental uncertainty across the entire range of measured burnout. At 1.0 MPa, low levels of burnout are overpredicted and high levels are underpredicted. The experiments conducted at 1.5 MPa had

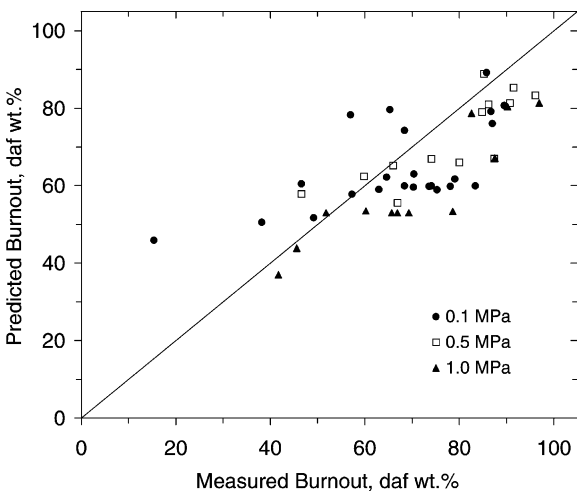


Fig. 34. Parity plots for burnout predictions for the EFR dataset with Utah coal char based on the best-fit parameter assignment [76].

extremely low wall temperatures and low gas temperatures, and hence were not included for comparison due to severe ignition problems [93].

*3.5.2.2. VTT dataset*. The most comprehensive EFR measurements were reported by VTT, Finland [71]. A sizing pyrometer was used for simultaneous in situ measurement of the temperatures and sizes of individual particles. The dataset represents gas temperatures from 877 to 1000 °C, total pressure from 0.2 to 1.0 MPa, and $O_2$ concentrations from 3 to 30%. Measurements were taken with five coals representing ranks from lignite to anthracite. Average particle temperatures and average extents of burnout were determined from the primary single-particle measurements. For the evaluation with this dataset, the initial coal particle size of each fuel was adjusted in a one-point calibration procedure to match the measured sizes for that fuel.

The parity plot for the burnout predictions appears in the upper panel of Fig. 35. The SSE for burnout predictions over all runs is 9.2 daf wt%, and the only systematic discrepancy is a slight overprediction for extents of burnout below 50%. The accuracy of the predictions is the same for all fuels. The predicted particle temperatures have large discrepancies with the measured values. With all coals, the predicted temperatures at low burnout levels are in good agreement, except for the anthracites whose temperatures are underpredicted by 200–250 °C. Particle temperatures were overpredicted for one of the anthracites and under-predicted for one of the bituminous chars at high burnout levels. The particle size predictions are scattered but reasonably accurate over the test domain, reflecting the one-point calibration for each fuel.

Under these test conditions, the char burning rate was determined by film-diffusion for the lignite. Consequently, there was insufficient sensitivity to assign values of $A_{30}$ from the burning rates for this coal. The respective best-fit values were $3.0 \times 10^7$ and $5.0 \times 10^7$ for the two anthracites, and $6.0 \times 10^7$ and $1.5 \times 10^8$ for the bituminous coals.

*3.5.2.3. IVD dataset*. The dataset collected in the EFR at IVD at University of Stuttgart in Germany [73] has similar measurements to those in VTT dataset, except that no burnout profiles were reported and only two coals, a brown coal and a hv bituminous coal, were tested. Only particle temperatures and sizes were measured. Preliminary simulations for the brown coal indicated that the predicted particle sizes for the residence times in the evaluation were smaller than the observed values, and also much smaller than the initial sizes. The initial size was adjusted to obtain agreement with the measured sizes at the evaluation conditions. Since the errors in the predicted sizes for the bituminous coal were small, the size calibration was only applied in the brown coal simulations.

Fig. 36 shows a parity plot for the predicted particle temperatures. The agreement is virtually exact for the hv bituminous coal, whereas the predicted temperatures for

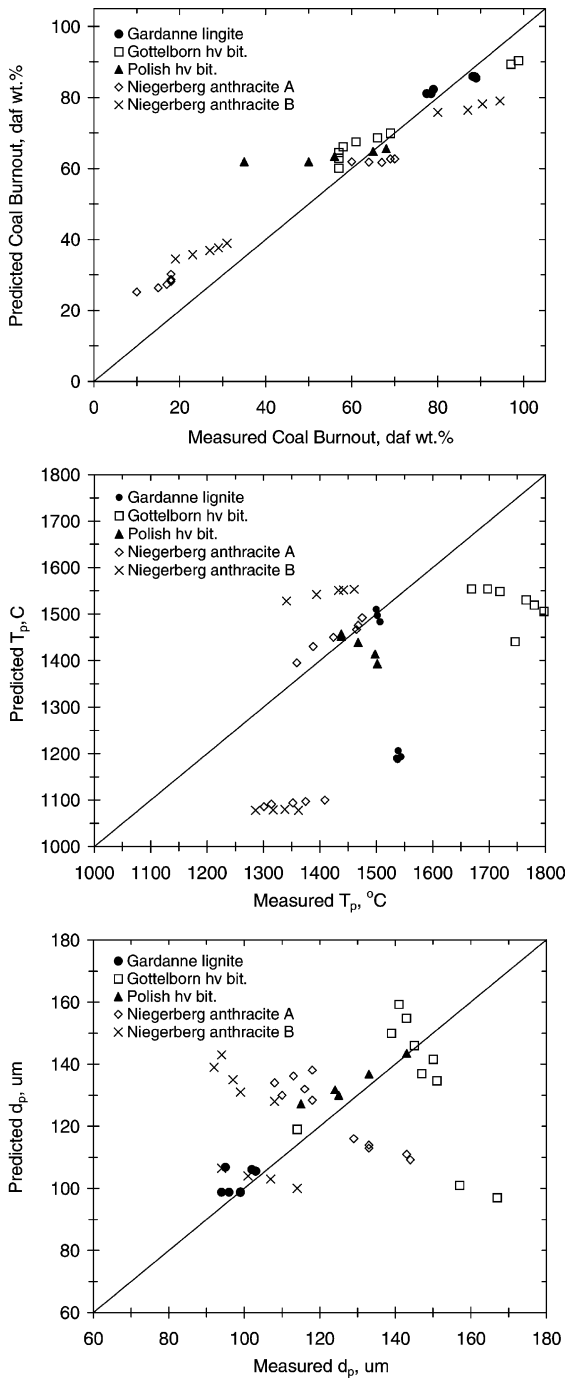


Fig. 35. Parity plots of (Upper) burnout, (Middle) $T_P$, and (Lower) $d_p$ predictions for five coals in an EFR at VTT [71].

the brown coal are high by 100 °C. The best-fit value of $A_{30}$ is $4.0 \times 10^7$ for the bituminous coal and $3.0 \times 10^8$ for the brown coal.

The evaluation of the predicted particle size in Table 13 shows good agreement for the brown coal, due to

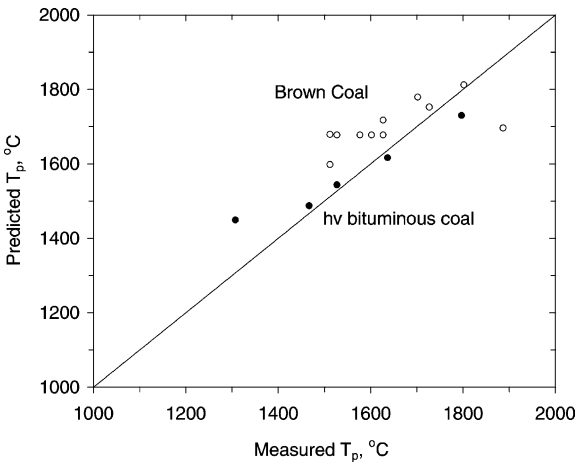


Fig. 36. Parity plot of predicted particle temperatures with a brown coal (○) and hv bituminous coal (●) in an EFR at 0.3 MPa with 12% $O_2$ [73].

the one-point calibration procedure. The maximum error is 19% for the brown coal and 18% for hv bituminous coal.

*3.5.2.4. DMT datasets*. DMT (Deutsche Montan Technologie, GmbH, Germany) presented two separate datasets for Westerholt coal in an EFR [74,75]. One used particle sizes of 100–125 μm and the other used sizes of 315–500 μm. The coal properties reported in the original publication were not complete, so we used the properties for the same coal reported elsewhere [80].

The predictions of coal burnout for the small-particle dataset are compared to the measured values in Fig. 37. The predictions are within experimental uncertainty in all but two cases. Slight overpredictions were seen for 1.5 MPa with 5.0% $O_2$, and for 2.0 MPa with 0.5% $O_2$. The best-fit value of $A_{30}$ is $5.5 \times 10^7$ over the five separate cases in this dataset.

Table 13
Evaluation of predicted particle sizes in the EFR at IVD for 12% $O_2$ at 0.3 MPa

| *t*, ms | $T_G$ and $T_W$, °C | Measured $d_P$, μm | Predicted $d_P$, μm | Error, % |
|---|---|---|---|---|
| *Brown coal* | | | | |
| 250 | 1000 | 160 | 190 | 18.8 |
| 250 | 1100 | 150 | 158.8 | 5.9 |
| 250 | 1200 | 150 | 137.5 | 8.3 |
| 250 | 1350 | 90 | 107.1 | 19.0 |
| *hv Bit.* | | | | |
| 200 | 1000 | 270 | 222 | 17.8 |
| 200 | 1100 | 200 | 209 | 4.5 |
| 200 | 1200 | 200 | 203 | 1.5 |
| 200 | 1350 | 200 | 188 | 6.0 |
| 200 | 1500 | 200 | 175 | 12.5 |

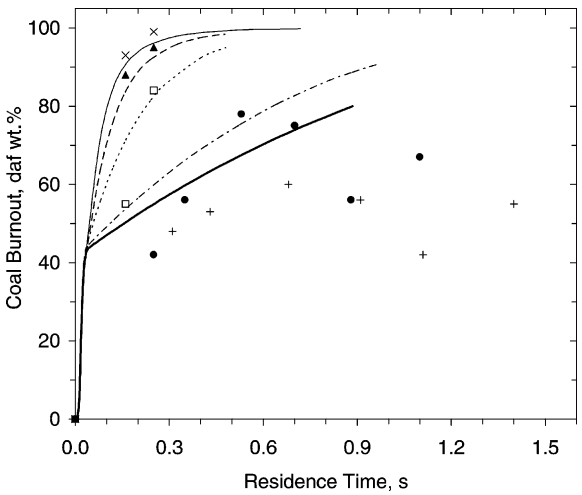


Fig. 37. Burnout of Westerholt coal in an EFR at 1200 °C and (+ and lower solid curve) 0.5% $O_2$ at 2.0 MPa; (● and dot–dash curve) 0.7% $O_2$ at 1.5 MPa; (□ and dotted curve) 2.5% $O_2$ at 1.5 MPa; (▲ and dashed curve) 5.0% $O_2$ at 1.5 MPa; and ( × and upper solid curve) 7.5% $O_2$ at 1.5 MPa [74].

The predicted extents of burnout for particle sizes of 315–500 μm in the second dataset are compared to the measured values in Fig. 38. The experimental data show that the burnout increased by only 6% at 200 ms and by 3% at 650 ms as the total pressure was increased from 0.1 to 1.5 MPa. Such a small effect is an indication that burning rates were limited by film diffusion, because the bulk diffusion rate of $O_2$ is nominally independent of pressure. The predicted burnout shows a much wider variation over the different pressures which, at 200 ms, ranges from 10% at 0.1 MPa to 30% at 1.5 MPa. This variation persists for longer residence times. It is due primarily to the pressure dependence in the new swelling factor correlation in CBK/

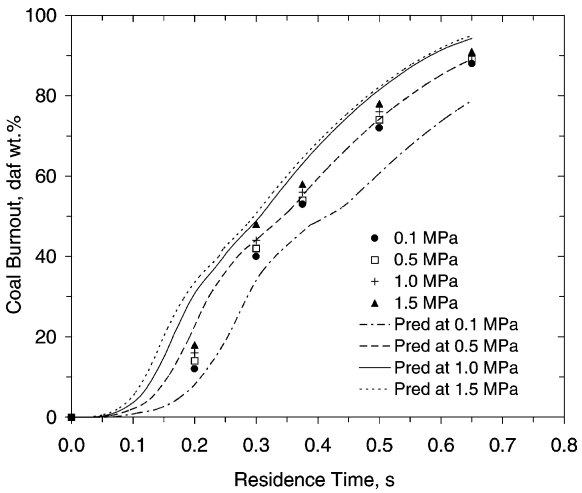


Fig. 38. Burnout of 315–500 μm Westerholt coal in an EFR at 800 °C in air at various pressures [75].

E, which significantly increases the particle size for pressures to 0.8 MPa then reduces the size for even higher pressures. This aspect explains the significant differences among the predicted ignition times which, in turn, are responsible for the apparent pressure dependence in the extents of burnout. Had the ignition points been the same, then the predicted burnout histories would have been essentially independent of pressure. The faster conversion during the later stages that is seen in the data is probably due to the participation of more than the external surface area of the particles, which occurs when the char has large voids and highly irregular perimeters.

Also, the particles in this test series were large enough to sustain substantial gradients within the particles, which were not accounted for in the simulations. The model would therefore tend to overpredict the particle temperatures during the initial stages.

*3.5.2.5. CRC dataset*. A dataset from the Cooperative Research Center (CRC) on Black Coal Utilization at the Univ. of Newcastle in Australia [72] contains two cases from a pressurized drop tube furnace at 1200 °C. The coal burnout level of an Australian bituminous coal was measured at various residence times. Fig. 39 shows the prediction at 0.1 and 1.5 MPa based on the $A_{30}$ of $5.0 \times 10^6$. With the assigned $A_{30}$, the prediction at 0.1 MPa is in reasonable agreement with measurement; however, the burnout at 1.5 MPa was over-predicted. The kinetics assigned from this dataset are much slower than all others, and inconsistent with expectations.

*3.5.2.6. RISO dataset*. Only two cases were reported for an EFR at RISO in Denmark [43] that was operated at 700 °C and pressures of 0.5 and 1.0 MPa with Colombian Cerrejon bituminous coal. The $O_2$ levels were set to 7 and 3.5 mol%

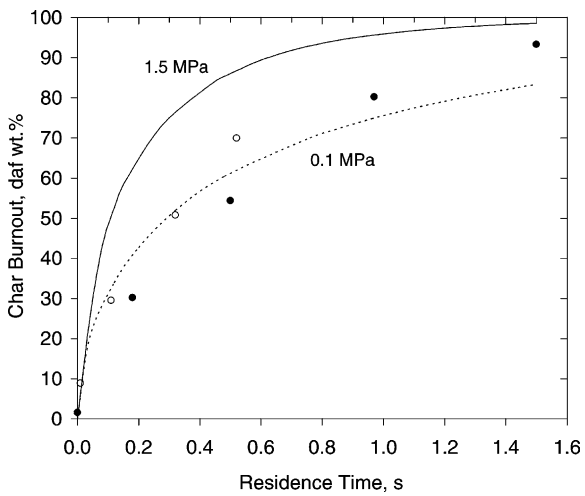


Fig. 39. Coal burnout of Australian Lithgow bituminous coal in a EFR at 1200 °C in air at 0.1 MPa (dotted curve, ●) and at 1.5 MPa (solid curve, ○) [72].

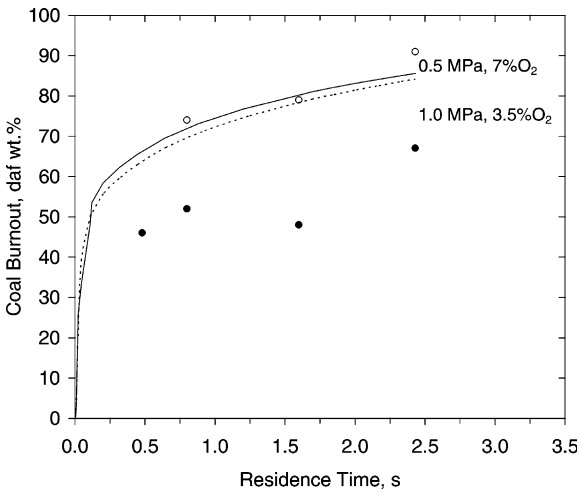


Fig. 40. Burnout of Columbian Cerrejon coal in a EFR at 700 °C at 0.5 MPa with 7% $O_2$ (solid curve, ○) and at 1.5 MPa with 3.5% $O_2$ (dotted curve, ●) [43].

at 0.5 and 1.0 MPa, respectively, to maintain the same $O_2$ partial pressure in these two cases. The coal burnout profiles as functions of residence time appear in Fig. 40. At 0.5 MPa, the reported coal burnout increased from 71 to 91% as residence time was increased from 800 to 2430 ms, whereas at 1.0 MPa, the burnout increased from 46 to 67% as time increased from 480 to 2430 ms. The reported burnout at 1.0 MPa is lower than that at 0.5 MPa by about 25% over the full range of residence time, but the predicted profiles show only a slight reduction in the burning rate for the higher pressure. This tendency was attributed to differences in char physical properties for the two test pressures [43], but without any quantitative evidence. It is difficult to rationalize such large changes in physical structure over the limited range of conditions imposed in this test series. The dataset indicates that higher char yields were obtained from devolatilization as pressure was increased from 0.5 to 1.0 MPa, which is well beyond the normal pressure range that affects devolatilization yields and char characteristics (Section 2).

### *3.5.3. Shock tube evaluations*

This section presents the evaluations of CBK/E with all the available shock tube datasets. As for the EFR evaluations, the predictions are based on the coal's proximate and ultimate analyses and the shock tube operating conditions, including the initial particle temperature, gas temperature, total pressure, $O_2$ level, reaction time and particle size. The wall temperature was set to 25 °C in all cases. The initial particle temperatures were set to 600 °C for all datasets because the reaction time scale began at the time of arrival of a reflected shock; prior to this time, particles were heated by the products of an incident shock. All model parameters were assigned their default values except $A_{30}$, which, as before, was first fit on a case-by-case

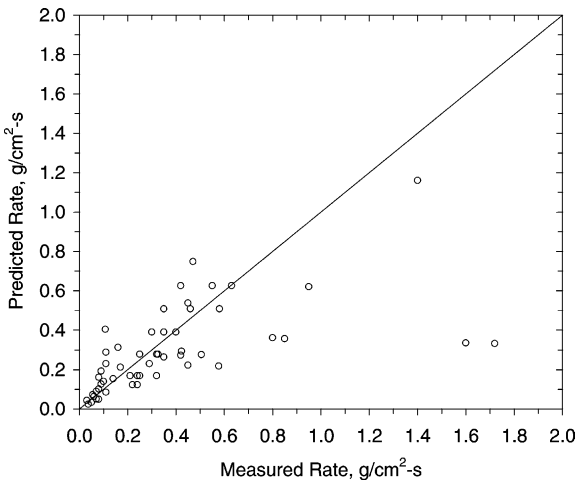


Fig. 41. Parity plot for burning rate predictions for the shock tube database based on the best-fit assignment to $A_{30}$ for each coal.

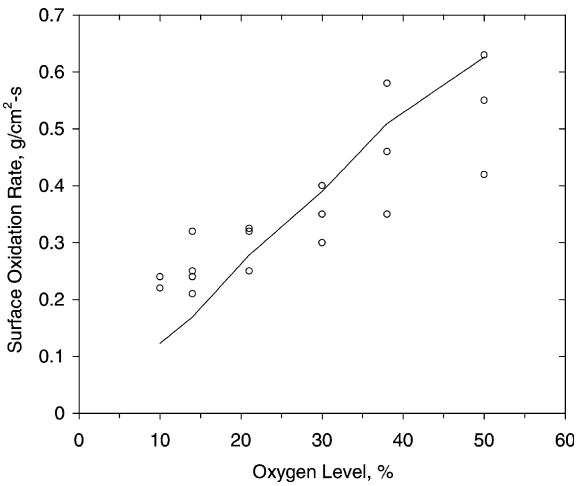


Fig. 42. Evaluation of predicted impact of $O_2$ level on the burning rate of Ill. #6 coal in a shock tube at 0.8 MPa and 1031 °C [79].

basis then assigned an average, best-fit value for each fuel in a dataset. The assignments were based on reported values of the burning rate per unit external surface area.

A parity plot for the burning rates in the entire shock tube database appears in Fig. 41. Burning rates as fast as 0.6 g/cm$^2$ s were assigned without bias within a SSE of 0.32 g/cm$^2$ s. But the few higher rates in this database were seriously underpredicted.

*3.5.3.1. KSU dataset*. Shock tube experiments at Kansas State University (KSU) [79] assigned the burning rates 0.5 ms after particle ignition. The dataset represent gas temperatures from 1031 to 1383 °C, pressures from 0.55 to 1.0 MPa, and $O_2$ mole percentages from 10 to 50%. Only the results for an Ill. #6 coal were reported and used in our evaluation. Fig. 42 shows the impact of $O_2$ mole fraction on the burning rate of Ill. #6 coal at 0.8 MPa and 1031 °C. Multiple points at each $O_2$ level represent repeat measurements under the same operating conditions. Despite the excessive scatter, especially at high $O_2$ levels, the reported burning rates increase for progressively higher $O_2$ levels, as expected. The relationship is near-linear. The predicted relationship in Fig. 42 is also near-linear, although the model underpredicts the rate for $O_2$ levels lower than 20%.

The impact of total pressure on the burning rates of Ill. #6 coal in air from this dataset was presented earlier in Fig. 29. At a gas temperature of 1118 °C, the reported burning rate decreased rapidly from about 1.7 to 0.8 g/cm$^2$ s as total pressure was increased from 0.6 to 0.8 MPa. At 1031 °C, however, the reaction rate only slightly decreased from about 0.55 to 0.40 g/cm$^2$ s as pressure was increased from 0.55 to 0.97 MPa. The authors suggested that lower char surface areas were generated at the higher test pressure which, in turn, reduced the surface reaction rate. But, again, a dramatic change in char structure over the narrow range of pressures investigated is not consistent with what is known about coal fluidity during devolatilization over the domain of test pressures.

The predicted reaction rates at both gas temperatures are within a range of only 0.2–0.4 g/cm$^2$ s at pressures between 0.6 and 0.8 MPa, which is considerably lower than the measured values. The predicted rates are also independent of pressure between 0.6 and 0.8 MPa, because film diffusion is the rate limiting process. The best-fit value for $A_{30}$ was $4.0 \times 10^8$.

*3.5.3.2. Eindhoven datasets*. Three fuels were tested in the shock tube at Eindhoven at the same operating conditions [77,78]. One dataset was recorded with the char from Gottelborn hv bituminous coal, and the second covered Illawara bituminous coal char and Polish hv bituminous coal. Reaction rates were assigned from the variation in the measured particle size during the tests. The extent of burnout for the assigned reaction rate was not specified, so we evaluated the predicted rates at the initial stage for all the cases in the datasets.

Parity plots for this dataset appear in Fig. 43. For Gottelborn hv bituminous char in the upper panel, the predictions are within experimental uncertainty in all but the two cases with the highest burning rates, which are underpredicted. For the Illawara bituminous coal char in the lower panel, the predictions are within the experimental uncertainty over the full range. The discrepancies are larger for the Polish hv bituminous coal, although there is no systematic bias in these predictions either. The above predictions were based on best-fit values of $A_{30}$ of $8.0 \times 10^7$, $2.0 \times 10^7$, and $1.1 \times 10^7$ for the Gottelborn, Illawara, and Polish coal chars, respectively.

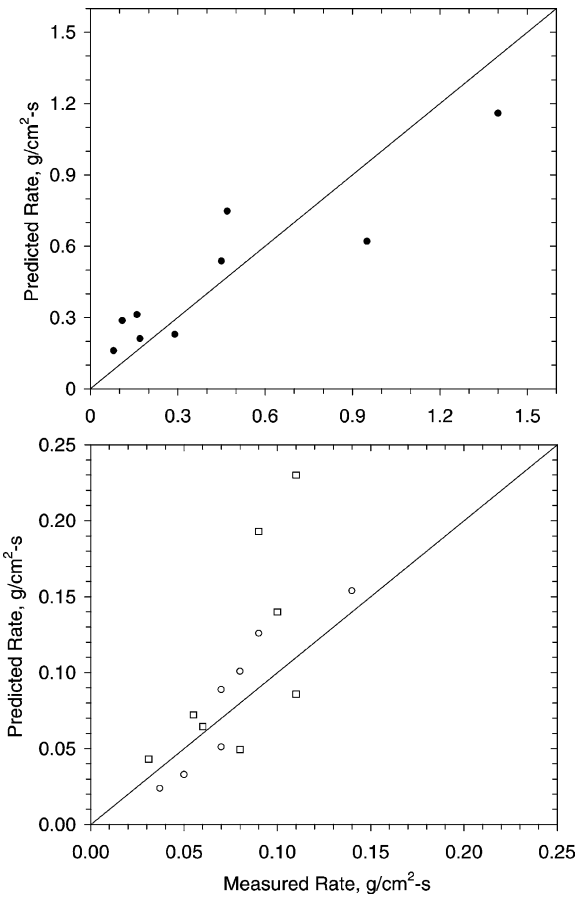


Fig. 43. Burning rates of (Upper, ●) Gottelborn hv bituminous char, (Lower, ○) Illawara bituminous coal char and (Lower, □) Polish hv bituminous coal in a shock tube at 0.9 MPa and 927–1527 °C [77,78].

### 3.6. Discussion

#### 3.6.1. Rank dependence of rate parameter $A_{30}$

The best-fit values for $A_{30}$ of 14 coals presented earlier are collected in Fig. 44. The assignment for the CRC dataset is omitted, because the associated burning regimes were incompatible with the test conditions and the assigned value for $A_{30}$ was, therefore, much lower than the others. The rank dependence of $A_{30}$ for atmospheric pressure is also rendered in the figure for comparison, which was assigned from the char combustion database for atmospheric pressure from Sandia National Laboratories, Livermore [94].

As shown in Fig. 44, the log of $A_{30}$ is inversely proportional to the fuel's carbon content on a daf-basis. For high rank coals with daf carbon contents above 80%, the magnitudes of $A_{30}$ for oxidation at atmospheric pressure is only slightly greater than the values for elevated pressures, so that the differences are within the scatter in the assignments for elevated pressure. However,

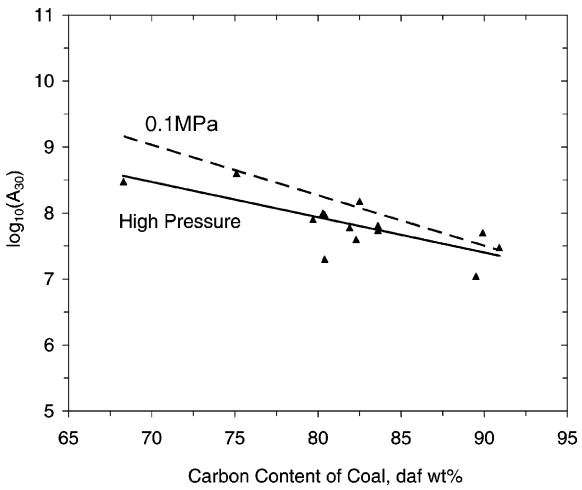


Fig. 44. Rank dependence of the best-fit values for $A_{30}$. Filled triangles denote the best-fit values for each fuel. The solid line represents a correlation between $\log_{10}(A_{30})$ and a fuel's carbon content obtained from this study, and the dashed line represents the analogous correlation for char conversion at atmospheric pressure prepared by Hurt.

the magnitude of $A_{30}$ for low rank coal oxidation at high pressures is lower than for atmospheric pressures. The discrepancy increases to just over one-half an order-of-magnitude as carbon content decreases from 80 to 67%. Most of the cases with low-rank coals were found to be too close to the film diffusion limit for accurate determination of $A_{30}$, so only two $A_{30}$ assignments were made for this portion. One of them is consistent with the correlation for atmospheric pressure while the other is lower. Clearly, special datasets for low-rank coals are needed to resolve this issue in which lower temperatures and/or smaller particle sizes are specifically employed to avoid the diffusion limit. The apparent differences are expressed in the following correlations:

$$\log_{10}(A_{30}) = \begin{cases} 14.38 - 0.0764C_{\text{daf}}, & \text{0.1 MPa only,} \\ 12.22 - 0.0535C_{\text{daf}}, & \text{elevated pressures} \end{cases} \tag{10}$$

where $C_{\text{daf}}$ denotes the carbon content (%) on a daf basis.

Note that these correlations implicitly reflect a host of supplemental variations with coal quality in CBK/E, including estimates for the coal density, the density of combustibles in char, and, perhaps most important, the swelling factor. These implicit connections have two important implications: First, the correlations should not be incorporated into other char oxidation mechanisms unless all the supplemental information is also the same. Second, these correlations will need to be modified whenever the supplemental information is upgraded. For example, the apparent rank dependence in the initial reactivity may be biased by inaccurate swelling factors for

portions of the rank spectrum, and these biases can only be eliminated by improving the accuracy of the swelling factor correlation.

It is also important to realize that both the correlations in Eq. (10) can only depict the overall tendency in the initial reactivity for different coal samples. They do not depict the sample-to-sample variability, as apparent from the substantial scatter about the regression line in the assignments for elevated pressure in Fig. 44. We currently do not know which of the many potential aspects of the composition and morphology of coal and char actually determine the initial char oxidation reactivity. Until the essential nature of this rank dependence has been resolved, models such as CBK/E should be regarded as powerful tools for extrapolating across a wide domain of operating conditions, given sufficient measurements on the burnout of every coal of interest to specify the initial reactivity parameter. In general, a one-point calibration for every sample with either an extent of burnout or loss-on-ignition measurement for the latest stages of combustion is sufficient to predict char oxidation across a wide domain of operating conditions.

#### 3.6.2. Rank dependence of char oxidation at elevated pressures

The rank dependence based on the $A_{30}$ correlation for high rank coals at elevated pressure is slightly weaker than that for char oxidation at atmospheric pressure, indicating that pressure has little impact on the burning rates of high rank coals. Here the burning rate refers to the rate of mass loss per unit external surface area. A recent study on char morphology and char reactivity [95] concluded that pyrolysis pressure has little effect on intrinsic reactivity—the mass loss rate per internal surface area—of bituminous chars, and has a slight impact on the burning rates of the three coals investigated, although the morphology of bituminous chars at different pyrolysis pressures varied significantly due to enhanced plasticity at progressively higher pressures. This conclusion is consistent with the reactivity correlations in this study, and their insensitivity to pressure for high rank chars.

The significant discrepancy in the magnitude of $A_{30}$ for low-rank coals between atmospheric and high pressure oxidation exerts little impact on burnout predictions, because most low-rank coal chars will burn in the film-diffusion-limited regime in p.f. flames. In this regime, the rate is governed by the diffusivity of $O_2$ in the boundary layer and the particle size, and is independent of the values for the rate constants in the chemical kinetics.

From a more theoretical perspective, a lower reactivity for low-rank char oxidation for higher pressures is easily rationalized. As discussed earlier, bituminous coals undergo a plastic stage at both atmospheric and high pressures, and plasticity is enhanced at elevated pressures. Low-rank coals do not become plastic during rapid heating at atmospheric pressures, but they do become plastic at elevated pressures [96]. The high fluidity of coal melts during a plastic stage allows extensive alignment and rearrangements of graphitic carbon lamellar structures in the nascent char. Such alignments are associated with lower reactivity, because chars with highly oriented graphitic crystallites are much less reactive than disordered carbons [47]. Hence, the enhanced fluidity associated with devolatilization at elevated pressures [96] tends to reduce char oxidation rates, and also to diminish the rank dependence of these rates. The fact that such nonreactive char material tends to be formed into cenospheres further diminishes their burning rates, because cenospheres have low internal surface areas.

Another potential explanation pertains to catalysis by Ca impurities in coal, which is primarily responsible for the high reactivity of low-rank coal chars at atmospheric pressure. But the impact of elevated pressure on this catalysis has not yet been characterized.

### 3.7. Pressurized combustion applications

#### 3.7.1. Pressurized applications

CBK/E has been validated against the combustion behavior of a variety of coal types at both atmospheric and elevated pressure. Notwithstanding a few major discrepancies, CBK/E is sufficiently robust to predict various combustion characteristics within useful quantitative tolerances across the entire domain of test conditions, including char burnout, the burning rate, and particle temperature and size.

#### 3.7.2. Coal quality evaluation

Perhaps one of the most important features of CBK/E is the capability to evaluate coal quality impacts. The overall impact is determined by the physical properties of coal and char, the residual char yield after devolatilization, as well as the reactivity of coal whose rank dependence is expressed by the $A_{30}$ correlation in Eq. (10).

The predictions in Fig. 45 show how these factors collectively affect the particle temperature and burnout histories for typical entrained-flow processing conditions. They are based on actual proximate and ultimate analyses for representative subbituminous, hv bituminous, and low volatility coals. The subbituminous and hv bituminous devolatilize at comparably fast rates, but the lv bituminous decomposes much slower. The ultimate yield of volatiles from the lv bituminous is just over half the others. Nevertheless, the maximum particle temperatures are similar because the higher calorific value of volatiles from the lv bituminous compensates for its lower yield. The subbituminous char oxidizes significantly faster than both of the others, which burn at fairly similar rates. Even so, the lv bituminous requires much longer times to burnout than the hv bituminous, due to its much higher char yield after devolatilization.

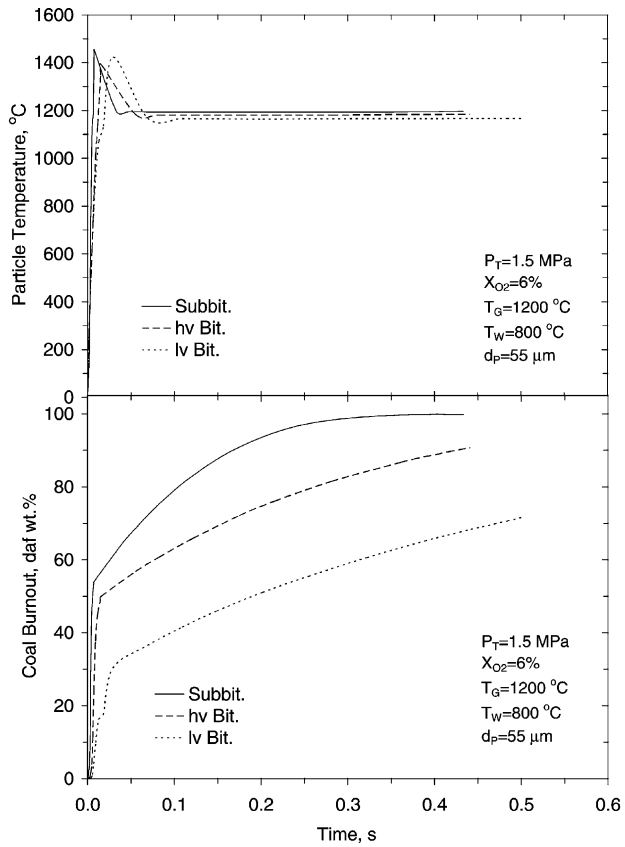


Fig. 45. (Upper) Predicted particle temperature and (Lower) burnout histories of 55 μm subbituminous, hv bituminous, and lv bituminous coals injected into 6% $O_2$ at 1200 °C and 1.5 MPa within a chamber at 800 °C.

*3.7.3. Char oxidation during entrained coal gasification*

The simulations in this section place the validated version of CBK/E in the context of entrained coal gasification with several sensitivity analyses for char combustion at typical gasification conditions. All cases are based on a typical Australian bituminous coal under the operating conditions for a pressurized entrained flow gasifier in Table 14. The gas and wall temperatures were 1300 and 1100 °C, and the particle size was 60 μm. Total pressures of 0.5, 1.0 and 2.0 MPa and $O_2$ levels of 3, 6 and 10% were examined. The value of $A_{30}$ was assigned from the high-pressure correlation obtained in this study, and default values were applied to all other parameters.

The predicted particle temperature and mass as a function of residence time appear in Fig. 46a. At 3% $O_2$ and 2.0 MPa, the particle is heated to 1100 °C within about 13 ms, as seen in the upper panel. The particle heating rate then falls off sharply while the temperature reaches its maximum value of 1400 °C at 30 ms, and slowly decays during the rest of the simulation. With more $O_2$, the particle temperature achieves much higher maximum values in shorter times, as expected. In the lower panel, the char mass decreases rapidly during the first 13 ms due to moisture loss and devolatilization, then the much slower char burning rate determines a longer decay. With 3% $O_2$, the extent of burnout is 99% after 180 ms. Burnout times decrease with higher $O_2$ levels, approaching 50 ms with 10% $O_2$.

The associated variations of particle size and density appear in Fig. 46b. During devolatilization, density falls sharply due to swelling and volatiles release. The char burns in a near-shrinking-core mode thereafter, so sizes shrink continuously while density remains constant until the contributions from the much higher ash density dominate during the latest stages of burnout. This transition begins at roughly 90% burnout.

The impact of total pressure on the particle temperature and burnout histories is minimal, as seen in Fig. 47a. The predicted

Table 14
Entrained coal gasification conditions

| Testing conditions | Values |
|---|---|
| Coal | Australian hv bituminous |
| Pressure, MPa | 0.5, 1.0 and 2.0 |
| $O_2$ level, % | 3, 6, and 10 |
| Gas temperature, °C | 1300 |
| Wall temperature, °C | 1100 |
| Particle size, μm | 60 |

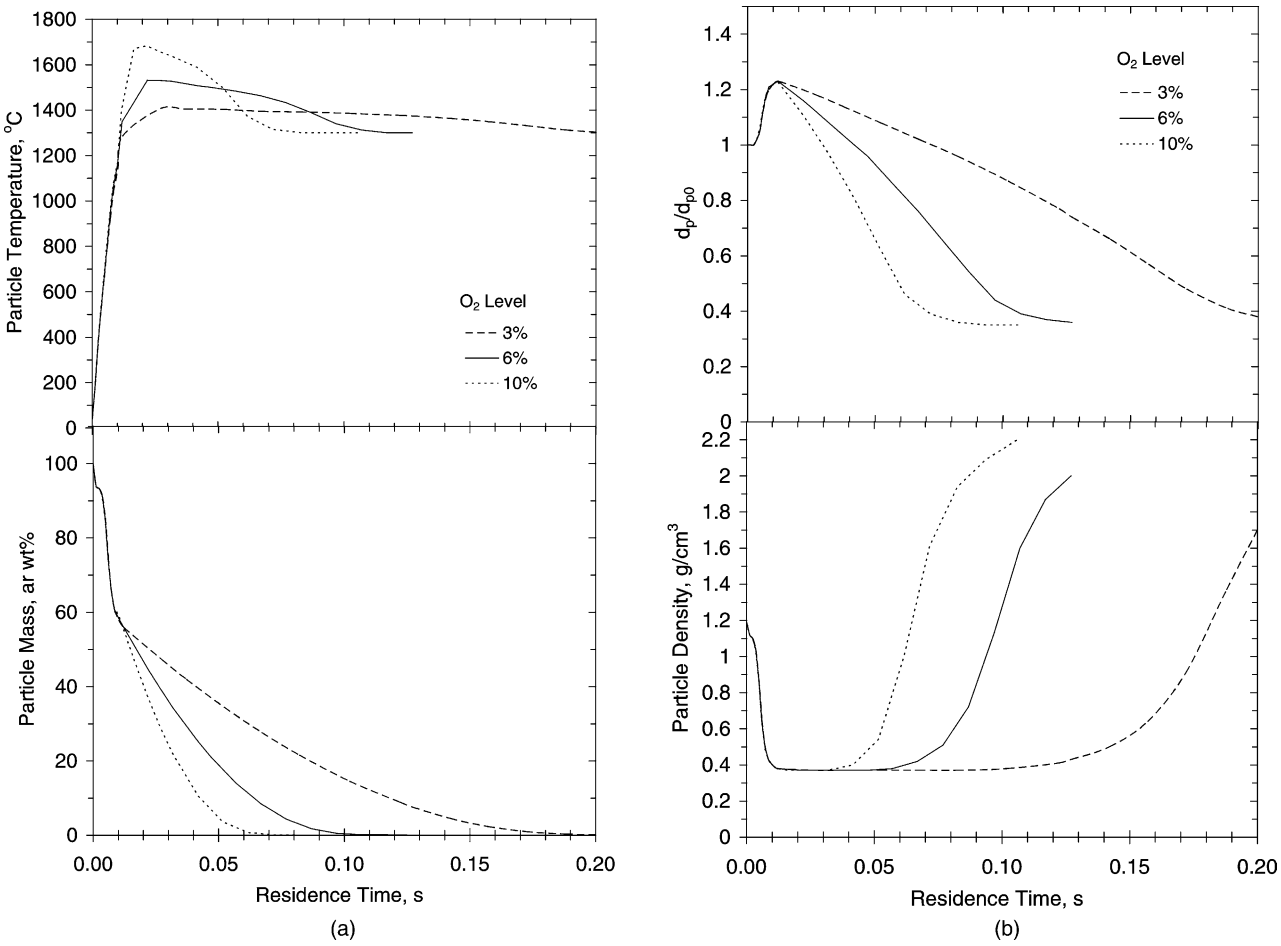


Fig. 46. (a) (Upper) Particle temperature and (Lower) mass, and (b) (Upper) Normalized particle diameter and (Lower) particle density after injection of 60 μm SS003AUS coal into a 1100 °C gasifier with gases at 2.0 MPa and 1300 °C.

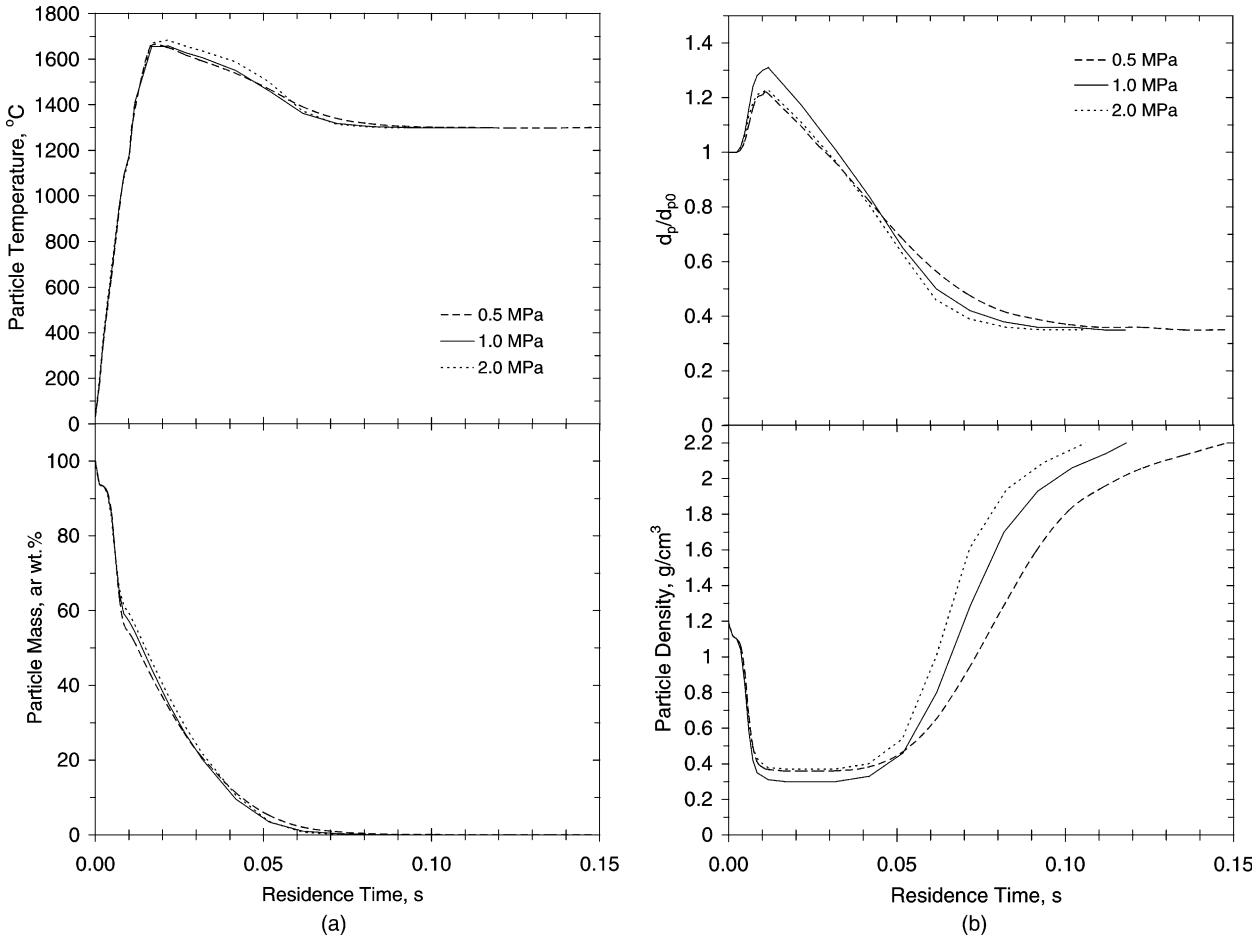


Fig. 47. (a) (Upper) Particle temperature and (Lower) mass, and (b). (Upper) Normalized particle diameter and (Lower) particle density after injection of 60 μm SS003AUS coal into a 1100 °C gasifier with gases at 1300 °C with 10% $O_2$, for total pressures from 0.5 to 2.0 MPa.

particle size and density histories in Fig. 47b show a stronger pressure dependence. The main effect is due to the variation in swelling factors, which reaches 1.3 at 1.0 MPa, compared to 1.22 at both 0.5 and 2.0 MPa. The swelling factor variation is also responsible for the predicted density variations, whereby the most swollen chars have the lowest density.

## 4. Summary and recommendations for future research

### 4.1. Summary

#### 4.1.1. Coal devolatilization

The database reported in English on rapid coal devolatilization at elevated pressures covers the relevant domain of operating conditions for current and advanced technology, including coal quality impacts. Three hundred and thirty-two independent tests with ninety-nine coals characterized heating rates to $10^5$ °C/s, temperatures to 1300 °C, pressures to 16.7 MPa, and the entire coal rank spectrum. Three-fourths of the database was obtained with WMRs. Complementary test results from EFRs are more directly relevant to entrained coal gasification conditions, due to the faster heating rates, and also provided opportunities to validate submodels for the thermal histories of entrained coal particles.

The database exhibits several trends that are essential for rational design of pressurized coal utilization technology, and a few surprising departures from conventional wisdom as well. Weight loss diminishes for progressively higher pressures. With bituminous coals, the reduction in yield is essentially complete once 15–30% of the ultimate weight loss at atmospheric pressure has been eliminated. For pressures above 1 MPa, the ultimate weight loss from hv bituminous coals falls at approximately 2.5 daf wt% per MPa increase in the operating pressure, with little variation among samples of this rank. Somewhat surprisingly, the total yields from low-rank coals diminish over the same range of pressure as bituminous coals, although the quantitative reductions tend to be smaller. Nominal devolatilization rates are insensitive to pressure variations.

Tar yields usually fall by up to 50% at elevated pressures. Gas yields increase at higher pressures, but not by enough to compensate for the reduction in tar yields. The hydrogen enrichment of tars appears to be significantly greater at elevated pressures. High-pressure tars also appear to contain less oxygen, but more data is needed to make this observation definitive. The yields of $CO_2$ and $H_2O$ appear to be insensitive to pressure variations, whereas the yields of all aliphatic hydrocarbons, especially $CH_4$, increase at elevated pressures. The pressure dependence of CO yields is not apparent in the available database, due to an acute sensitivity to the severity of the thermal history.

One of the most surprising findings is that faster heating rates do not enhance ultimate weight loss or tar yields at the highest operating pressures. But coal quality is just as important at 1 MPa as it is at 0.1 MPa. Essentially the same sample-to-sample variability is reported for higher pressures as for atmospheric pressure.

The best available mechanistic explanation for these effects is the flash distillation analogy, which is based on a phase equilibrium among like-sized fragments in the condensed and vapor phases. The phase equilibrium shifts to retain a larger portion of the lighter fragments in the condensed phase as the pressure is increased. These fragments would constitute the heavy end of the tar MWD at low pressures, but remain in the coal at elevated pressures. Consequently, tar prepared at higher pressures becomes lighter and the tar yield diminishes. The fragments retained in the char also contain precursors to noncondensible gases which are eventually released, so gas yields increase as the pressure is elevated, but not by enough to compensate for the retention of tar precursors.

Heating rate affects the rate, yields, and composition of volatiles. As the heating rate is increased, the onset of devolatilization moves to higher temperatures and the devolatilization rate increases in rough proportion to the heating rate. Rapid heating enhances yields at lower pressures by delaying the generation of primary fragments until higher temperatures are achieved, where more of the heavier fragments are expelled as tar. Consequently, tar becomes more abundant and heavier as heating rates are accelerated. And gas yields decrease because the additional tar shuttles away precursors to noncondensibles. But at elevated pressures, the heavier tar fragments cannot vaporize so the heating rate enhancements diminish. Some of the fragment mass is retained in the char, while the rest is released as noncondensible gases during tar cracking.

The FLASHCHAIN® predictions capture the distinctive devolatilization characteristics of individual samples, and represent the sample-to-sample variability with uncanny accuracy, even among samples with the same nominal rank. FLASHCHAIN® also predicts that nominal devolatilization rates are independent of pressure. Whereas the predictions show smaller enhancements due to faster heating rates for progressively higher pressures, the predicted tar yields for very high pressures do not become independent of heating rate, as do the available data. The predictions also do not depict the greater degree of hydrogen enrichment in tars prepared at elevated pressures; in contrast, the predicted tar H/C values diminish slightly for higher operating pressures.

#### 4.1.2. Char oxidation

The database reported in English on char oxidation at elevated pressures covers the relevant domain of operating conditions for current and advanced technology. Two hundred and twenty-one independent tests with 11 coals and 2 coal chars characterized heating rates approaching $10^6$ °C/s, furnace temperatures to 1527 °C, pressures to 2.0 MPa, $O_2$ levels to 100%, and most of the coal rank spectrum. Two-thirds of the database was obtained with

EFRs. Complementary test results from shock tubes characterized much smaller particle sizes, hence, faster heating rates and shorter reaction times.

The database exhibits several trends that are essential for rational design of pressurized coal utilization technology. Burning rates increase for progressively higher $O_2$ partial pressures, but are insensitive to total pressure. They also increase for progressively higher furnace temperatures. Char burning rates tend to become faster for coals of progressively lower rank, but the rank dependence is not directly evident in the database.

CBK/E with the assigned correlation for $A_{30}$ and default values for all other parameters was able to represent the reported combustion behavior in every dataset except one. Model predictions were within useful quantitative tolerances across the entire domain of test conditions. The SSE on the predicted burnout for the EFR database was 11.4% and the SSE on the predicted burning rates for the shock tube database was 0.32 g/cm$^2$ s. However, extents of burnout below 50% in the EFR database tended to be overpredicted, and the highest rates in the shock tube database were underpredicted. The particle temperature predictions were reasonably accurate, except for the underprediction at high burnout levels.

Under typical combustion conditions, the rank dependence of burning rates for high rank coals assigned for elevated pressures is similar to that for char oxidation at atmospheric pressure. The $A_{30}$ values at high pressure are lower by just over one-half order-of-magnitude than those at atmospheric pressure as rank progressively decreases from bituminous coal to lignite. This discrepancy is not important to burnout prediction, because the burning rates of low-rank chars are nearly film-diffusion-limited in p.f. flames.

A one-point calibration with data is needed to assign the initial char oxidation reactivity accurately enough to represent the distinctive char oxidation behavior of individual coal samples.

### 4.2. Recommendations

#### 4.2.1. Coal devolatilization

The imperative for additional laboratory characterizations of pressurized devolatilization must be diverted from ultimate weight loss and tar yields to detailed resolutions of the distributions of all major products, including thorough characterizations of tars and chars. Subbituminous and low volatility coals should be emphasized.

It would also be worthwhile to investigate the potential mechanistic reasons for FLASHCHAIN's inability to depict no heating rate enhancements in the tar yields for very high pressures. Even though the pressures where the flaw becomes evident are much higher than those of practical interest, a resolution of this defect may conceivably improve the accuracy of the predictions over the entire pressure range. For the same reasons, mechanisms should also be developed to predict greater extents of hydrogen enrichment in the tars prepared at elevated pressures.

#### 4.2.2. Char oxidation

The following additional laboratory testing is needed to enhance the predictive capabilities of the current theoretical framework for char oxidation at elevated pressures.

The relationship between coal fluidity during devolatilization and the reactivity of the resulting char needs to be characterized in depth with the same techniques developed to understand the chemical nature of unburned carbon emissions.

Accurate swelling factors are essential for accurate predictions of a fuel's combustion characteristics. Char sizes and bulk particle densities need to be monitored under rapid heating conditions for wide ranges of pressure and coal rank.

Further laboratory studies involving large and diverse sample sets ($>20$ coals) burned under standard conditions in 1D laboratory flow devices are needed to develop improved correlations between coal properties and initial char reactivity. If successful, this could remove the need for the current 1-point calibration procedure. Specific measures should be taken to prevent low-rank chars from burning under the diffusion limit. The combustion measurements should be supported by detailed characterizations of the composition and morphology of char, to identify the factors that actually determine a char's initial oxidation reactivity.

In addition, the following three theoretical developments will significantly improve our predictive capabilities for char oxidation at elevated pressures.

During the 1980s, a skeletal modeling framework was developed to relate coal fluidity during devolatilization to the reaction intermediates in the pyrolysis rate mechanism, particularly metaplast species. This framework provides the best means to relate the coal properties and combustion conditions to swelling behavior and to the initial intrinsic reactivity for char oxidation.

Homogeneous chemistry within the boundary layer of a reacting char particle should be analyzed in detail for combustion at elevated pressures. An initial analysis with detailed gas chemistry is needed to determine energy feedback rates due to CO oxidation in boundary layers, and to identify the concentrations of the various oxidizers ($O_2$, OH, O-atoms) that reach the char particle surface. The detailed analysis will ultimately be used to develop simpler, quasi-global schemes for deployment in engineering submodels like CBK/E.

Like FLASHCHAIN®, CBK/E should be used to specify the parameters in the simpler quasi-global mechanisms deployed in CFD simulations for char oxidation that mimic the predictions from the complete model.

## Acknowledgements

This research was sponsored by the Center for Coal Utilization in Japan (CCUJ) under the BRAIN-C program, and administered by Mssrs N. Asahiro and T. Ando and Dr M. Harada.

## References

[1] Beer JM. Combustion technology developments in power generation in response to environmental challenges. Prog Energy Combust Sci 2000;26(4–6):301–27.
[2] Cho SM, Ma J, Seltzer AH. Vision 21 Plant Concept Specification Report. Foster Wheeler Development Corp. Report No. 9-441004-01; 2002.
[3] Lin SY, Hirato M, Horio M. The characteristics of coal char gasification around ash melting temperatures. Energy Fuels 1994;8:598–606.
[4] Wall TF, Liu G-S, Wu H-W, Roberts DG, Benell KE, Gupta S, Lucas JA, Harris DJ. The effect of pressure on coal reactions during pulverized coal combustion and gasification. Prog Energy Combust Sci 2002;28:405–33.
[5] Niksa S. Predicting the devolatilization behavior of any coal from its ultimate analysis. Combust Flame 1995;100:384–94.
[6] Genetti D, Fletcher TH. Predicting $^{13}C$ NMR measurements of chemical structure of coal based on elemental composition and volatile matter content. ACS Div Fuel Chem Pre 1997;41(1): 194–8.
[7] Zhao Y, Serio MA, Bassilakis R, Solomon PR. A method of predicting coal devolatilization behavior based on the elemental composition. Proc Combust Inst 1994;25:553–60.
[8] Messenbock RC, Dugwell DR, Kandiyoti R. $CO_2$ and steam-gasification in a high-pressure wire-mesh reactor: the reactivity of Daw Mill coal and combustion reactivity of its chars. Fuel 1999;78:781–93.
[9] Messenbock RC, Dugwell DR, Kandiyoti R. Coal gasification in $CO_2$ and steam: development of a steam injection facility for high-pressure wire-mesh reactors. Energy Fuels 1999; 13(1):122–9.
[10] Megaritis A, Messenbock RC, Chatzakis IN, Dugwell DR, Kandiyoti R. High-pressure pyrolysis and $CO_2$ gasification of coal maceral concentrates: conversions and char combustion reactivities. Fuel 1999;78:871–82.
[11] Megaritis A, Messenbock RC, Collot A-G, Zhuo Y, Dugwell DR, Kandiyoti R. Internal consistency of coal gasification reactivities determined in bench-scale reactors: effect of pyrolysis conditions on char reactivities under high pressure. Fuel 1998;77(13):1411–20.
[12] Megaritis A, Zhuo Y-Q, Messenbock R, Dugwell DR, Kandiyoti R. A new bench-scale high-pressure fluidized bed pyrolysis and gasification reactor design. Ninth International Conference on Coal Science, DGMK Tagungsberichte 9703; 1997. p. 613–6.
[13] Lim J-Y, Chatzakis IN, Megarities AM, Cai H-Y, Dugwell DR, Kandiyoti R. Gasification and char combustion reactivities of Daw Mill coal in wire-mesh and 'hot-rod' reactors. Fuel 1997;76:1327.
[14] Guell AJ, Kandiyoti R. Development of a gas-sweep facility for the direct capture of pyrolysis tars in a variable heating rate high-pressure wire-mesh reactor. Energy Fuels 1993;7: 943–52.
[15] Cai H-Y, Guell AJ, Dugwell DR, Kandiyoti R. Heteroatom distribution in pyrolysis products as a function of heating rate and pressure. Fuel 1993;72(3):321–7.
[16] Cai H-Y. Fast pyrolysis of coals and char characterization in relation to pulverized coal combustion. PhD Imperial College of Science, Technology and Medicine, University London, London, UK; 1995.
[17] Cai H-Y, Guell AJ, Chatzakis IN, Lim J-Y, Dugwell DR, Kandiyoti R. Combustion reactivity and morphological change in coal chars: effect of pyrolysis temperature, heating rate and pressure. Fuel 1996;75(1):15–24.
[18] Gibbins J, Kandiyoti R. Experimental study of coal pyrolysis and hydropyrolysis at elevated pressures using a variable heating rate wire-mesh apparatus. Energy Fuels 1989;3(6):670.
[19] Gibbins J, Kandiyoti R. The effect of variations in time-temperature history on product distribution from coal pyrolysis. Fuel 1989;68:895.
[20] Gibbins-Maltham J, Kandiyoti R. Coal pyrolysis yields from fast and slow heating in a wire-mesh apparatus with a gas sweep. Energy Fuels 1988;2:505.
[21] Tomeczek J, Gil S. Pore structure evolution and volatiles release during high pressure coal pyrolysis. Ninth International Conference on Coal Science, DGMK Tagungsberichte 9703; 1997. p. 545–8.
[22] Wanzl W. Chemical reactions in thermal decomposition of coal. Fuel Process Technol 1988;20:317–36.
[23] Arendt P, van Heek K-H. Comparative investigations of coal pyrolysis under inert gas and $H_2$ at low and high heating rates and pressures up to 10 MPa. Fuel 1981;60(9):779–87.
[24] Eklund H, Wanzl W. Pyrolysis and hydropyrolysis of solid fuels at high heating rates using Curie point technique. Int Conf Coal Sci, IEA 1981;701–7.
[25] Kaiser M, Wanzl W, vanHeek KH, Juntgen H. Kinetics of primary and secondary reactions during coal pyrolysis at high heating rates using Curie-point technique. Int Conf Coal Sci, IEA 1985;899–902.
[26] Ko GH, Sanchez DM, Peters WA, Howard JB. Correlations for effects of coal type and pressure on tar yields from rapid devolatilization. Proc Combust Inst 1988;22:115–24.
[27] Ko GH. Pyrolysis of different coal types. PhD. Cambridge, MA: MIT; 1988.
[28] Suuberg EM. In: Schlosberg RH, editor. Chemistry of coal conversion. New York: Plenum Press; 1985. [chapter 4].
[29] Griffin TP, Howard JB, Peters WA. An experimental and modeling study of heating rate and particle size effects in bituminous coal pyrolysis. Energy Fuels 1993;7(2):297–305.
[30] Bautista JR, Russel WB, Saville DA. Time-resolved pyrolysis product distributions of softening coals. Ind Engr Chem Fundam 1986;25:536.
[31] Heyd LE. Weight loss behavior of coal during rapid pyrolysis and hydropyrolysis. MS. Princeton, NJ: Princeton University Press; 1982.
[32] Niksa S, Russel WB, Saville DA. Time-resolved weight loss kinetics for the rapid devolatilization of a bituminous coal. Proc Combust Inst 1982;19:1151.
[33] Mill CJ, Harris DJ, Stubington JF. Pyrolysis of fine coal particles at high heating rates and high pressure. Eighth

Australian Coal Science Conference, Australian Institute of Energy; 1998. p. 151–6.
[34] Sathe C, Li C-Z. Effects of heating rate and pressure on the pyrolysis yields of a brown coal. Tenth International Conference on Coal Science, Shanxi Sci: Technol. Press; 1999. p. 709–12.
[35] Sathe C, Pang B, Li CZ. Effects of pyrolysis conditions on the thermal decomposition of a Victorian low-rank coal. Thermal Energy Engineering and the Environment, University of Adelaide; 1998. p. 373–84.
[36] Duxbury J. Prediction of coal pyrolysis yields from BS volatile matter and petrographic analyses. Fuel 1997;76(13):1337–43.
[37] Cor J, Manton N, Mul G, Eckstrom D, Olson W, Malhotra R, Niksa S. An experimental facility for the study of coal pyrolysis at 10 atmospheres. Energy Fuels 2000;14(3): 692–700.
[38] Tomita A. Analysis of product distribution in coal pyrolysis under high pressure. No. 97TM5021, Sendai, Japan: Institute for Chemical Reaction Science, Tohoku University; 1997.
[39] Mathews JF, Yeasmin J, Ouyang S. Devolatilization of Yallourn brown coal at elevated pressure in an entrained flow reactor. Ninth International Conference on Coal Science, DGMK Tagungsberichte 9703; 1997. p. 629–32.
[40] Yeasmin H, Matthews JF, Ouyang S. Rapid devolatilization of Yallourn brown coal at high pressures and temperatures. Fuel 1999;78:11–24.
[41] Yeasmin J, Ouyang S, Mathews JF. Characteristics of chars produced from devolatilization of Yallourn brown coal at elevated pressure. Ninth International Conference on Coal Science, DGMK Tagungsberichte 9703; 1997. p. 689–92.
[42] Hamalainen JP, Aho MJ. Conversion of fuel nitrogen through HCN and $NH_3$ to nitrogen oxides at elevated pressure. Fuel 1996;75(12):1377–86.
[43] Gjernes E, Fjellerup J, Hansen LK, Hald P, Kirkegaard M, Illerup JB, Rathmann O, Olsen A. Combustion and gasification of coal and straw under pressurized conditions. Task 4. Determination of kinetic parameters (coal) in PEFR. Riso-R-812(EN) and NTIS DE96711738, Roskilde, Denmark: Riso National Laboratory; 1995.
[44] Takeuchi M, Berkowitz N. Fast pyrolysis of some western Canadian subbituminous coals. Fuel 1989;68(10):1311–9.
[45] Lee C-W. Effect of pressure on rapid pyrolysis and resultant char structure of a caking coal. PhD Pennsylvania State University, State College, PA; 1989.
[46] Lee CW, Jenkins RG, Schobert HH. Mechanisms and kinetics of rapid, elevated pressure pyrolysis of Illinois No. 6 bituminous coal. Energy Fuels 1991;5:547–55.
[47] Lee CW, Jenkins RG, Schobert HH. Structure and reactivity of char from elevated pressure pyrolysis of Illinois No. 6 bituminous coal. Energy Fuels 1992;6(1):40–7.
[48] Bissett LA. Response surface model predictions for the flash pyrolysis of Montana Rosebud coal. ACS Div Fuel Chem Prepr, ACS 1983;222–9.
[49] Bissett, L.A., High-temperature, high-pressure flash pyrolysis of Montana Rosebud coal. NTIS DE86006618, METC, Morgantown, WV; 1986.
[50] Bissett LA. Flash pyrolysis of Montana Rosebud coal. 1. Experimental data and response surface model predictions for product gas and char. Energy Fuels 1988;2:819–27.
[51] Neoh KG, Gannon RE. Coal volatile yield and element partition in rapid pyrolysis. Fuel 1984;63(10):1347–52.
[52] van Krevelen DW. Coal. Coal science and technology, 3, Amsterdam: Elsevier; 1981.
[53] Oh MS, Peters WA, Howard JB. Fuel 1989;65:251.
[54] Unger PE, Suuberg EM. Molecular weight distributions of tars produced by flash pyrolysis of coals. Fuel 1984;63:606.
[55] Suuberg EM, Unger PE, Lily WD. Experimental study on mass transfer from pyrolysing coal particles. Fuel 1985;64:966.
[56] Solomon PR, Serio MA, Deshpande GV, Droo E. Cross-linking reactions during coal conversion. Energy Fuels 1990; 4:42.
[57] Howard JB. In: Elliot MA,, editors, 2nd suppl. Chemistry of coal utilization, vol. 1981. New York: Wiley–Interscience; 1981. [chapter 12].
[58] Niksa S. Rapid coal devolatilization as an equilibrium flash distillation. AIChE J 1988;34(5):790–802.
[59] Niksa S. FLASHCHAIN theory for rapid coal devolatilization kinetics. 4. Predicting ultimate yields from ultimate analyses alone. Energy Fuels 1994;8:659.
[60] Niksa S. Predicting the complete distributions of volatile products from diverse fuel types with FLASHCHAIN. Proceedings of the Fifth International Conference on Technology and Combustion for a Clean Environment, vol. 1. Lisbon: C. Gulbenkian Foundation; 1999. p. 709–15.
[61] Freihaut JD, Proscia WM. Tar evolution in heated-grid apparatus. Energy Fuels 1989;3:625.
[62] Tomita A. Personal communication; 1997.
[63] Lau C-W, Niksa S. The impact of soot on the combustion characteristics of particles of different coal types. Combust Flame 1993;95:1–21.
[64] Niksa S, Cho S. Assigning meaningful stoichiometric ratios for pulverized coal flames. Proc Combust Inst 1998;27: 2905–13.
[65] Shim H, Hurt RH. Thermal annealing of chars from diverse organic precursors under combustion-like conditions. Energy Fuels 2000;14:340–8.
[66] Hurt RH, Davis KA. Near-extinction and final burnout in coal combustion. Proc Combust Inst 1994;25:561–8.
[67] Essenhigh RH, Fortsch D, Klimesh HE. Combustion characteristics of carbon: influence of the Zone I–Zone II transition on burnout in pulverized coal flames. Energy Fuels 1999; 13(5):955–60.
[68] Hurt RH, Calo JM. Semi-global intrinsic kinetics for char combustion modeling. Combust Flame 2001;125:1138–49.
[69] Aarna I, Suuberg EM. Changes in reactive surface area and porosity during char oxidation. Proc Combust Inst 1998;27: 2933–9.
[70] Sun J-K, Hurt RH. Mechanisms of extinction and near-extinction in pulverized solid fuel combustion. Proc Combust Inst 1996;28:2205–13.
[71] Joutsenoja T, Saastamoinen J, Aho M, Hernberg R. Effects of pressure and oxygen concentration on the combustion of different coals. Energy Fuels 1999;13(1):130–45.
[72] Wall T, Wu H, Benfell K, Liu G, Bryant G. The influence of pressure in pf combustion and gasification: char structure, reactivity, and ash character. Fifth International Conference on Technologies and Combustion Technologies for a Clean Environment, Calouste Gulbenkian Foundation; 1999. p. 733–9.
[73] Reichelt T, Joutsenoja T, Spliethoff H, Hein KRG, Hernberg R. Characterization of burning char particles under pressurized

conditions by simultaneous in situ measurement of surface temperature and size. Proc Combust Inst 1998;27:2925–32.
[74] Scherello A, Hackert G, Wirtz S, Bonn B, Seewald H. Drop tube investigations into coal particle combustion at elevated temperatures and pressures. Ninth International Conference on Coal Science, DGMK Tagungsberichte 9703; 1997. p. 999–1002.
[75] Muhlen H-J, Schulte A. Combustion kinetics of coal particles under pressures up to 20 bar and temperatures up to 900 °C. Int Conf Coal Sci, IEA 1989;269–72.
[76] Monson CR, Germane GJ, Blackham AU, Smoot LD. Char oxidation at elevated pressures. Combust Flame 1995;100: 669–83.
[77] Banin V, Moors R, Veefkind B. Kinetic study of high-pressure pulverized coal char combustion: experiments and modeling. Fuel 1997;76(10):945–9.
[78] Banin V, Commissaris FAC, Moors R, Veefkind B. Kinetic study of pulverized coal combustion at high pressure using a shock tube. Combust Flame 1997;108(1/2):1–8.
[79] Lester TW, Seeker WR, Merklin JF. The influence of oxygen and total pressure on the surface oxidation rate of bituminous coal. Proc Combust Inst 1981;18:1257–65.
[80] Richard J-R, Majthoub MA, Aho MJ, Pirkonen PM. Separate effects of pressure and some other variables on char combustion under fixed bed conditions. Fuel 1994;73(4): 485–91.
[81] Hurt RH, Lunden MM, Brehob EG, Maloney DJ. Statistical kinetics for pulverized coal combustion. Proc Combust Inst 1996;26:3169.
[82] Hurt RH, Sun J-K, Lunden M. A kinetic model of carbon burnout in pulverized coal combustion. Combust Flame 1998; 113:181.
[83] Sun J-K, Hurt RH. A numerical study of the origin of unburned carbon. Ninth International Conference on Coal Science, Essen, Germany, DGMK Tagungsberichte 9703; 1997. p. 927–30.
[84] Hong J-H. Modeling char oxidation as a function of pressure using an intrinsic Langmuir rate equation. PhD Dissertation, Department of Chemical Engineering, Brigham Young University, Utah; 2000.
[85] Benfell KE. Assessment of char morphology in high pressure pyrolysis and combustion. PhD Thesis, Department of Geology, The University of Newcastle, NSW, Australia; 2001.
[86] Hecker WC, Madsen PM, Sherman MR, Allen JW, Sawaya RJ, Fletcher TH. High-pressure intrinsic oxidation kinetics of two coal chars. Energy Fuels 2003;17:427.
[87] Grow D. Mass and heat transfer to an ellipsoidal particle. Combust Flame 1990;80:209–13.
[88] Choi MK, Gavalas GR. A theoretical study of combustion of nonspherical particles. Combust Flame 1993;89:9–26.
[89] Gera D, Mathur M, Freeman M, O'Dowd W. Moisture and char reactivity modeling in pulverized coal combustors. Combust Sci Technol 2001;172:35–69.
[90] Mitchell RE, Akanetuk EJ. The impact of fragmentation on char conversion during pulverised coal combustion. Proc Combust Inst 1996;26:3137–44.
[91] Bayless DJ, Schroeder AR, Peters JE, Buckius RO. Effect of surface voids on burning rate measurements of pulverized coal in diffusion-limited conditions. Combust Flame 1997;108: 187–98.
[92] Stanmore BR, Visona SP. The contribution of char burnout from gasification by $H_2O$ and $CO_2$ during pulverized-coal flame combustion. Combust Flame 1998;113:274–6.
[93] Hong J, Hecker WC, Fletcher TH. Modeling high pressure char oxidation using Langmuir kinetics with an effectiveness factor. Proc Combust Inst 2000;28:2215–23.
[94] Mitchell RE, Hurt RH, Baxter LL, Hardesty DR. Compilation of Sandia coal char combustion data and kinetic analyses: Milestone Report. NTIS Report No. DE92018668; 1992.
[95] Benfell KE, Liu G-S, Roberts D, Harris D, Lucas J, Bailey J, Wall TF. Modeling char combustion: the influence of parent coal petrography and pyrolysis pressure on the structure and intrinsic reactivity of its char. Proc Combust Inst 2001;28: 2233–42.
[96] Lee CW, Scaroni AW, Jenkins RG. Effect of pressure on the devolatilization and swelling behaviour of a softening coal during rapid heating. Fuel 1991;70:957.